Modeling and distributed control of decentralized energy generation: a MIMO approach

Von der Fakultät für Elektrotechnik, Informationstechnik, Physik
der Technischen Universität Carolo-Wilhelmina zu Braunschweig

zur Erlangung des Grades eines Doktors
der Ingenieurwissenschaften (Dr.-Ing.)

genehmigte Dissertation

von Mauro Calabria

aus Olavarría, Argentinien

eingereicht am: 15. April 2015

mündliche Prüfung am: 16. Oktober 2015

1. Referent: Prof. Dr.-Ing. Walter Schumacher
2. Referent: Prof. Dr.-Ing. Bernd Engel

Druckjahr: 2015

PREFACE

This thesis has been written on the basis of the research I conducted at the Institute of Control Engineering, TU Braunschweig from 2012 to 2015 and as participant of the Lower Saxony research network *SmartNord*. The thesis offers a systematic approach to the topic of small signal stability in low-voltage grids with distributed generation and puts emphasis on control engineering aspects.

Although it is impossible to name everybody in these few lines, I would like to acknowledge everyone for their contributions which made this thesis reality.

I am indebted to Prof. Dr.-Ing. Walter Schumacher, who gave me the chance to join his research team and shared his extensive engineering know-how, providing countless hours of tutorship and fruitful discussions.

I must also thank everyone at the Institute for their friendly treat and the enriching work environment. Special thanks go to Jan Klöck, Steffen Lampke, and Onno Martens, who graciously spent a lot of their time reviewing my work.

Thanks to everyone in *SmartNord* for the helpful interdisciplinary knowledge exchange. In particular, I thank Prof. Dr.-Ing. Michael Kurrat and Prof. Dr.-Ing. Bernd Engel for their interest in my work and their participation in the evaluation board.

I would also like to thank Prof. Josep Guerrero and his team at Aalborg University who made the experimental testing possible.

Finally, I would like to use this opportunity to express my enormous gratitude to my girlfriend and my family who have permanently showed me their love and support.

Mauro Calabria
October 2015

CONTENTS

LIST OF OPERATORS, SYMBOLS, AND ABBREVIATIONS

SPECIAL MATHEMATICAL OPERATORS

$\tilde{x}$	Complex variable
$\tilde{x}^*$	Complex conjugate
$\dot{x}, \ddot{x}$	First and second time derivatives
Δx	Linearized variable
$\odot$	Element-wise or Hadamard product
$\boldsymbol{X}^{-T}$	Transposed inverse of the matrix
$\boldsymbol{x}^d$	Diagonal matrix from the vector $\boldsymbol{x}$
$diag(\boldsymbol{X})$	Main diagonal of the matrix
$det(\boldsymbol{X})$	Determinant of the matrix

MOST USED SYMBOLS

$\mathbf{0}$	Zero vector/matrix
$\mathbf{1}$	Identity matrix
$\boldsymbol{A}, \boldsymbol{B}, \boldsymbol{C}, \boldsymbol{D}$	State-space matrices
C	Capacitance
$\tilde{E}$	Equivalent voltage phasor
$f, \boldsymbol{f}$	Frequency, vector of frequencies
$G(s),\ \boldsymbol{G(s)}$	Transfer function, matrix of transfer functions
$\tilde{I}, \tilde{\boldsymbol{I}}$	Current phasor, vector of current phasors
j	Imaginary unit
$k_P,\ k_Q$	Active and reactive power droop
$\boldsymbol{K_P},\ \boldsymbol{K_Q}$	(Diagonal) matrices of active and reactive power droops
k_{Pd}	Dynamic droop gain
$\boldsymbol{k_{Pd}}$	Vector of dynamic droop gains
$\boldsymbol{K_{Pd}}$	(Diagonal) matrix of dynamic droop gains
L	Inductance
$\boldsymbol{N}$	Linearized coupling
$P,\ Q$	Active (true) and reactive power
$\hat{P},\ \hat{Q}$	Estimated active and reactive power
R	Resistance
S	Apparent power

T_P, T_Q	Filter time constants
$\tilde{U}, \tilde{\boldsymbol{U}}$	Voltage phasor, vector of voltage phasors
$\tilde{\boldsymbol{Y}}$	Amittance matrix
$\tilde{Z}, \tilde{\boldsymbol{Z}}$	Impedance, impedance matrix
λ_i	i-th eignevalue
$\theta, \boldsymbol{\theta}$	Phase, vector of phases
ω, ω_{nom}	Angular frequency, nominal angular frequency
ω_{fP}, ω_{fQ}	Filter cutoff frequencies

ABBREVIATIONS

AC	Alternating current
DER	Distributed energy resources
DG	Distributed generation
DPM	Dynamic phasor model
EMS	Energy management system
IGBT	Insulated gate bipolar transistor
LV, MV, HV	Low-voltage, medium-voltage, high-voltage
MG	Microgrid
PCC	Point of common coupling
PWM	Pulse width modulation
RES	Renewable energy sources
TSO	Transmission system operator
VPP	Virtual power plant
VSI	Voltage source inverter

ABSTRACT

The ongoing increase of inverter-interfaced distributed energy generation based on renewable energy sources is notably changing the structure of modern power systems. Particularly in low-voltage grids, the large-scale implementation of droop-controlled distributed generation gives rise to stability issues, given the dynamic response of the power inverters and the complex coupling that arises from the inductive and resistive behavior of the power lines.

This work focuses on the analysis of the small-signal stability of a low-voltage grid with distributed generation and on the design of a proper control law that assures stability independently from the chosen power droops. After a detailed introduction on the fundamentals of the operation of a low-voltage grid with distributed generation, appropriate models are introduced for the power inverters and the grid to which they are connected, followed by a discussion on their dynamics and the limits to which these models are subject.

The implementation of a so-called improved droop controller on a single inverter is proposed and studied in depth, which modifies the dynamics with which a power inverter operates. The damping and stabilizing capabilities of the improved droop controller are studied at full length with the help of graphical control tools such as root-locus, Bode, and Nyquist plots. From this analysis, three systematical design methods are derived, which allow for the tuning of the improved droop controller in a way that enough damping can be guaranteed.

Subsequently, the analysis is extended to a grid with several inverters. Although the tuning of a group of inverters is traditionally done disregarding their coupling, this work considers a low voltage grid as a whole, explicitly contemplating the interaction between power inverters. Accordingly, two methods to tune the improved droop controller for a given group of inverters are derived.

Finally, a reduced-order model of the grid is derived, which captures the most significant aspects of the dynamic behavior of a low-voltage grid with distributed generation.

Laboratory small-scale experiments are included to show the performance and the limits of the proposed approach.

KURZFASSUNG

Die Struktur moderner Energiesysteme hat sich durch das laufende Wachstum der umrichterbasierten dezentralen Energieerzeugung auf Basis erneuerbarer Energiequellen enorm geändert. Besonders in Niederspannungsnetzen führt der großflächige Einsatz von verteilten Erzeugungsanlagen führt zu Stabilitätsproblemen, denn die Dynamik der Wechselrichter und die durch das ohmsche und induktive Verhalten der Stromleitungen komplexe Verkopplung können zu ungedämpften Schwingungen führen.

Diese Arbeit setzt den Schwerpunkt auf die Analyse der Kleinsignalstabilität eines Niederspannungsnetzes mit dezentraler Erzeugung und auf die Auslegung eines geeigneten Regelgesetzes, das Stabilität gewährleisten kann. Nach einer detaillierten Einführung in die Arbeitsweise eines Niederspannungsnetzes mit dezentraler Erzeugung werden geeignete Umrichter- und Netzmodelle eingeführt. Darauf folgt eine Diskussion des dynamischen Verhaltens dieser Modelle und deren Grenzen.

Als Regler wird ein so genannter *improved-droop* Regler vorgeschlagen, der als PDT-Regler auf die Wirkleistungsstatikkennlinie des Umrichters wirkt. Das Dämpfungs- und Stabilisierungsvermögen des PDT-Reglers werden in vollem Umfang mit Hilfe von Wurzelortskurven, Bode- und Nyquist-Diagramme untersucht. Diese Analyse mündet in drei Designmethoden, die die systematische Auslegung des Reglers ermöglichen.

Anschließend wird die Analyse auf ein Niederspannungsnetz mit mehreren dezentralen Umrichtern erweitert. Im Gegensatz zur traditionellen entkoppelten Reglerauslegung mehrerer Umrichter wird in dieser Arbeit deren Kopplung explizit betrachtet. Zwei solcher Verfahren zur Auslegung der PDT-Regler jeder Umrichter werden entsprechend entworfen.

Schließlich wird ein Modell reduzierter Ordnung hergeleitet, das die wesentlichen Aspekte des dynamischen Verhaltens eines Niederspannungsnetzes mit dezentraler Erzeugung nachbildet.

Die Leistungsfähigkeit und die Grenzen der vorgeschlagenen Ansätze werden mittels Laborversuchen demonstriert.

1

INTRODUCTION

For more than a century, large power generating stations have delivered energy to a great amount of smaller distributed loads through several power systems across the world. But rising demand, new technologies, and environmental and reliability concerns are transforming the power grid, particularly through the incorporation of medium and small size generators based on renewable energy sources (RES), shifting the paradigm from a vertically operated system to a more horizontal one.

Moving to a more dynamic interconnected power system inherently enhances its performance since it enables power export between regions and shared load-coverage, making for a more robust grid. At the same time, further including small distributed energy resources (DER) based on RES maximizes the amount of green energy produced, eventually lowering costs and reducing our carbon footprint on the planet. However, changing the way power is generated and transported gives rise to new problems, which have to be thoroughly studied in order to guarantee a reliable energy supply in the future.

The magnitude and complexity of a large-scale power system, such as the European grid, makes an integrated analysis a demanding challenge, which requires appropriate modeling tools. A valid approach to studying such a system consists in analyzing the different processes that are present, observing the distinct time domains in which they take place. An example of the nature of such processes and their related time domains is shown in Fig. 1.1.

Complex phenomena down to the atomic level can be found for instance in a power semiconductor device, which needs extensive expertise in quantum mechanics for its modeling and understanding, while the study of market mechanisms and the demographics of energy consumption is related to sociology and strategic decision making, being game theory the preferred modeling tool. On the other hand, the construction of new generating stations and power lines relates

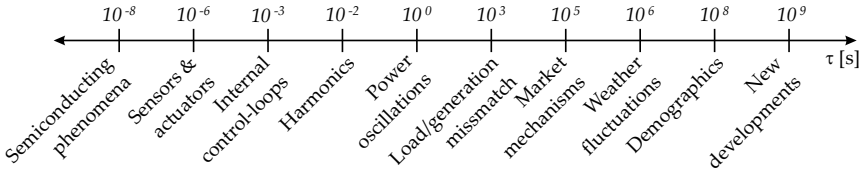

Figure 1.1: Several process present in a power system with different time domains.

to technological advances and political decisions, which are long-term developments usually hard to model or predict.

The diverse nature of these processes makes it necessary to model the related phenomena in each situation with different tools. In some cases, even new disciplines arise. For example, energy meteorology is a recent field of research interfacing renewable energy and atmospheric physics, which develops methods for the characterization of the fluctuating power output from RES [1]. In each case, the chosen modeling approach only makes sense in the context of a given system structure and a given time domain. For instance, modeling the dynamics of a power switch on a photovoltaic converter with more or less detail will not alter the quality of the model that predicts the amount of solar energy that will be available at a given point in time.

Focusing on one of these processes and its related time domain does not necessarily imply disregarding the rest of the system. Continuing with the example of the photovoltaic converter, a simplified aggregated model of the unit should be considered in order to contemplate power losses or maximum ratings that could indeed modify the solar energy prediction. Establishing the scope of such a model and defining its interface with the rest of the system is a key element of this modeling approach.

This work focuses on power oscillations in low-voltage (LV) grids with distributed generation (DG), which arise from dynamic interactions between power sources and can be found in the range of 1 to 10 Hz. Although the analysis presented in this work shall be extended to medium-voltage (MV) and high-voltage (HV) systems, the focus is stressed on LV grids since the dynamic processes are much more complex in that domain. Similar processes present in MV and HV systems are merely simplifications of the more general LV case.

In addition to the dynamics of the power sources, the factors that play a decisive role in the resulting oscillations are the provision of load-following energy and

the structure of the power system. Introducing these shall help understand the processes present on this time domain.

1.1 LOAD-FOLLOWING ENERGY AND FREQUENCY CONTROL

A very interesting aspect of the electrical power grid is the practical absence of energy storage, which implies that the amount of power produced at any given moment must exactly match the power consumed. Traditional power generating stations rely on producing electrical energy from some sort of potential energy, be it chemical or mechanical. In this sense, energy *is* initially stored and can be converted into electricity at a given rate. However, the inverse process of converting electrical energy into potential energy is usually not possible, either because the process used for the generation of electricity is not reversible or because the prime movers are designed to operate as generators but not as motors, compressors, or pumps. In this case, the only way of fictitiously storing energy is to reduce the amount of generation, which leaves fuel available for a later point in time. In the case of RES such as wind and solar, all energy has to be converted into electricity as it reaches the generator and there is no direct way of storing it.

Although some small-scale pilot projects with different storage technologies do exist [2], the current share of energy storage in power systems is rather negligible. As a consequence, some procedure to ensure the matching of supply and demand is imperative. There are several mechanisms that work to this goal, which operate on different time scales. On a seasonal and day-ahead basis, power generation is scheduled in advance according to forecasts. Many economical and regulatory issues are related to its scheduling and dispatch, which are not topic of this work. The coordination of several power generating stations is based on asynchronous communications between power providers and the transmission system operator, which orchestrate a generating schedule.

In a second-to-second basis, any deviation between forecasted and actual consumption must be constantly compensated for, producing more or less energy in accordance to the demand. Figure 1.2 shows the generation schedule for a simplified scenario with three generating stations that supply a given demand, as well as the actual consumption.

In order to supply this demand, every power imbalance between generation and load must be actively compensated. To do so, the power plants have to deviate from their schedule and slightly adjust their power output within short response times as the demand fluctuates. This additional amount of energy provided according to the actual demand is called *load-following energy*, sometimes referred

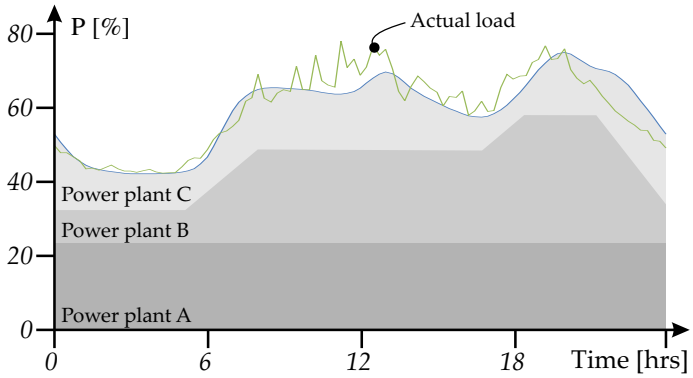

Figure 1.2: Scheduled generation and actual consumption as a percentage of installed capacity

to as *control energy* as well. Note that load-following energy can be either positive or negative, according to whether the scheduled generation exceeds or falls behind the actual demand.

On a rotating synchronous generator, this power imbalance translates naturally into an accelerating (or decelerating) torque, which changes rotating speed of the generator and hence the grid frequency. Should the local control loops of the generator not intervene, the frequency would further diverge and the generator would trip. To assure a stable operation, each generator features a governor that controls its frequency by simply changing the amount of energy supplied to the prime mover, which increases the electrical output of the generator. This is a classic example of proportional control and has been in operation since the very first days of power systems.

As a result, there is a coupling between the active power being generated (and hence consumed) and the grid frequency which acts as an indicator of the power balance in the system. A grid frequency lower than nominal represents excess of demand and accordingly lack of generation, while an increase in frequency signals the opposite situation. Because of this inherent coupling, the provision of load-following energy in order to match the demand is also known as *frequency control*.

In a similar manner, the terminal voltage of a generator is coupled to the reactive power it delivers through the exciter. If the terminal voltage decreases, the exciter will modify the excitation on the rotor to increase the reactive power output of the generator. The opposite happens if the voltage increases. Although different type

of control laws can be chosen, exciters are usually implemented as proportional controllers as well.

These steady state characteristics between frequency and active power, as well as between voltage and reactive power are called active and reactive droops respectively. A graphic representation of these droops is shown in Fig. 1.3. The slope of these lines result from the parameters of the governor and exciter. Modern systems based on power electronics instead of rotating generators achieve a similar behavior by implementing droop-controlled power inverters, which will be discussed in detail in Chapter 3.

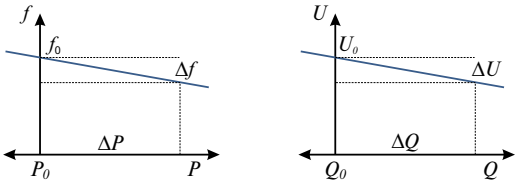

Figure 1.3: Active and reactive power droops

A distinction is made between primary, secondary, and tertiary frequency control. Primary control is achieved through the active power droop, while a deviation from scheduled active power results in a proportional deviation of the frequency. This type of control acts in a matter of seconds to prevent frequency decay, accelerating autonomously the generator to a new rotating speed. Secondary control acts as an outer control loop in order to restore to nominal frequency. This is a type of integral control which slowly shifts the droop line vertically in a way that the desired power output P is achieved at nominal frequency f_0. Finally, tertiary or peak-load control involves additional power plants that are brought in line, freeing capacity on all other generating stations.

As in almost every aspect of a power system, there are not only technological but also economical and regulatory issues related to the functioning of frequency control. These shall nonetheless remain uncovered in this work. For the purposes of power oscillations, the process of frequency restoration can be studied as outlined in Fig. 1.4.

In a system with DG, a load step ΔP produces an increase in the amount of power each generator produces which is proportional to the active power droop of each unit, while the frequency of the system changes until a new steady state value $f_0 - \Delta f$ is achieved. Although the steady state frequency is the same throughout the whole system, the instantaneous frequencies of the generators might differ over short periods of time, due to heterogeneous coupling between generators and

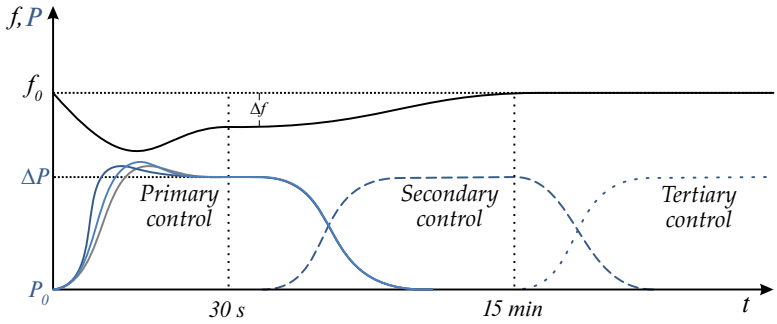

Figure 1.4: Outline of frequency control after a load step [3]

the large inertia of each unit which results in a lagged response. Consequently, all power stations contributing to frequency control interact with each other, which can yield stability issues. The different overshoots shown in Fig. 1.4 illustrate this effect. The frequency of all generators must settle within 30 seconds after a load step, while the transient response and the interactions between units must be stable and well damped.

Power generator interactions and so-called inter-area oscillations are a well known issue of primary frequency control [4]. The resulting low frequency oscillations are generally mild but can eventually lead to grid instability. In a future scenario with growing DG, these interactions become a rising problem, since a much larger number of smaller generators interact with each other through the MV and LV grids as well. Furthermore, the coupling between distributed generators is much different in lower voltage grids, since the inductive to resistive ratio of the power lines is completely different from those of a HV system. In order to assure a stable functioning of a future power system with large amounts of DG, the small-signal stability of this process needs to be better studied. The analysis of such oscillations constitutes the core motivation of this work.

1.2 MICROGRIDS AND VIRTUAL POWER PLANTS

Increasing integration of DER and the promotion of the smart grid is modifying the way electricity is generated and consumed. In some European countries like Germany, this development has been intensively supported by government laws, which have further accelerated the expansion of smaller DER at the MV and LV levels. Despite the benefits of DG based on RES, their penetration in the power system gives rise to new challenges. For instance, the intermittent nature of RES

and the resulting bidirectional power flows on existing power networks have a large impact on the operation of the grid.

Traditionally, DGs have been operated as grid-feeding units, acting as mere current sources that inject all power available blindly into the grid. This works out satisfactorily in a system with comparatively little integration of DER, but needs to be reviewed if the share of DG increases greatly as envisioned. The future power system will need to become more intelligent, and even new market models will have to be developed in order to successfully accommodate the new scheme in the existing infrastructure.

In order to handle and integrate DG in the power system, the ideas of microgrids (MG) [5] and virtual power plants (VPP) [6] have emerged. A microgrid is a localized group of DER that is normally connected to a traditional grid at a single point of common coupling (PCC). This system can operate as a grid-feeding unit or autonomously in case of a disconnection to the power grid. A virtual power plant is essentially an improvement to this concept, which consists in combining various small-size DG to form a single virtual generating unit that can behave as a conventional power plant, capable not only of feeding current into the grid but also of managing power flow between units and of providing frequency and voltage control.

A VPP operating solely in a given LV grid is electrically no different than a MG. In that case, the PCC is simply the transformer that interfaces the MV and LV grids. While a MG is usually operated with power droops only in islanded mode, a VPP providing frequency and voltage control implements power droops invariably. In the framework of this work, both MG and VPP alternatives will be addressed indistinctly as a LV grid with DG, since the focus will be set on the stability analysis of the system, which relates simply to the distributed implementation of power droops.

Another important aspect of modern DG is the inclusion of energy management systems (EMS). Such systems can operate a group of DER according to different targets which can be, for example, the minimization of the generation costs, maximization of the reliability of the system, or best use of RES. In this case, the power droops on the distributed units must be constantly modified, involving more or less load-following energy on each unit according to the optimization goals of the EMS.

1.3 STATE OF THE ART

When considering a number of medium and small size DER in a LV grid, some important issues regarding its proper and stable functioning arise. In particular, the stability of such a system is known to be dependent on the droop parameters of the power inverters [7–10], which in turn define as well the contribution of each inverter to frequency control and hence to system performance and efficiency. This raises the question of how to choose the droops in an optimal way without compromising the stability of the system. A valid approach is to vary their static droop parameters as needed to ensure a stable functioning of the system. This is usually done considering small-signal stability, finding a set of droops that yields a stable configuration [7, 8]. A more elaborate approach consists in taking into account other characteristics of the resulting system, such as reliability, efficiency, or costs of the energy that must be provided according to the chosen droop gain. Good examples of this are shown in [9, 10], where the droop gains in a MG are chosen in a way that fuel consumption is optimized while the resulting small-signal dynamics is stable. In doing so, the stability of the system becomes part of a set of constraints in a multivariable optimization problem which yields an optimal tradeoff between different aspects of a grid. Similar approaches can be found in the literature, with the goal of optimizing the droop gain in a way that the damping of the system is maximized [11–13].

Under the framework of an EMS, the selection of the units that make up a MG or VPP and the optimal configuration of its droops is itself a topic of great complexity. Intensive research is being carried out on the concepts of self-organized coalitions [14] and active rescheduling in real time [15], which will lead to flexible VPP based on RES in MV and LV grids. The solutions proposed in this area are usually numerically complex, even though generally no stability analysis is included. Further limiting these algorithms with stability constraints results frequently in ill-posed problems when considering real-world scenarios. As a result, there are often very few possible solutions to the optimization problem that fulfill all the necessary constraints. For instance, a group of inverters could be set to provide load-following energy with a given droop characteristic that maximizes the use of renewables available at the time or is optimal from an economical or operational point of view, yet the dynamics resulting from the chosen droop gains turns out to be unstable. In this sense, the droop parameters cannot be modified since they serve some other purpose, and the only alternative left to stabilize the system is to modify the local control loops of the inverters.

One effective means of achieving this is by a so-called improved droop controller, which incorporates a dynamic response to the otherwise static active power droop gain [16–20]. This approach is referred to as improved droop control [17], angle

droop control [18], phase-shift control [19], or transient droop control [20] in contrast to conventional droop control which governs merely the frequency of the inverter. Such an approach incorporates additional degrees of freedom, allowing the stabilization of the system even when unfavorable droops are selected. In this way, design considerations for static requirements of a MG or VPP can be decoupled from dynamic stability constraints [20]. Experimental results have shown in [21] the feasibility of this approach for a system with parallel inverters, but an analytical method to tune the dynamic droop gain in a system with DG is yet to be found.

1.4 AVOIDING REAL-TIME COMMUNICATION

Another interesting aspect of distributed generation is the communication requirements between inverters, which should be by all means minimized. Relying on real-time transmissions of inverter internal states would greatly degrade the reliability and robustness of the system, making the communication channel a vulnerable element. This renders some inverter control methods such as shown in [18] unsuitable for real-world large-scale applications, although laboratory tests under controlled conditions have shown good results. The authors in [22] have shown a three-inverter MG to be stable when controlled over an ideal wireless link, whereas a delay of 20 ms in the communication channel turned the system unstable. This was considering only a small-scale experiment, without packet losses and with the same delay for every inverter. Needless to say, the chances of such a control scheme to function robustly at large scale with current communication technologies are very low.

Although the resulting dynamics depends on all the variables of the system, each inverter should be stabilized only through feedback of the state variables that are locally measurable. At the same time, these controllers have to account for the stabilization of the interconnected system, which also depends on distributed parameters such as the coupling through the grid. In this sense, the controller strategy faces a contradiction, having to account for global effects but having access only to local variables.

Traditional state-space controller design with closed-form solutions such as pole placement and LQR turn out not to be implementable in this case, since not all of the system variables are available at a local level. However, communication is at the same time inevitable in an interconnected system. Even under the traditional power system structure there is an information exchange between the different generating stations and the system operator, although asynchronous and with low

real-time requirements. For example, network load flow calculations take place in order to avoid overloading the power lines and to establish transmission constraints due to the market outcome [23]. Once the process finishes, the related information is sent to the power stations and the system continues functioning without further communication.

In a similar way, the dynamics of the power inverters can be set with knowledge of the whole LV grid, while the resulting configuration is able to operate autonomously without real-time communication with the rest of the system. The stability of the system must still be evaluated for a selected configuration before tuning the inverters, but once a stable configuration is found, no further information exchange between inverters is necessary and the system can continue to function autonomously.

1.5 CONTRIBUTION AND STRUCTURE OF THIS WORK

Although much has been researched on the topic of traditional power system stability and many different solutions have been proposed, there have been none or very little references regarding the massive implementation of DG and its participation on the provision of frequency and voltage control. This thesis focuses on the small-signal stability of a LV grid with distributed droop-controlled generators and the possibility to better damp and even stabilize a system by properly implementing improved droop controllers.

The distribution of the power lines that make up the LV grid is supposed to be well known, as well as their admittance characteristics. Several distributed loads might be connected at different points of the grid, which can also be represented through admittance parameters. At some of the nodes of the grid there are inverters configured with a droop-controlled scheme. The energy source of each inverter (for instance wind, solar, batteries) is in this case indistinct, since the differences in availability and fluctuations are slower than the dynamic interactions analyzed in this work. Slower processes such as market mechanism and weather fluctuations will be considered exogenous to the models and their slow dynamics neglected, while faster processes such as the dynamics of the power lines and the internal control loops of a power inverter will be replaced with simplified models accordingly.

This work is organized as follows. A simplified model of a LV power grid will be derived in Chapter 2. The structure of a droop-controlled power inverter and its stability when connected to a stiff grid will be investigated in Chapter 3. To conclude the analysis of a single inverter, the improved droop controller will be

discussed in Chapter 4. A model for distributed generation in a LV grid will be derived in Chapter 5 and two methods to tune the improved droop controllers for a system with several generating units will be presented in Chapter 6. An aggregated reduced-order model of the LV grid with DG will be discussed in Chapter 7, which allows to extend the stability analysis performed in the LV grid hierarchically to the MV and HV levels. Finally, experimental results showing the performance of the proposed improved droop controllers will be shown in Chapter 8, followed by a concluding Chapter 9.

2

MODEL OF A LOW-VOLTAGE POWER GRID

One of the critical aspects that defines frequency stability on a given network is the electrical coupling between inverters. A valid grid model is in this sense of importance, in order to be able to derive conclusions on the dynamics of the system. Nevertheless, including the whole network or even a detailed section of it in the stability analysis comprises vast calculation power, while not gaining much insight on the functioning of the system itself, since most of the nodes on a distribution network are loads that can be considered constant in the scope of the oscillations between power inverters. The same is true for those nodes at which a power inverter is connected, when acting as a constant current source, not implementing power droops and hence not affecting the stability of the system other than changing the operation point. These loads and sources can be replaced by equivalent parameters, sacrificing only local information at those specific nodes, but not changing the global description of the system. One way of achieving this simplification is by grouping sets of passive nodes that are connected to each other and deriving equivalent admittance parameters, building π-pads that replace these groups of nodes. This process could be repeated iteratively until a minimal representation of the grid is found. However, recurring to some basic tools of linear algebra can greatly minimize this effort.

2.1 KRON REDUCTION OF AN ELECTRICAL NETWORK

Lets consider an arbitrary AC electrical network with m nodes and complex node voltages $\tilde{U}_{E_i}$, for $i = 1...m$. By writing the node equation in matrix form according to Kirchhoff's current law, the current $\tilde{I}$ injected at every node is related to the node voltages through the admittance matrix $\tilde{\boldsymbol{Y}}_{\boldsymbol{Net}}$, such that

$$\tilde{\boldsymbol{I}} = \tilde{\boldsymbol{Y}}_{\boldsymbol{Net}} \tilde{\boldsymbol{U}}_{\boldsymbol{E}}. \tag{2.1}$$

This admittance matrix is composed of the branch conductances that determine the coupling between nodes, and the shunt conductances that define the loads between nodes and ground. Its derivation is left out of this work, given its prevalence in the field [24].

The distribution transformer and those nodes to which an inverter providing ancillary services is connected form a subset of $n < m$ nodes. Arranging accordingly, the admittance matrix $\tilde{\boldsymbol{Y}}_{\boldsymbol{NetEq}}$ can be divided into four submatrices, and Eq. (2.1) can be rewritten as

$$\begin{pmatrix} \tilde{I}_1 \\ \vdots \\ \tilde{I}_n \\ \tilde{I}_{n+1} \\ \vdots \\ \tilde{I}_m \end{pmatrix} = \left(\begin{array}{c|c} \tilde{\boldsymbol{Y}}_{\boldsymbol{Net_{1,1}}} & \tilde{\boldsymbol{Y}}_{\boldsymbol{Net_{1,2}}} \\ \hline \tilde{\boldsymbol{Y}}_{\boldsymbol{Net_{2,1}}} & \tilde{\boldsymbol{Y}}_{\boldsymbol{Net_{2,2}}} \end{array}\right) \begin{pmatrix} \tilde{U}_1 \\ \vdots \\ \tilde{U}_n \\ \tilde{U}_{n+1} \\ \vdots \\ \tilde{U}_m \end{pmatrix} \tag{2.2}$$

The nodes $n+1$ to m are passive, i.e. they inject or consume power independently of the state of the grid and do not provide load following energy. The voltage at these nodes is determined by the voltages at the first n nodes, while the only current that flows is the one dictated by the admittance values. Considering this, Eq. (2.2) can be split into the equation system

$$\tilde{\boldsymbol{I}}_{\boldsymbol{1\ldots n}} = \tilde{\boldsymbol{Y}}_{\boldsymbol{Net_{1,1}}} \tilde{\boldsymbol{U}}_{\boldsymbol{E_{1\ldots n}}} + \tilde{\boldsymbol{Y}}_{\boldsymbol{Net_{1,2}}} \tilde{\boldsymbol{U}}_{\boldsymbol{E_{n+1\ldots m}}} \tag{2.3}$$

$$0 = \tilde{\boldsymbol{Y}}_{\boldsymbol{Net_{2,1}}} \tilde{\boldsymbol{U}}_{\boldsymbol{E_{1\ldots n}}} + \tilde{\boldsymbol{Y}}_{\boldsymbol{Net_{2,2}}} \tilde{\boldsymbol{U}}_{\boldsymbol{E_{n+1\ldots m}}} \tag{2.4}$$

The solution of this system for the currents $\tilde{\boldsymbol{I}}_{\boldsymbol{1\ldots n}}$ and voltages $\tilde{\boldsymbol{U}}_{\boldsymbol{1\ldots n}}$ is obtained by computing the Schur complement, resulting in the equivalent impedance matrix $\tilde{\boldsymbol{Y}}_{\boldsymbol{NetEq}}$, which allows for a compact representation of the net considering only the interaction between the first n nodes. The invertibility of $\tilde{\boldsymbol{Y}}_{\boldsymbol{Net_{2,2}}}$ is provided by physical properties of the admittance matrix [24].

$$\tilde{\boldsymbol{I}}_{\boldsymbol{1\ldots n}} = \underbrace{\left(\tilde{\boldsymbol{Y}}_{\boldsymbol{Net_{1,1}}} - \tilde{\boldsymbol{Y}}_{\boldsymbol{Net_{1,2}}} \tilde{\boldsymbol{Y}}_{\boldsymbol{Net_{2,2}}}^{-1} \tilde{\boldsymbol{Y}}_{\boldsymbol{Net_{2,1}}}\right)}_{\tilde{\boldsymbol{Y}}_{\boldsymbol{NetEq}}} \tilde{\boldsymbol{U}}_{\boldsymbol{E_{1\ldots n}}} \tag{2.5}$$

This reduction of an electrical network applying the Schur complement of the associated admittance matrix is known as Kron reduction, after the work of the Hungarian mathematician Gabriel Kron [25], who promoted the application of linear algebra in the electrical engineering field. The graph-theoretic properties

of the Kron reduction process and its resemblance with an iterative derivation of π-pads are studied in [26].

To illustrate this transformation, an arbitrary network with 12 nodes is presented in Fig. 2.1. In this example, the transformer is located at node 1, while three distributed power generators are placed at nodes 2, 3, and 4. Since their energy source is indistinct in the scope of small signal stability, the generators are here treated equally. All other energy sources and loads that do not provide ancillary services are represented through equivalent parameters, resulting in an admittance matrix $\tilde{\boldsymbol{Y}}_{\boldsymbol{Net}}$ of size 12×12.

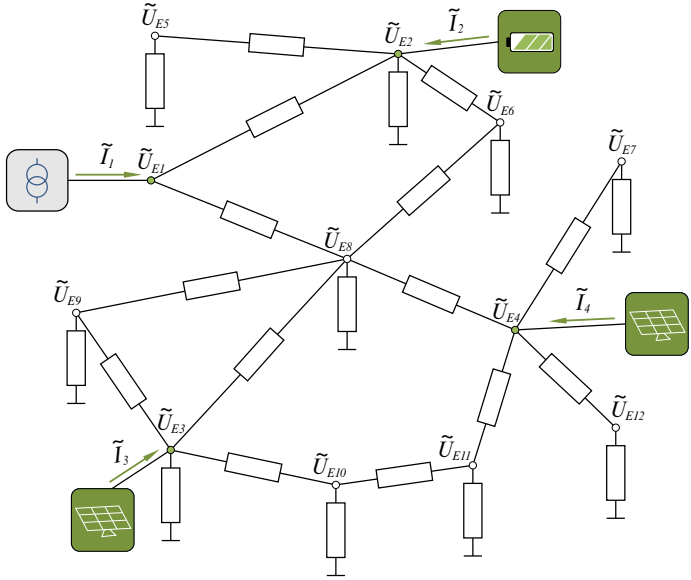

Figure 2.1: Arbitrary network representing a power grid with twelve nodes, one distribution transformer and three distributed power generators

Since only the interactions between nodes 1 to 4 are of interest, Eq. (2.5) can be applied to obtain the equivalent admittance matrix $\tilde{\boldsymbol{Y}}_{\boldsymbol{NetEq}}$, which describes the current of each power source as a function of their voltages. The elements of $\tilde{\boldsymbol{Y}}_{\boldsymbol{NetEq}}$ can be related to an equivalent minimal network rewriting the Kirchhoff's current equations in matrix form for these four nodes, which yields

$$\begin{pmatrix} \tilde{I}_1 \\ \tilde{I}_2 \\ \tilde{I}_3 \\ \tilde{I}_4 \end{pmatrix} = \begin{pmatrix} \tilde{Y}_{L1}+\tilde{Y}_{12}+\tilde{Y}_{13}+\tilde{Y}_{14} & -\tilde{Y}_{12} & -\tilde{Y}_{13} & -\tilde{Y}_{14} \\ -\tilde{Y}_{12} & \tilde{Y}_{L2}+\tilde{Y}_{12}+\tilde{Y}_{23}+\tilde{Y}_{24} & -\tilde{Y}_{23} & -\tilde{Y}_{24} \\ -\tilde{Y}_{13} & -\tilde{Y}_{23} & \tilde{Y}_{L3}+\tilde{Y}_{13}+\tilde{Y}_{23}+\tilde{Y}_{34} & -\tilde{Y}_{34} \\ -\tilde{Y}_{14} & -\tilde{Y}_{24} & -\tilde{Y}_{34} & \tilde{Y}_{L4}+\tilde{Y}_{14}+\tilde{Y}_{24}+\tilde{Y}_{34} \end{pmatrix} \begin{pmatrix} \tilde{U}_{E1} \\ \tilde{U}_{E2} \\ \tilde{U}_{E3} \\ \tilde{U}_{E4} \end{pmatrix} \quad (2.6)$$

The equivalent minimal network described by Eq. (2.6) is shown as a mesh of admittances in Fig. 2.2. If the transformer is considered as an ideal voltage source, any load parallel to it can be neglected. Otherwise, an equivalent impedance at the transformer could also be included.

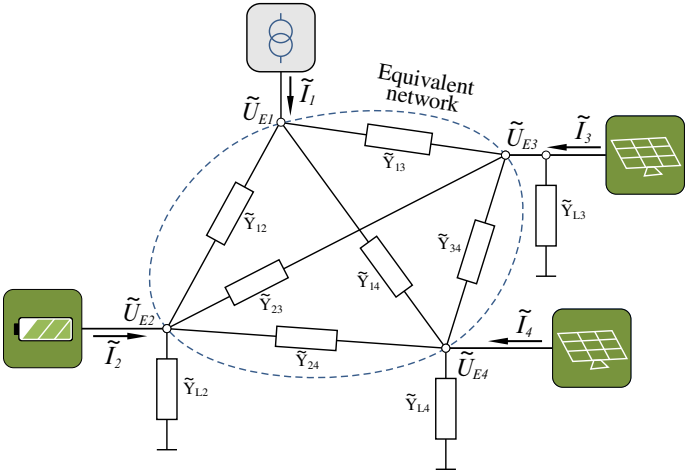

Figure 2.2: Mesh representation of the equivalent network

2.2 STAR AND MESH EQUIVALENTS

The proposed Kron transformation of the power grid results in the equivalent admittance matrix shown in Eq. (2.6), which can easily be interpreted graphically as seen in Fig. 2.2. This mesh representation arises naturally from the admittance parameters, giving an idea of the distribution of energy sources and loads, and their coupling in a given grid. The admittances *in parallel* to each node represent a portion of the combined effect of the distributed loads "as seen" at those nodes. On the other hand, the admittances *between* nodes define the coupling between energy sources, which is crucial in the study of oscillations.

This approach yields one admittance in parallel to each node, and $n-1$ admittances connecting it to each other. For a simple system with four nodes, this results in six parameters that define their coupling ($\tilde{Y}_{12}$, $\tilde{Y}_{13}$, $\tilde{Y}_{14}$, $\tilde{Y}_{23}$, $\tilde{Y}_{24}$, and

$\tilde{Y}_{34}$). For the general case, the number of coupling admittances is determined by the binomial coefficient

$$\binom{n}{2} = {}_nC_2 = \frac{n!}{2(n-2)!}, \tag{2.7}$$

which diverges as n grows, being the number of coupling admittances $\frac{n-1}{2}$ times the amount of nodes.

A different approach would be to think of a star representation of the system. In this case, nodes are not connected to each other but to an additional virtual point $\tilde{U}_0$, while their coupling is defined through two impedances in series, as shown in Fig. 2.3.

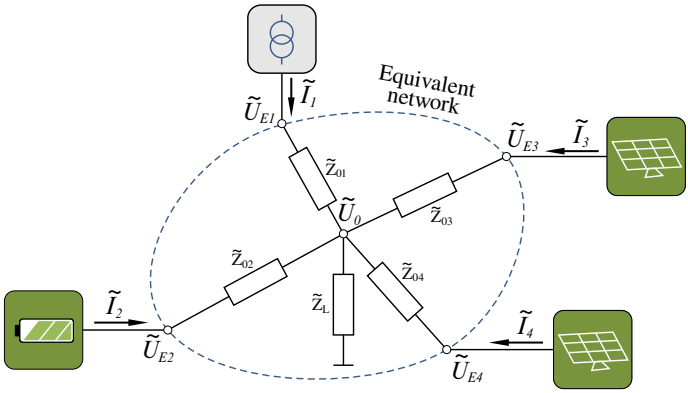

Figure 2.3: Assumed star representation of the equivalent network

This representation would minimize the amount of parameters needed for a given network, since there are as many coupling impedances as nodes. One might be seduced by this idea and try to find the inverse of the admittance matrix, looking for an equivalent star representation of the system. In fact, this is often done in power and electrical engineering for the case with 3 nodes, which yields the well-known delta-wye transformation. Unfortunately, this transformation is not possible for an arbitrary system with more than three nodes, since the converse of the star-mesh transformation does not always exist [27]. While the delta-wye transformation relates three impedances to three admittances, it is not always possible to transform a set of ${}_nC_2$ admittances into $n-1$ impedances without additional constraints. Furthermore, a single intermediate node $\tilde{U}_0$ might not have any physical significance in a distributed network, since its voltage could be undefined. Further mathematical and topological arguments for this can be found for instance in [28].

There are a few particular cases in which it is nonetheless possible to find this transformation, as determined in [29]. However, this imposes strong conditions on the topology of the network and the values of the admittances, which cannot be guaranteed for an arbitrary power grid. Therefore, the representation through a star equivalent shall not be used as a foundation for the study of interactions in a distributed power grid.

2.3 TYPICAL IMPEDANCE VALUES IN A LOW-VOLTAGE GRID

The following analysis will focus on a benchmark real-world low-voltage grid which has been available for studies within the scope of the project *Smart Nord* [30]. Applying a Kron reduction to such a benchmark system will give an overall idea on the typical impedance values that can be found.

The benchmark grid under consideration consists of 71 lines connecting 71 nodes to each other. The system is three-phase and is considered balanced. Details on its topology and the values of its elements can be found in Appendix I. The transformer which interfaces with the MV grid is connected at node number 1. An ideal voltage source will be considered at this node, although an equivalent impedance different from zero between LV and MV grids could be as well considered, which does not modify the analysis method presented in this work. The following 10 nodes are related to busbars, while the remaining 60 are connections to buildings, i.e. nodes 12 to 71.

2.3.1 *Single inverter connected to a stiff grid*

Since a power inverter could be connected at any of the 60 buildings, it is interesting to study the equivalent impedance between each of these nodes and the transformer. This value is crucial for the stability analysis of a single inverter connected to a stiff grid, as it will become clearer in Chapter 3. Applying the Kron reduction discussed before, a single equivalent impedance can be computed for every pair of nodes $\{1, i\}$, with $i = 12...71$. Each resulting impedance value determines the coupling between the chosen node i and the transformer, while all other nodes are considered as constant impedances. The magnitude and angle of these equivalent impedances can be seen in Fig. 2.4.

It is interesting to note that the phase angles of the equivalent impedances stay fairly constant in all cases, which is due to the resistive to inductive nature of the power cables that make up the grid. On the other hand, the magnitude varies

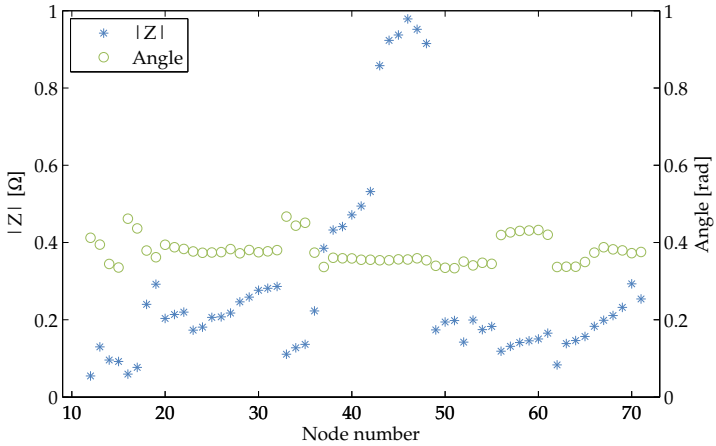

Figure 2.4: Value of the equivalent single impedance

from a few tens of $m\Omega$ up to 1 Ω. This is due to the fact that the buildings are distributed geographically in a neighborhood, which implies different total lengths of the power lines between a given building and the transformer. Furthermore, each section of the grid is made of cables of different categories, which yield different impedance parameters. Particularly interesting in this sense are nodes 43 to 48, which are the farthest from the transformer and at the end of a branch. This yields larger equivalent impedances not only because the distance between these nodes and the transformer is large, but also because the power cables chosen for this portion of the grid are of smaller cross section, which increases their impedance. Please refer to Appendix I for details on the types of power cable and for a graphical scheme of the grid.

Computing a mean value out of these equivalent impedances would help find the coupling between a power inverter and the stiff grid that is typically present in a LV system. However, the arithmetic mean might not yield a proper indicator of this, since individual data points, such as seen with nodes 43 to 48, skew the data set. For this reason, it is of better practice to use the median instead, so that these few extreme values do not distort what will be considered typical. The resulting median of these impedances is $\tilde{Z}_{med} = 0.202e^{0.374j}\ \Omega = 0.187 + j0.073\ \Omega$.

2.3.2 *Multiple inverters in parallel*

Although the analysis just presented results in a typical equivalent impedance for the coupling of a single inverter connected to a stiff grid, it could be argued that this value should differ when considering a grid with multiple power sources, since the coupling between inverters comes as well into play. These considerations are commonly left out when studying the stability of multiple inverters connected to a LV grid, since inverters are considered in a star configuration with a single impedance connecting them to an infinite bus at the PCC. However, as shown in the equivalent mesh representation of a LV grid of Fig. 2.2, there is not only an equivalent coupling between each inverter and the transformer ($\tilde{Z}_{12}, \tilde{Z}_{13}, \tilde{Z}_{14}$) but a coupling between inverters as well ($\tilde{Z}_{23}, \tilde{Z}_{24}, \tilde{Z}_{34}$). The latter shall be disregarded only if negligible with respect to the former, which is in fact not always the case.

In order to illustrate the significance of the coupling between inverters, a Kron reduction of the 71-node grid shall be computed for the case of three inverters operating in parallel. The equivalent grid is derived considering the transformer node and a selection of three of the 60 nodes at which an inverter could be connected. This is repeated for every possible combination of nodes, without repetition, resulting in ${}_{60}C_3 = 34220$ equivalent three-inverter grids. This yields a set of values that characterize the equivalent impedances possible in a real-world grid. Each of these equivalent grids has a unique set of six impedance parameters, which are composed of three inverter-to-transformer impedances ($\tilde{Z}_{12}, \tilde{Z}_{13}, \tilde{Z}_{14}$) and three inverter-to-inverter impedances ($\tilde{Z}_{23}, \tilde{Z}_{24}, \tilde{Z}_{34}$), such as seen in Fig. 2.2. It is worth to mention that some of these impedances are infinite and have to be removed from the data set, since a direct coupling between two nodes is not always present, as in the case of a simple series connection. As a result, 73273 inverter-to-transformer and 26197 inverter-to-inverter non infinite impedances are obtained.

Since in this case a scatter diagram such as the one shown in Fig. 2.4 would contain almost 10^5 points, it makes more sense to visualize the values of impedances by means of a histogram. Moreover, merely the absolute value of the impedances shall be studied, since the angle was shown to stay fairly constant. Fig. 2.5 shows the relative frequency of the absolute values of the impedances, which gives an idea of the empirical probability of a group of impedance values. To better deal with outliers, the histogram was computed using logarithmic binning [31].

The histogram shown is divided in inverter-to-transformer and inverter-to-inverter impedances. The median of the inverter-to-transformer impedances is $\tilde{Z}_{i-t} = 0.219e^{0.373j}$, which is very similar to the one obtained for the case of a

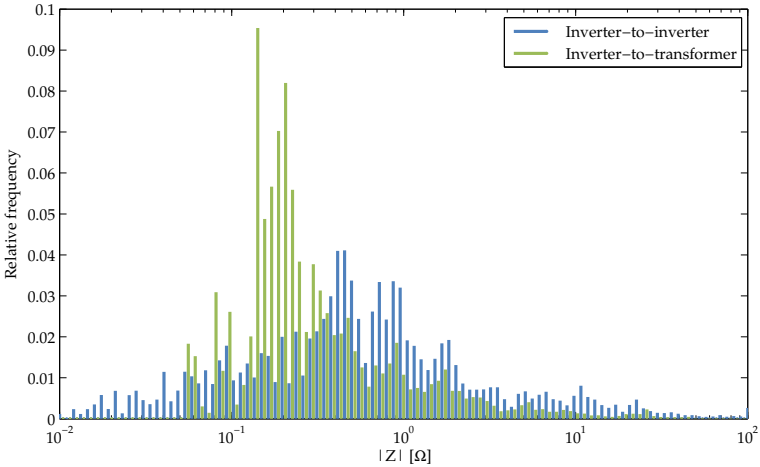

Figure 2.5: Normalized histogram of the absolute value of $(\tilde{Z})$

single inverter. On the other hand, the values of the equivalent inverter-to-inverter impedances are more spread and their median results in $\tilde{Z}_{i-i} = 0.506e^{0.353j}$, which is larger than $\tilde{Z}_{i-t}$. Even though larger impedance values decouple the inverters, it is the probability of smaller inverter-to-inverter impedances that has to be taken into account, since a coupling between inverters that is as strong or even stronger than the coupling with the stiff grid intensifies the interactions between them. From the histogram it follows that about a third of the resulting inverter-to-inverter impedances are equal or smaller than the average inverter-to-transformer coupling, which justifies the need of a proper network model contemplating inverter-to-inverter interactions when studying the effects of distributed generation in a LV grid.

This statistical analysis was kept rather simple and does not account for correlation between both groups of impedances, which could be further studied by means of Bayesian statistical methods. However, it is not the topic of this chapter - nor the focus of this thesis - to study the topology and statistical properties of LV grids, and the above should serve as a mere rule-of-thumb for the impedance values that will be used in the stability analysis on Chapter 3. A detailed analysis on grid topologies and their statistical properties can be found on [32, 33].

2.4 DEPENDENCE ON THE LOAD

The typical impedance values derived before were computed assuming constant impedances as loads, which were obtained from an average over a day of the load at each node as shown in Appendix II. However, the load in a LV grid is all but constant, and large variation can be observed within a day. Studying the statistical properties of such load variations allows for the generation of intra-day load profiles, which can be computed for winter, summer, and mid-season, as well as for residential, commercial, and industrial areas accordingly.

Of particular interest in Germany are the standardized load profiles defined by the BDEW [34]. Households with a maximum annual consumption of less than 8000 kWh are integrated into the so-called H0 profile, which exposes the typical load profile of a residential low-voltage grid at three different periods of the year. This benchmark profile has been averaged over many households and represents a smooth profile with typical load levels shown at 15 minute intervals.

This standard H0 load profile can be compared with that of the benchmark grid of Appendix II. For this purpose, the loads connected at each node of the benchmark grid were registered at an interval of 15 minutes during a whole day. The chosen day was April 14th, 2009, which was a Tuesday. The variation of the total load on the grid normalized by the mean annual load can be seen in Fig. 2.6, as well as the standard H0 profile for mid-season. Notice the correlation of both lines, particularly at early morning, noon, and evening, where the changes in load are more notable.

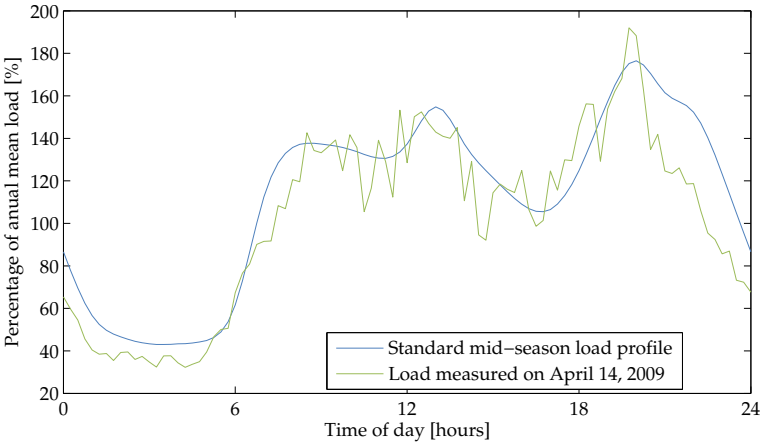

Figure 2.6: Variation of the load on a mid-season day

These intra-day variations of the load are reflected on the equivalent impedance values $\tilde{Z}_{i-t}$. To illustrate this, the equivalent impedances between the transformer and each single node can be computed as for the case of Fig. 2.4 but instead of using the mean value of the load, the measured load values for every 15 minute interval within the day shall be used. As a result, a varying impedance is obtained for each node, whose changes on their relative amplitudes are shown in Fig. 2.7 as a function of time.

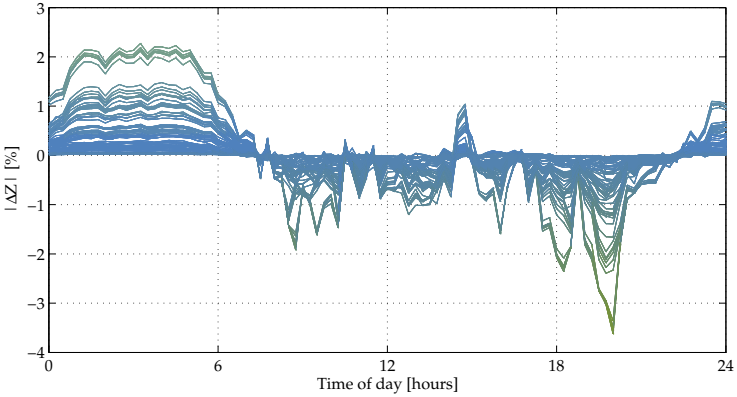

Figure 2.7: Intra-day relative change of the equivalent impedance

It is interesting to note that the resulting equivalent impedances $\tilde{Z}_{i-t}$ are inversely correlated with the load profile of Fig. 2.6. This is perfectly normal and expected, since power is inversely proportional to impedance and hence larger loads are related to smaller impedance values.

More interesting than this is the fact that the total variation of the equivalent impedances within a day is relatively small, bounded in most cases by about ± 2 %. The same stays true when studying different days of the year. These relatively small changes on the equivalent impedances are also logical from the point of view of the design of a power grid. If the impedance between two points changed considerably with the load, it would mean that there is a significant voltage drop and subsequent power loss in the line. Hence, the impedances of the lines have to be much smaller than those of the loads. This is very well known by the designers of power systems and considered at the time of dimensioning the grid, which is why the analysis with a real-world low-voltage grid yields such small changes of the equivalent impedances when the load varies.

With this in mind, the variations of the equivalent impedances with respect to the load can be safely disregarded, and the analysis can continue considering merely constant impedances between any two nodes of the grid.

3

MODEL OF A POWER INVERTER

Although there are different concepts for the design and control of a power inverter, this work focuses on the basic structure shown in Fig. 3.1, which comprises a traditional voltage source inverter (VSI) with current and voltage loops and an outer power loop that implements the droops. This structure has been widely implemented for distributed generation in MGs and for the provision of load-following energy in grid-connected LV networks [9, 16, 18, 20, 35–37].

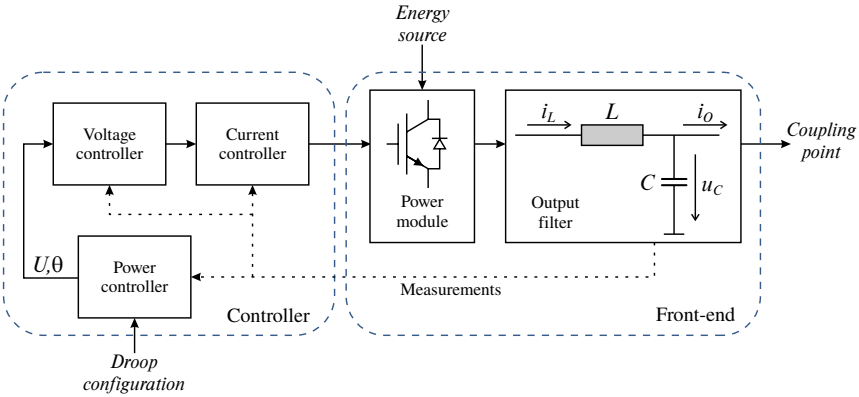

Figure 3.1: Basic structure of a power inverter

The inverter front-end consists of a power module and an output filter. The power module is typically composed of a B6 full bridge based on IGBTs with the related PWM drivers. The output filter is essentially a three-phase low-pass LC filter that limits the injection of harmonics into the grid. Some alternatives include a coupling inductor and even an output transformer, resulting in an LCL filter. However, in the scope of the present work this only changes the output impedance of the inverter, which can be introduced in series to the network model.

Current and voltage measurements are made on the filter, which are in turn used by the control system. The measurement of the output current i_O is omitted in some designs in order to reduce costs. This introduces error in the calculation of the output power, which has to be estimated in this case from the inductor current i_L. The same occurs when estimating the output voltage of the system in case an output impedance is present between the capacitor and the actual coupling point.

The inverter controller itself can be divided in two sections. On the one hand, the cascaded current and voltage controllers regulate the current i_L and the voltage u_C on the filter. This is normally achieved either with standard PI controllers in a grid-synchronous *dq* rotating reference frame or with PR controllers in an $\alpha\beta$ stationary reference frame, which are designed to damp the output filter and avoid high frequency disturbances. Some authors have proposed different configurations and improvements to these controllers, which range from the compensation of coupling effects in the filter [38] to the control of harmonic distortion [39]. In any case, the goal of these faster control loops is to ensure that the voltage at the coupling point follows the reference as smoothly and undistorted as possible, while the resulting bandwidth is in the order of a few hundred Hz.

The remaining section of the inverter controller is the power controller that generates the amplitude and phase of the voltage reference through the implementation of the power droops as an outer, slower control loop. The phase θ is related to the frequency f through an integration, such that

$$\dot{\theta} = \omega = 2\pi f, \tag{3.1}$$

while the frequency and amplitude are governed through the droop equations

$$f = f_{nom} - k_P(\hat{P} - P_{set}), \tag{3.2}$$

$$U = U_{nom} - k_Q(\hat{Q} - Q_{set}), \tag{3.3}$$

where f_{nom} represents the nominal frequency, U_{nom} the nominal voltage, P_{set} and Q_{set} the active and reactive power set-point, k_P and k_Q the droops, and $\hat{P}$ and $\hat{Q}$ the estimated active and reactive power at the coupling point.

The power estimation is normally achieved by averaging the instantaneous apparent power computed from the three phase voltages and currents measured locally, separating it into real (P) and imaginary (Q) parts. Under this scheme, the quadratic mean of the instantaneous power is not calculated over an exact period of the grid frequency as it should after definition of power for AC systems, but rather low-pass filtered with a bandwidth much smaller than that of the PWM

controller and the internal voltage and current control loops. This method is not exact and allows a small ripple in the estimation, but has extensively been tested and used as a decent estimator [16, 18, 35–37, 40–42]. As a result, the inverter behaves with the slower dynamics of the estimation filters, which also decouple the dynamics of the power controller from the faster internal control loops.

The estimations $\hat{P}$ and $\hat{Q}$ result from the instantaneous active and reactive power P and Q after a one-pole filter with time constants T_P and T_Q, such that:

$$\hat{P}(s) = \frac{1}{1 + sT_P} P(s), \tag{3.4}$$

$$\hat{Q}(s) = \frac{1}{1 + sT_Q} Q(s). \tag{3.5}$$

It is common practice to set both filter constants to

$$T_P = T_Q = \frac{1}{\omega_f}. \tag{3.6}$$

The constant ω_f is usually set to a tenth of the nominal frequency $\omega_{nom} = 2\pi f_{nom}$, with $f_{nom} = 50$ Hz in Europe, providing 20 dB of attenuation at this frequency.

3.1 SIMPLIFIED INVERTER MODEL

In order to study the dynamic behavior of an inverter, a detailed analysis could be considered, describing each portion of the structure shown in Fig. 3.1 with a set of differential algebraic equations. The authors in [37] derive a full small-signal state-space inverter model with this concept, resulting in a set of 13 state variables for a single inverter. However, different dynamic modes are shown to be present. High frequency modes are affected by the filter and the faster current and voltage controllers, while the more critical low-frequency modes that are of interest in an inverter dominated grid are mainly influenced by the frequency droops. The effects of the controllers and the filter's passive components are also taken into account in the modeling of the inverter in [16, 42], but both analytic and experimental results have shown that the dynamics related is in fact negligible with respect to the behavior of the grid-connected inverter [40, 41, 43]. Alternatively, these effects can be as well represented by a single equivalent inductor, which adds up nicely to the admittance parameters of the grid without need to modify the model [44].

With this in mind, the stability analysis of an inverter can be carried out in two separate ways. On the one hand, the stability of the internal current and voltage loops of a given inverter should be studied, considering the specifications of its output filter. Provided that the internal loops are stable and their bandwidth large enough, they can be simplified to a voltage source with adjustable amplitude and phase followed by an equivalent output impedance, which depends on the type of output filter and its control strategy. This yields a Thévenin equivalent of the inverter as seen in Fig. 3.2, whereas the equivalent voltage source features the dynamics of the slower power controller. In this way, a reduced model of a droop-controlled inverter is obtained, which only comprises three state variables. This allows to study the interactions between several inverters in a larger grid and keeps the simulation complexity to a minimum.

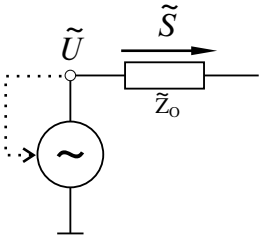

Figure 3.2: Thévenin equivalent of the voltage source inverter with droop controller

Considering this simplified approach, the dynamics of the inverter are merely described through the filter on the power controller of Eq. (3.4) and (3.5) together with the relationship between phase and frequency of Eq. (3.1) and the droop equations (3.2) and (3.3). The block diagram shown in Fig. 3.3 arises from these equations. The output impedance is not considered in this diagram since it can be taken into account together with the network model.

3.2 SYNCHRONOUS GENERATORS

The model discussed so far has been developed for a droop-controlled inverter with filtered active and reactive power estimators. Although there is no physical inertia in the power inverter, there is a lagged response caused by the filters, which resembles the natural reaction of a synchronous generator. Indeed, the proposed inverter model could also be adopted for this type of machine by simply adapting its parameters, as it will be demonstrated.

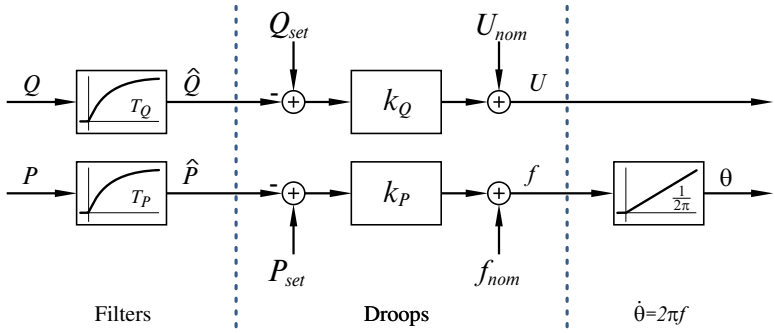

Figure 3.3: Simplified block diagram of a droop-controlled inverter

On the one hand, the parameters for the dynamics of the reactive power controller can be set directly. In this case, the reactive power droop coefficient is assigned according to Eq. (3.3), while the related constant T_Q is replaced with the equivalent exciter time constant.

On the other hand, the dynamics of the power controller can be derived by studying the rotor and governor equations as follows. A simplified diagram of a synchronous generator connected to a grid is shown for this purpose in Fig. 3.4.

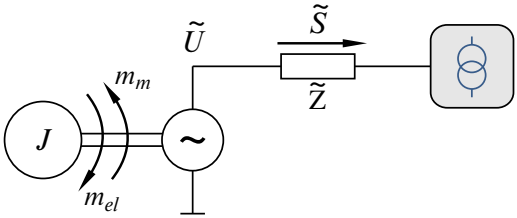

Figure 3.4: Simplified model of a synchronous generator

The input torque m_m is applied by the prime mover to the generator, which rotates with electrical frequency f. The generator delivers the active power P, which relates to the counter-reacting torque on the prime mover m_{el} through

$$P = 2\pi f m_{el} \tag{3.7}$$

Considering the equivalent moment of inertia J and neglecting losses, the rotor dynamics can be described by

$$J\ddot{\theta} = m_m - m_{el}. \tag{3.8}$$

Finally, the prime mover is controlled by a governor which implements the active power droop d, which can be written as a function of the set-point m_{set} and the nominal frequency f_{nom}:

$$m_m = m_{set} - d(f - f_{nom}). \tag{3.9}$$

Linearizing Eq. (3.7) and replacing in (3.8) and (3.9) yields the active power dynamics

$$J\ddot{\theta} = m_{set} - d(f - f_{nom}) - \frac{1}{2\pi f_{nom}} P + \frac{P_{set}}{2\pi f_{nom}^2} f. \tag{3.10}$$

This second order linear differential equation can be directly brought to the form in Fig. 3.3 with the equivalent parameters

$$T_P = \frac{4\pi^2 f_{nom}^2 J}{2\pi f_{nom}^2 d - P_{set}}, \quad k_P = \frac{f_{nom}}{2\pi f_{nom}^2 d - P_{set}}. \tag{3.11}$$

In this way, the slower dynamics of synchronous machines are brought to the same basic structure used for power inverters, simplifying the simulations with different types of generators.

3.3 DYNAMIC PHASOR MODEL

While operating with the traditional concept of phasors facilitates the analysis of power systems reducing the mathematical complexity of the model, it implies working in a stationary reference frame. This leads to the assumption that the frequency is constant and equal at every node of the grid, which is not well suited anymore in the case of a system with decentralized generation of load-following energy. To address this issue, the concept of dynamic phasors developed in [45] can be applied.

The main idea of the dynamic phasor model (DPM) is to derive a time varying Fourier coefficient for the fundamental frequency of each sinusoid. This makes it possible to include the dynamics of the power grid during transitions, whereas in steady state it becomes a standard phasor. The authors in [46] have shown that it is possible to extend this concept to higher order Fourier coefficients, which enables the analysis in unbalanced systems as well.

To derive the dynamic phasor model, the current through a transmission line in a balanced three phase system shall be studied, which can be represented by its equivalent single-phase model as shown in Fig. 3.5.

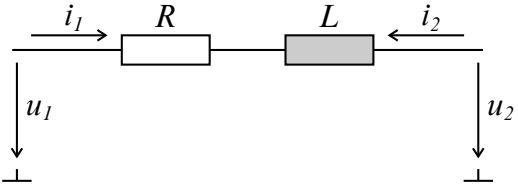

Figure 3.5: Single-phase model of a power line

The currents and voltages can be written as

$$u_1(t) = \sqrt{2}U_1(t)\sin(\omega_{nom}t + \theta_1(t)), \tag{3.12}$$

$$u_2(t) = \sqrt{2}U_2(t)\sin(\omega_{nom}t + \theta_2(t)), \tag{3.13}$$

$$i_1(t) = -i_2(t) = \sqrt{2}I(t)\sin(\omega_{nom}t + \phi(t)). \tag{3.14}$$

The terms U and I represent the effective values of the sinusoids, which shall vary with time, while their arguments are represented by a constant nominal angular frequency ω_{nom} plus a term that varies with time as well.

Writing the Kirchhoff's voltage law equation for the line of Fig. 3.5 results in

$$u_1 - u_2 = Ri + L\frac{di}{dt}. \tag{3.15}$$

Replacing with Eqs. (3.12) through (3.14) and dividing by $\sqrt{2}$ yields

$$U_1\sin(\omega_{nom}t+\theta_1) - U_2\sin(\omega_{nom}t+\theta_2) = RI\sin(\omega_{nom}t+\phi) + L\dot{I}\sin(\omega_{nom}t+\phi) + LI\omega_{nom}\cos(\omega_{nom}t+\phi) + LI\dot{\phi}\cos(\omega_{nom}t+\phi). \tag{3.16}$$

Making use of Euler's formula and simplifying the term $e^{j\omega_{nom}t}$, it follows

$$U_1e^{j\theta_1} - U_2e^{j\theta_2} = (R + j\omega_{nom}L)Ie^{j\phi} + L\dot{I}e^{j\phi} + LIj\dot{\phi}e^{j\phi}, \tag{3.17}$$

which can be rewritten using complex notation as

$$\tilde{U}_1 - \tilde{U}_2 = (R + j\omega_{nom}L)\tilde{I} + L\dot{\tilde{I}}. \tag{3.18}$$

In the traditional quasi-static representation, the rightmost term of this formula is ignored, assuming that the dynamics of the phasor is negligible. This holds true for most power systems, considering the slow dynamics of large power generators and their coupling through MV and HV grids. However, this may not be the case in LV grids with faster reacting power inverters. Studying these effects further provides a better understanding of the dynamics of a phasor in a general case.

Rearranging Eq. (3.18) and considering $\tilde{I} = \tilde{I}_1 = -\tilde{I}_2$ results in the equation

$$\tilde{I}_1 = \frac{1}{(R + j\omega_{nom}L)}\left(\tilde{U}_1 - \tilde{U}_2\right) - \frac{1}{(R/L + j\omega_{nom})}\dot{\tilde{I}}_1, \tag{3.19}$$

$$\tilde{I}_2 = \frac{1}{(R + j\omega_{nom}L)}\left(\tilde{U}_2 - \tilde{U}_1\right) - \frac{1}{(R/L + j\omega_{nom})}\dot{\tilde{I}}_2. \tag{3.20}$$

The block diagram shown in Figure 3.6 can be derived from these equations considering vector notation, being $\tilde{\boldsymbol{Y}}_{\boldsymbol{Eq}}$ the admittance matrix of the quadripole in Fig. 3.5. The dynamic phasor model can then be included in series to the traditional admittance matrix and be later added easily to the nonlinear model, as it will be discussed in Chapter 5. Thanks to vector notation, this model can also be extended for several nodes, and even load dynamics can be studied with this approach considering ground as another node.

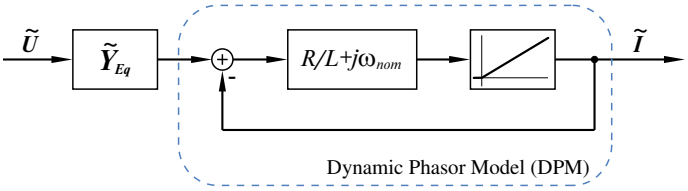

Figure 3.6: Admittance matrix and dynamic phasor model

Since the voltages $\tilde{U}$ and the currents $\tilde{I}$ are (complex) causal signals that vary with time, Eq. (3.18) can be rewritten in the Laplace domain, which yields

$$I(s) = (U_1(s) - U_2(s))\,\frac{1}{R + j\omega_{nom}L + Ls} \tag{3.21}$$

This equation suggests a single complex pole of value $-(R/L + j\omega_{nom})$ to be present on the system. However, care should be taken when analyzing this result, keeping in mind that the state variable $\tilde{I}$ of this model is also complex. This actually yields two state variables, since the integration over time of a complex variable implies two integrations along the real and imaginary components.

Having found an expression for the dynamics of the current through a line, it is of interest to find a similar expression for the dynamics of active and reactive power related to it, since the power controller of the inverter works based on the power flow and not on its current. With this purpose, the apparent power S flowing into a node can be computed from

$$\tilde{S} = P + jQ = \tilde{U}\tilde{I}^*, \tag{3.22}$$

where $\tilde{S}$, $\tilde{P}$, $\tilde{Q}$, $\tilde{U}$, and $\tilde{I}$ are functions in the *time* domain.

The authors in [47] and [48] analyze the related power dynamics directly on the Laplace domain, neglecting some basic mathematical properties of this approach. In the first place, the Laplace transform of instantaneous active and reactive power is not equal to the product of the Laplace transforms of voltage and current. In fact, the power flow should be calculated in the s-domain through the limit of the complex convolution

$$S(s) = \frac{1}{2\pi j} \lim_{T\to\infty} \int_{\varsigma-jT}^{\varsigma+jT} U(\varsigma) I^*(s^* - \varsigma^*) d\varsigma$$

which has to be performed along the vertical line $Re\{\varsigma\} = c$ within the region of convergence of $U(s)$ [49]. Therefore, dealing with power and energy variables in the Laplace domain is better avoided, given its mathematical complexity.

In order to better understand the dynamics of power flow, the expression of apparent power in the time domain shown in Eq. (3.22) can be linearized. The prefix Δ denotes the linearized state, whereas the partial derivatives must be evaluated at the linearization point.

$$\Delta P = \frac{\partial P}{\partial \tilde{U}} \Delta\tilde{U} + \frac{\partial P}{\partial \tilde{I}^*} \Delta\tilde{I}^* \tag{3.23}$$

$$\Delta Q = \frac{\partial Q}{\partial \tilde{U}} \Delta\tilde{U} + \frac{\partial Q}{\partial \tilde{I}^*} \Delta\tilde{I}^* \tag{3.24}$$

Rewriting these equations for both nodes of the power line yields:

$$\Delta P_1 = I_r \Delta U_{1r} + I_i \Delta U_{1i} + U_{1r} \Delta I_r + U_{1i} \Delta I_i \tag{3.25}$$

$$\Delta Q_1 = I_r \Delta U_{1i} - I_i \Delta U_{1r} + U_{1i} \Delta I_r - U_{1r} \Delta I_i \tag{3.26}$$

$$\Delta P_2 = -I_r \Delta U_{2r} - I_i \Delta U_{2i} - U_{2r} \Delta I_r - U_{2i} \Delta I_i \tag{3.27}$$

$$\Delta Q_2 = -I_r \Delta U_{2i} + I_i \Delta U_{2r} - U_{2i} \Delta I_r + U_{2r} \Delta I_i \tag{3.28}$$

where the suffixes $_r$ and $_i$ denote real and imaginary parts.

The linearized current ΔI can be rewritten from Eq. (3.19) in a similar manner, resulting in

$$L\Delta\dot{I}_r = \Delta U_{1r} - \Delta U_{2r} - R\Delta I_r + \omega_{nom} L\Delta I_i, \tag{3.29}$$

$$L\Delta\dot{I}_i = \Delta U_{1i} - \Delta U_{2i} - R\Delta I_i - \omega_{nom} L\Delta I_r. \tag{3.30}$$

Recall here that the frequency ω_{nom} represents the constant portion of the instantaneous frequency, whereas its variations in time are contemplated in the phase θ.

Last, the amplitude and phase of the voltage at each node can be introduced through the variables ΔU and $\Delta\theta$, linearizing the functions $U_r = U\cos\theta$ and $U_i = U\sin\theta$:

$$\begin{pmatrix} \Delta U_{1r} \\ \Delta U_{1i} \\ \Delta U_{2r} \\ \Delta U_{2i} \end{pmatrix} = \underbrace{\begin{pmatrix} \cos\theta_1 & -U_1\sin\theta_1 & 0 & 0 \\ \sin\theta_1 & U_1\cos\theta_1 & 0 & 0 \\ 0 & 0 & \cos\theta_2 & -U_2\sin\theta_2 \\ 0 & 0 & \sin\theta_2 & U_2\cos\theta_2 \end{pmatrix}}_{\boldsymbol{T}} \begin{pmatrix} \Delta U_1 \\ \Delta\theta_1 \\ \Delta U_2 \\ \Delta\theta_2 \end{pmatrix} \tag{3.31}$$

The equations (3.23) through (3.31) allow for a state space model of the line:

$$\begin{pmatrix} \Delta\dot{I}_r \\ \Delta I_i \end{pmatrix} = \boldsymbol{A} \begin{pmatrix} \Delta I_r \\ \Delta I_i \end{pmatrix} + \boldsymbol{BT} \begin{pmatrix} \Delta U_1 \\ \Delta\theta_1 \\ \Delta U_2 \\ \Delta\theta_2 \end{pmatrix} \tag{3.32}$$

$$\begin{pmatrix} \Delta P_1 \\ \Delta Q_1 \\ \Delta P_2 \\ \Delta Q_2 \end{pmatrix} = \boldsymbol{C} \begin{pmatrix} \Delta I_r \\ \Delta I_i \end{pmatrix} + \boldsymbol{DT} \begin{pmatrix} \Delta U_1 \\ \Delta\theta_1 \\ \Delta U_2 \\ \Delta\theta_2 \end{pmatrix} \tag{3.33}$$

with

$$\boldsymbol{A} = \begin{pmatrix} -R/L & \omega_{nom} \\ -\omega_{nom} & -R/L \end{pmatrix} \tag{3.34}$$

$$\boldsymbol{B} = \begin{pmatrix} 1/L & 0 & -1/L & 0 \\ 0 & 1/L & 0 & -1/L \end{pmatrix} \tag{3.35}$$

$$\boldsymbol{C} = \begin{pmatrix} U_{1r} & U_{1i} \\ U_{1i} & -U_{1r} \\ -U_{2r} & -U_{2i} \\ -U_{2i} & U_{2r} \end{pmatrix} \tag{3.36}$$

$$\boldsymbol{D} = \begin{pmatrix} I_r & I_i & 0 & 0 \\ I_i & -I_r & 0 & 0 \\ 0 & 0 & -I_r & -I_i \\ 0 & 0 & -I_i & I_r \end{pmatrix} \tag{3.37}$$

Defining the resistive to inductive ratio of the line $\nu = R/(\omega_{nom}L)$, the characteristic equation of the linearized system can be written as

$$det(\lambda \mathbf{1} - \boldsymbol{A}) = \lambda^2 + 2\nu\omega_{nom}\lambda + \omega_{nom}^2(\nu^2 + 1) = 0. \tag{3.38}$$

An interesting implication arises from the analysis of the eigenvalues λ of this equation. Opposite to what intuition might suggest, the resulting phasor dynamics depend merely on the resistive to inductive ratio ν of the line and not on its length. Nor plays the operating point any role on the resulting poles. The eigenfrequency and damping ratio of the pole pair can be seen in Fig. 3.7 for different values of ν. For the classical case in LV grids where $R \approx \omega_{nom}L$ ($\nu \approx 1$), this analysis yields an eigenfrequency of 71 Hz with a damping ratio of 0.71. The damping decreases for more inductive grids, while the lower limit of the eigenfrequency is the nominal frequency of 50 Hz. For resistive grids, the system becomes faster and better damped.

3.4 MODEL VERIFICATION

In order to validate the proposed simplified model, the benchmark system of Fig. 3.8 is studied, which consists of a single inverter connected to a stiff grid. The voltage at the transformer is therefore considered as an ideal voltage source with adjustable amplitude and phase. The output impedance of the inverter is set to $\approx$ 1 mH (0.3 Ω), which is an average value of the output filters implemented by different authors [16, 21, 37, 40]. An equivalent load of 10 kW is connected in parallel to the inverter, while an impedance $\tilde{Z} = 0.2 + 0.1j\ \Omega$ represents the equivalent coupling between the inverter and the transformer as discussed in Chapter 2.

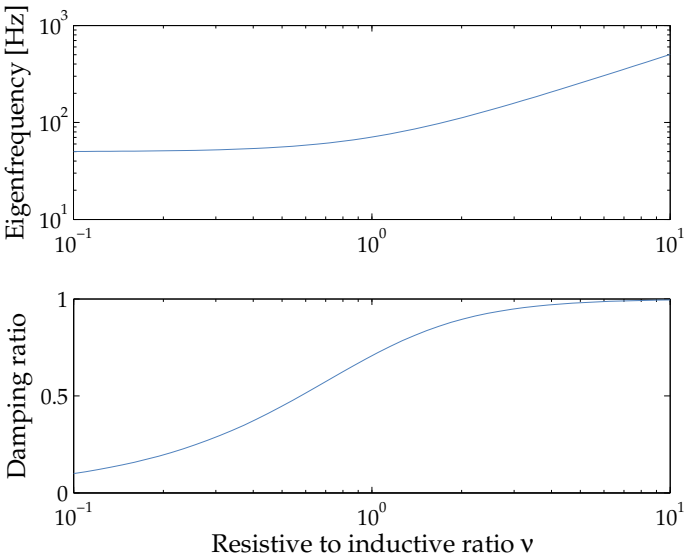

Figure 3.7: Eigenvalue resulting from the DPM as a function of ν

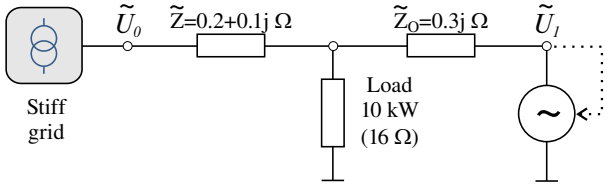

Figure 3.8: Single inverter connected to a stiff grid

The detailed small-signal state-space model deduced in [37] is implemented as a reference model, which has been proven to accurately reproduce the behavior of a real power inverter. Simulations are then compared with the proposed model with and without DPM.

For the system of Fig. 3.8, the detailed model in [37] delivers 15 state variables, 10 of which stem from the internal control loops of the inverter, 3 from the power controller, and 2 from the coupling through the grid. On the other hand, the proposed model makes use of only 3 state variables in its simplest form, or rather 5 state variables when including dynamic phasors. Considering a stiff grid, there are no state variables related to the power flow at the transformer node, since they are linear combination of the state variables at the inverter.

The power controller is set with the same control parameters as in [37], namely

$$k_P = 1.5\text{e-}5 \text{ Hz/Watts}, \quad k_Q = 1.3\text{e-}3 \text{ V/var}, \tag{3.39}$$

$$T_P = T_Q = 3.14\text{e-}2 \text{ s}. \tag{3.40}$$

The output inductance of the inverter is considered in series to the grid model, from which the equivalent admittance matrix is obtained:

$$\tilde{\boldsymbol{Y}}_{\boldsymbol{eq}} = \begin{pmatrix} 0.876 - 1.365j & -0.855 + 1.374j \\ -0.855 + 1.374j & 0.897 - 1.384j \end{pmatrix}. \tag{3.41}$$

The nominal inverter voltage is chosen so that no power is initially delivered by the inverter, which results in

$$U_{nom} = 392.57. \tag{3.42}$$

In order to compare the performance of these three models, a frequency drop of 100 mHz at the transformer is simulated. Moreover, the simulation is repeated increasing and decreasing the active power droop $\pm 50\%$, which alters the stationary values reached. The power delivered by the inverter can be seen in Fig. 3.9 for the three models in these cases.

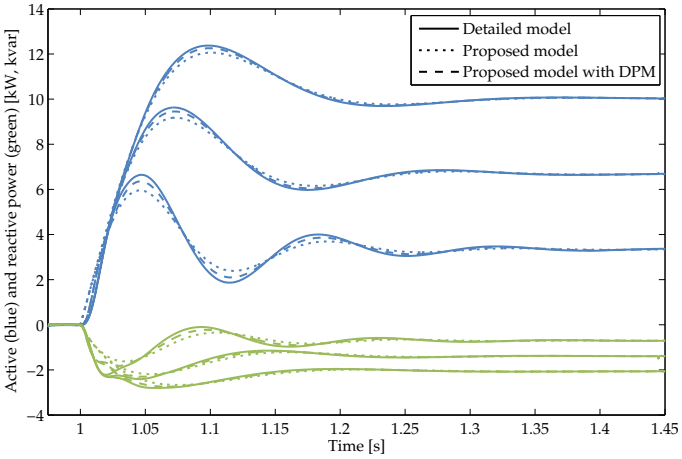

Figure 3.9: Active and reactive power delivered by the inverter after a frequency drop of 100 mHz at the transformer.

A voltage drop of 20 V at the transformer is simulated as well, producing the results shown in Fig. 3.10.

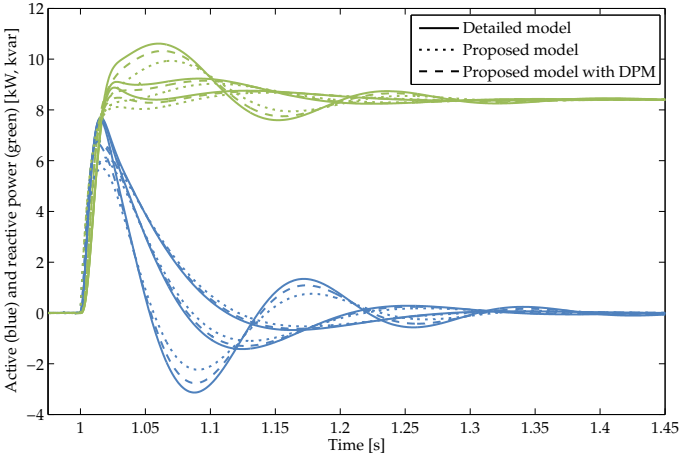

Figure 3.10: Active and reactive power delivered by the inverter after a voltage drop of 20 V at the transformer.

In all cases, the proposed model follows the detailed model appropriately. Some inevitable deviations can be recognized during the first few milliseconds, which are caused by neglecting the faster internal control loops of the inverter and the output filter dynamics. After these initial differences, all three models continue to behave in the same way.

Integrating dynamic phasors certainly improves the modeling but intrinsically adds two state variables, which increases the computational power needed to study the system. This is not an issue when considering only one inverter, but might play a decisive role in the simulation of larger interconnected systems. Furthermore, the improvement on the model is minimal, considering the frequency range of the phasor dynamics and that of the interactions in a typical LV power grid. Since phasor dynamics were proven to be in the order of 70 Hz, with an absolute minimum of 50 Hz, they shall be further neglected, as long as the resulting dynamics of the power system continue to be in the lower range of a few hertz.

3.5 STABILITY ASSESSMENT OF A SINGLE INVERTER CONNECTED TO A STIFF GRID

Even though the stability of an isolated inverter does not in any way guarantee that several such inverters will be stable when connected together to the same LV grid, studying it can illustrate and help understand the effects that different parameters have on the dynamics of the system. For this purpose, a simplified setup is considered, consisting of a single and balanced three-phase inverter connected to an ideal stiff grid through a single impedance. The single-phase equivalent of such system is shown in Fig. 3.11. The voltage phasors at the transformer and inverter nodes can be written as $\tilde{U}_0 = U_0$ and $\tilde{U}_1 = U_1 e^{j\theta_1}$ respectively.

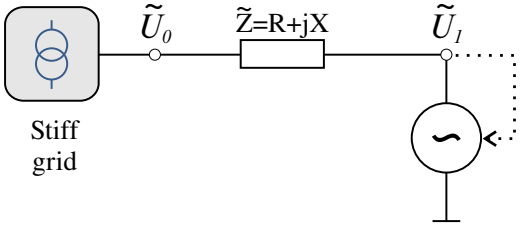

Figure 3.11: Single inverter connected to a stiff grid.

Recalling Eqs. (3.1) through (3.5), the dynamics of the power inverter can be described by the integral relationship between frequency and phase and the power droop equations, according to

$$f = f_{nom} - k_P(\hat{P} - P_{set}), \tag{3.43}$$

$$U = U_{nom} - k_Q(\hat{Q} - Q_{set}), \tag{3.44}$$

$$\dot{\theta} = \omega = 2\pi f, \tag{3.45}$$

together with the first-order power estimation dynamics, which are normally written directly in the s-domain as

$$\hat{P}(s) = \frac{\omega_{f_P}}{s + \omega_{f_P}} P(s) \text{and} \tag{3.46}$$

$$\hat{Q}(s) = \frac{\omega_{f_Q}}{s + \omega_{f_Q}} Q(s), \tag{3.47}$$

$$\tag{3.48}$$

where $\omega_{f_P} = 1/T_P$ and $\omega_{f_Q} = 1/T_Q$.

The power flow out of the inverter can be expressed as

$$P = \frac{1}{R^2 + X^2} \left(RU_1^2 - RU_0U_1 \cos(\theta_1) + XU_0U_1 \sin(\theta_1) \right), \tag{3.49}$$

$$Q = \frac{1}{R^2 + X^2} \left(XU_1^2 - XU_0U_1 \cos(\theta_1) - RU_0U_1 \sin(\theta_1) \right). \tag{3.50}$$

These two equations can be linearized at a given point $\tilde{U}_{0l} = U_{0l}$, $\tilde{U}_{1l} = U_{1l}e^{j\theta_{1l}}$, resulting in the linear relationships

$$\Delta P = k_{PU}\Delta U_1 + k_{P\theta}\Delta\theta_1, \tag{3.51}$$
$$\Delta Q = k_{QU}\Delta U_1 + k_{Q\theta}\Delta\theta_1, \tag{3.52}$$

with

$$k_{PU} = \frac{1}{R^2 + X^2} \left(2RU_{1l} - RU_{0l} \cos(\theta_{1l}) + XU_{0l} \sin(\theta_{1l}) \right), \tag{3.53}$$
$$k_{P\theta} = \frac{1}{R^2 + X^2} \left(RU_{0l}U_{1l} \sin(\theta_{1l}) + XU_{0l}U_{1l} \cos(\theta_{1l}) \right), \tag{3.54}$$
$$k_{QU} = \frac{1}{R^2 + X^2} \left(2XU_{1l} - XU_{0l} \cos(\theta_{1l}) - RU_{0l} \sin(\theta_{1l}) \right), \tag{3.55}$$
$$k_{Q\theta} = \frac{1}{R^2 + X^2} \left(XU_{0l}U_{1l} \sin(\theta_{1l}) - RU_{0l}U_{1l} \cos(\theta_{1l}) \right). \tag{3.56}$$

Replacing the power estimation dynamics of Eq. (3.46) and (3.47), it follows:

$$\Delta\hat{P} = \frac{\omega_{f_P}}{s + \omega_{f_P}} (k_{PU}\Delta U_1(s) + k_{P\theta}\Delta\theta_1(s)) \tag{3.57}$$
$$\Delta\hat{Q} = \frac{\omega_{f_Q}}{s + \omega_{f_Q}} (k_{QU}\Delta U_1(s) + k_{Q\theta}\Delta\theta_1(s)) \tag{3.58}$$

Closing the loop related to the reactive power droop replacing equation (3.44) yields

$$\frac{\Delta\hat{P}(s)}{\Delta\theta_1(s)} = \frac{\omega_{f_P}}{s + \omega_{f_P}} G_Q(s) \tag{3.59}$$

with

$$G_Q(s) = \frac{k_{P\theta}s + \omega_{f_Q}(1 + k_Q(k_{QU}k_{P\theta} - k_{Q\theta}k_{PU}))}{s + \omega_{f_Q}(1 + k_Q k_{QU})}. \tag{3.60}$$

Further closing the loop with the active power droop equation (3.43) leads to the known closed-loop dynamics of a single inverter connected to a stiff grid, as

shown for instance in [41]. However, studying the open-loop dynamics at this point allows for a better insight on the behavior of the system. Fig. 3.12 shows an equivalent block diagram for the single inverter connected to a stiff grid, highlighting the linearized equations of power flow through the line and the equivalent closed-loop dynamics of the reactive droop controller.

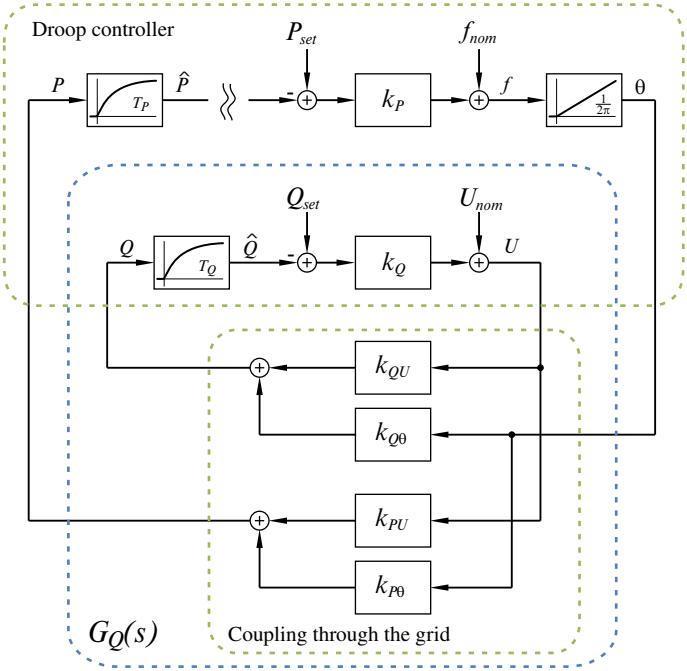

Figure 3.12: Open-loop diagram for a single inverter connected to a stiff grid

The open-loop transfer function of this system can be written as

$$G_{open}(s) = \frac{2\pi k_P}{s} \frac{\omega_{f_P}}{s + \omega_{f_P}} G_Q(s). \tag{3.61}$$

This transfer function does not necessarily have any physical meaning, since the loop is cut open at $\hat{P}$, which is an internal variable of the inverter's controller. In a similar way, the analysis could be carried on by closing the active power loop first and the reactive power loop thereafter. Nonetheless, this sets a base for the later improvement of the active power controller and some interesting properties related to the dynamics of the inverter can be investigated in this way. For instance, the value of the line impedance $\tilde{Z}$ does not appear directly on the

open-loop equation (3.61) but indirectly through a pole-zero pair in $G_Q(s)$. The location of this pole and zero depends on the line parameters k_{PU}, $k_{P\theta}$, k_{QU}, and $k_{Q\theta}$, which in turn depend on the impedance $\tilde{Z}$ and the linearization point as shown in Eqs. (3.53) to (3.56). This linearization might be affected by the choice of the linearization point, yielding erroneous values that could distort the stability analysis.

It was shown in Chapter 2 that the equivalent impedance on a power grid is practically unaffected by changes on the load. However, the linearized line parameters do not only depend on the equivalent resistance R and reactance X but also on the operating voltages U_{0l} and U_{1l}, as well as on the inverter phase θ_{1l}, which define the linearization point. Before studying the sensitivity of the linearized parameters to changes on the voltages and phase that define the linearization point, it is necessary to estimate the admissible range in which they can vary.

Assuming a constant transformer voltage $U_{0l} = 400\ V$ and a maximal voltage deviation of 10 %, the inverter voltage U_{1l} may vary between 360 and 440 V. This is usually the case in a power grid, since the maximal voltage deviation is regulated and has to be guaranteed. On the other hand, the analysis is not as straightforward for the inverter phase θ_{1l}. In MV and HV power networks, the maximum phase difference is known to be bounded by $\pi/2$ to avoid generator tripping. However such a large phase difference might not be possible in a LV grid, since the lines are much shorter and current flow is limited. To illustrate this effect, lets analyze the current that flows through the line, which can be written as

$$I_l = \frac{U_{0l} - U_{1l}e^{j\theta_{1l}}}{R + jX}. \tag{3.62}$$

The absolute value of this current can be expressed as

$$|I_l|^2 = \frac{(RU_{0l} - RU_{1l}\cos(\theta_{1l}) - XU_{1l}\sin(\theta_{1l}))^2 + (XU_{0l} - XU_{1l}\cos(\theta_{1l}) + RU_{1l}\sin(\theta_{1l}))^2}{R^2 + X^2} \tag{3.63}$$

which is essentially similar to the equation of a cone. Fig. 3.13 shows the magnitude of the current as a function of the inverter voltage and phase for a line of impedance $\tilde{Z} = 0.2 + 0.1j\ \Omega$.

It is interesting to note that the current through the line rapidly reaches a magnitude of over 300 A for a phase difference of ± 0.1 radians. This limits intrinsically the admissible phase difference, since the lines that make up a LV grid are usually rated at a maximum of 100 to 300 A. With this in mind, the following analysis will focus on a voltage domain of $400 \pm 40\ V$ and a phase domain of ± 0.1 radians.

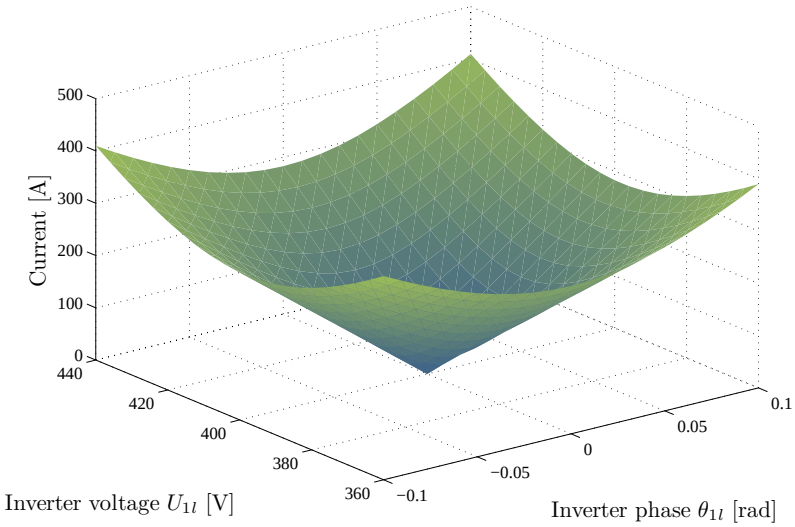

Figure 3.13: Absolute value of the current for a variation of the inverter voltage and phase

The location of the pole and zero of $G_Q(s)$ can be computed for every linearization point within the mentioned admissible domain. Fig. 3.14 shows the values of the pole and zero given the reactive droop value of Eq. (3.39). Note in the z-axis that the filter frequency ω_{fQ} was factored out when computing the pole and zero. The resulting pole of $G_Q(s)$ is about 1.2 times faster than the filter frequency ω_{fQ}, while the zero is 1.4 times faster than ω_{fQ}. Their relative change remains within a 10 % band for the whole domain. Although this might seem quite a large error caused by wrongly choosing the linearization point, moving from one extreme of the domain to the other means having a maximum voltage of $440\ V$ and $300\ A$ flowing in one direction to a minimum of $360\ V$ and $300\ A$ flowing in the opposite direction, which is a massive error in the estimation of the operating point of the system. Therefore, the influence of the linearization point on the resulting dynamics shall be further neglected.

It should also be noted in Eq. (3.60) that for the case of no reactive power droop ($k_Q = 0$) the pole and zero in $G_Q(s)$ directly cancel each other, while increasing the droop value moves the pole-zero pair to a higher frequency range and farther apart from each other. No reactive droop means that the inverter voltage has to be kept constant, which is clearly optimal for the stability of the system but might

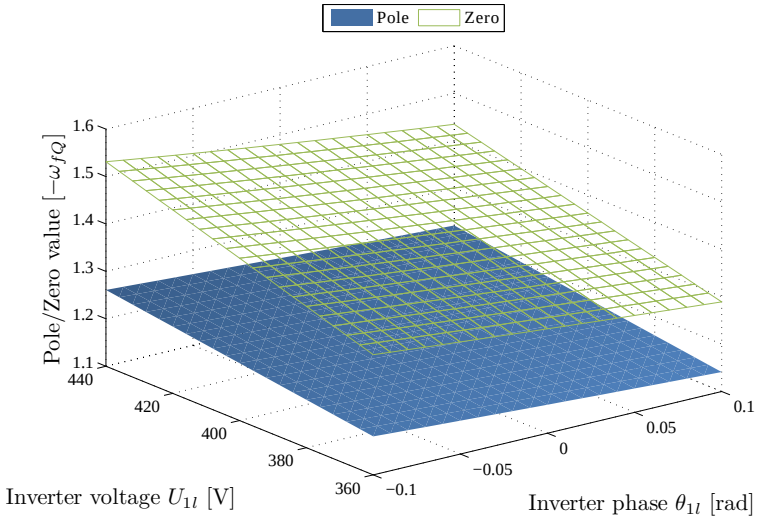

Figure 3.14: Pole and zero value of $G_Q(s)$

in turn yield to saturation of the power inverter, having to provide large amounts of power to prevent small voltage deviations. On the other hand, a larger value of the reactive power droop diminishes the reactive power requirements but yields larger voltage deviations and a faster response which might lead to unstable behavior due to interaction with unmodeled dynamics.

The value of the line impedance $\tilde{Z}$ has the opposite effect on Eq. (3.61). A larger impedance implies a looser coupling of the inverter to the grid, which moves the pole and zero in $G_Q(s)$ closer together, as seen in Eq. (3.60). Smaller values of $\tilde{Z}$ signal a stronger coupling of the inverter with the rest of the system, resulting in faster and worse damped dynamics on $G_Q(s)$.

The influence of the bandwidth ω_{fP} and ω_{fQ} of the power filters should also be considered when studying the stability of an inverter. Most authors set both active and reactive power filter dynamics equal to a tenth of the nominal frequency of the grid, or even lower [16, 18, 21, 41]. This is motivated by the necessity of filtering out possible ripple in the power estimation due to power harmonics and unbalance, as well as limiting the bandwidth of the input of the inverter's voltage controller. A larger bandwidth is therefore not desired. However, the implications of yet slower filter dynamics should be as well studied.

The family of Nyquist plots of $G_{open}(s)$ shown in Fig. 3.15 helps illustrate the impact that changing some of the inverter's parameters has on closed-loop stability.

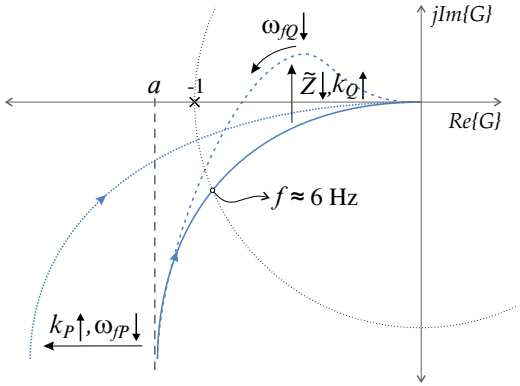

Figure 3.15: Family of Nyquist plots of $G_{open}(s)$ for different parameters

The solid line shown in Fig. 3.15 reflects the typical characteristic of the system, which is obtained implementing the inverter with the parameters shown in [37] and a line impedance of $\tilde{Z} = (0.2 + 0.1j)\ \Omega$. Since the active power droop k_P acts as a gain in $G_{open}(s)$, increasing it simply scales up the plot, as shown with the dotted line. The similar happens when decreasing ω_{fP}, which moves the asymptote a farther to the left (see Appendix II for a detailed analysis on this). In both cases the system remains stable, although its relative stability decreases, which can be noticed on the intersection with the unit circle and the resulting decreased phase margin.

The presence of the pole and zero in $G_Q(s)$ is difficult to tell apart, since both result almost equal for the inverter parameters considered. Hence, the shape of the Nyquist plot resembles that of a first-order lag element with integrator, which is absolutely stable in closed loop. However, increasing the reactive power droop k_Q or decreasing the line impedance $\tilde{Z}$ separates the pole-zero pair in $G_Q(s)$ as discussed before. Since the pole in Eq. (3.60) is always slower than the zero, an increase and later decrease of the phase in clockwise direction can be observed, creating a small hump as shown with the dashed line. This could yield enough phase shift so as to jeopardize the stability of the system. Note that a proper selection of both droop gains could make the plot encircle the point $(-1, 0)$, turning the closed-loop system unstable.

Although the stability of an inverter results clearly dependent on the selection of the droop gains, this work focuses on the possibilities of stabilizing the inverter

without modifying these droops. Both modifying the droop gains and changing the output impedance of the inverter can alter the dynamic response of the inverter, but this also modifies the nominal power deviation given a variation on the voltage or frequency, which shall remain unchanged in the scope of this work.

In order to cope with probable unstable behavior of the inverter caused by unfavorable droops, the dynamics of the power controller could be modified. One way of achieving this is by decreasing the reactive power filter bandwidth ω_{fQ}, which makes the pole-zero pair in $G_Q(s)$ slower. Note that the intersection with the unit circle corresponds to a frequency of about 6 Hz for the given choice of inverter parameters, while this value normally lies between 1 and 10 Hz for LV grids [16, 37, 40, 41, 43, 50, 51]. Sufficiently decreasing ω_{fQ} moves the hump on the Nyquist plot to a lower frequency range, assuring that the phase of the open-loop transfer function $G_{open}(s)$ never surpasses $180°$. This is a simple solution that can help avoid instability but it cannot guarantee a good damping of the closed-loop poles, since the intersection with the unit circle does not move to the right. A more elaborate strategy must be employed for this purpose, which will be covered in the next Chapter.

3.6 INCREASING THE SYSTEM'S INERTIA

It has been argued in the last years that the stability problems of an inverter-dominated grid are merely related to a decrease in the system's inertia. With this background, many authors have proposed inverter structures that mimic the functioning of a synchronous generator, coining terms such as VISMA (Virtual Synchronous Machine) [52], VSG (Virtual Synchronous Generator) [53], and Synchronverters [54]. The droop-controlled power inverter is itself a variation of this approach, given that the resulting dynamics are equivalent (recall the analogy between droop-controlled power inverters and synchronous generators on Section 3.2).

Since in a power inverter there is no physical inertia that stores kinetic mechanical energy that could be injected back into the grid if needed, electrical potential energy has to be secured in exchange. There are two main options that can be used for this purpose. The first one is to include some sort of storage in the power inverter, which is usually done in the form of batteries connected to the DC bus. The second option is to operate the inverter below its optimal operation point, which leads to a large waste of energy in the case of renewable sources. The selection of one or the other of these strategies makes a difference in costs and

efficiency of the system, but does not affect its small signal stability, provided that a given equivalent inertia can be guaranteed.

However, the *size* of this equivalent inertia has a direct impact on the system's dynamics. The traditional argument holds that a larger inertia has a stabilizing effect on the grid, since more energy can be injected in the event of a disturbance. This neglects the fact that increasing the inertia makes the system slower, as shown in Eq. (3.11). This slower behavior yields a worse damped system, which is shown through the Nyquist plot in Fig. 3.15. In the end, the larger the inertia the greater the phase lag in the feedback loop of a second order system which is naturally prone to oscillate.

Some other controller structure should explore the possibilities of stabilizing the system without necessarily adding more virtual inertia but rather systematically modifying the response of a simple rotating generator to exhibit a more complex dynamic behavior that can successfully damp the system. The analysis of such a controller is the topic of Chapter 4

4

IMPROVED DROOP CONTROLLER FOR A SINGLE INVERTER

The basic idea behind the improved droop controller is to compensate for the slow dynamic response of the inverter by adding an additional term to the active power droop controller. Instead of using the conventional droop equation [41,55–57]

$$\Delta\dot{\theta} = -2\pi k_P \Delta\hat{P}, \tag{4.1}$$

a power-dependent term is added directly to the phase θ [16–20], which becomes

$$\Delta\theta = -2\pi k_P \int \Delta\hat{P} dt - k_{Pd}\Delta\hat{P}. \tag{4.2}$$

This control structure can be considered a PI controller acting on the phase θ of the inverter, as seen in Fig. 4.1. The physical relationship between phase and frequency together with the droop gain k_P is seen here as an integral controller, while a proportional gain is added in parallel to improve the dynamic response. The gain k_P is referred to as the static droop gain, while k_{Pd} is called the dynamic droop gain. A further extension of this scheme implemented as a PID controller was demonstrated in [16], although the inclusion of the derivative term did not show any remarkable improvement on the closed-loop dynamics of the system and could even give rise to an unwanted response in high frequency bands, partially compensating the low-pass behavior of the power filters and amplifying noise due to harmonics and unbalance.

To better understand the functioning of this controller, it helps to review some aspects of power generation with conventional synchronous generators [4,58]. The power injected by a generator is a nonlinear function of the rotor displacement angle or *load angle*. Given a drop in load, the generator has to accelerate in order to achieve a new load angle and then decelerate to maintain this operating point. Accordingly, a rise in load pushes the load angle in the other direction. The large inertia of the generator makes a sudden change in load angle impossible, which

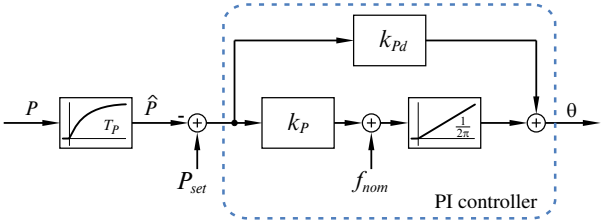

Figure 4.1: Improved active power droop implemented as a PI controller

in turn makes the rotor being pulled into the new load angle to overshoot and oscillate around it with decreasing amplitude. Since a droop-controlled inverter mimics a synchronous generator, the same oscillatory behavior can be observed in this case. Nevertheless, the overshoot is not caused by a physical inertia but due to the delayed response of the active power filter. The role of the dynamic droop gain k_{Pd} is to compensate for this delayed action by providing a direct path between power and phase. This helps the virtual load angle to shift to a new operating point according to the injected power. As a result, the load angle stabilizes faster and the oscillations are damped. A similar effect is achieved traditionally by the damper winding in a synchronous generator, which provides magnetic flux to compensate the transient relative motion between the rotor and stator.

It is important to note that the zero associated to the PI controller could cancel the pole at $\omega_{fP} = 1/T_P$ on the filter, giving the false impression that the inverter does not present any dynamics. This could give rise to unmodeled dynamics and instability due to the response of the inverter's internal current and voltage control loops. Furthermore, even when pole and zero do not exactly compensate each other, the bandwidth of the input to the inverter's internal controller should be limited in order to avoid noise and ripple to be fed back into the system. For this purpose, another first-order low pass filter with time constant T_{Pl} can be added to the controller. The constant T_{Pl} should be chosen to limit the bandwidth of the controller, which can be achieved for instance with $T_{Pl} = T_P/20$. If this pole is not added in the implementation of the controller, there will still be a dominant pole on the system in that frequency range, which stems from the internal voltage controller in closed loop. This is normally not considered, since most authors configure their inverters in a way that the resulting poles of the droop controller lay in a frequency range much lower than the bandwidth of the voltage controller, but it must be nonetheless considered in the stability analysis to study possible interactions with the droop controller, as it will become apparent in the following paragraphs.

Another way of studying the improved droop structure is as a PD controller. Rewriting Eq. (4.2) in the Laplace domain yields

$$\Delta\theta = -\left(\frac{2\pi k_P}{s} + k_{Pd}\right)\Delta\hat{P} \tag{4.3}$$

which can in turn be rewritten as

$$s\Delta\theta = \Delta\omega = -2\pi k_P G_{PD}(s)\Delta\hat{P} \tag{4.4}$$

with

$$G_{PD}(s) = 1 + \frac{k_{Pd}}{2\pi k_P}s \tag{4.5}$$

This simplifies the integration with the conventional droop controller since, instead of modifying the controller structure, a simple element is added in series.

Although an ideal PD controller is not realizable, this could be implemented together with the low pass filter to form a causal subsystem. In this way, instead of implementing the PD controller as such, an equivalent behavior is obtained with a phase lead controller.

It is also crucial that the lead controller has a unity gain at lower frequencies, ensuring that the inverter will operate with the selected power droop k_P in steady state. The resulting transfer function of this controller can be expressed as

$$G_{lead}(s) = \frac{1 + T_{Pd}s}{1 + T_{Pl}s}, \tag{4.6}$$

with

$$T_{Pd} = \frac{1}{\omega_d} = \frac{k_{Pd}}{2\pi k_P}. \tag{4.7}$$

The resulting block diagram of the improved active power droop implemented as a lead controller can be seen in Fig. 4.2, which illustrates the addition of a controller block in series to the conventional droop scheme.

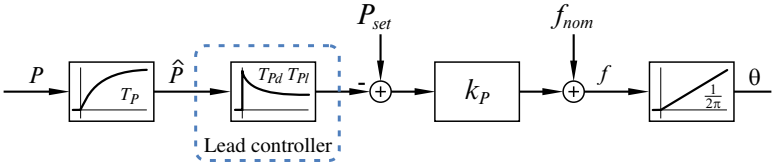

Figure 4.2: Improved active power droop implemented as a lead controller

4.1 DAMPING CAPABILITIES OF THE IMPROVED CONTROLLER

The effect that this controller has on the stability of the inverter can be clearly shown by means of a Nyquist plot. The solid line in Fig. 4.3 recalls the Nyquist plot of $G_{open}(s)$ as shown in Fig. 3.15 while the dashed line shows the Nyquist plot of $G_{open}(s)G_{lead}(s)$.

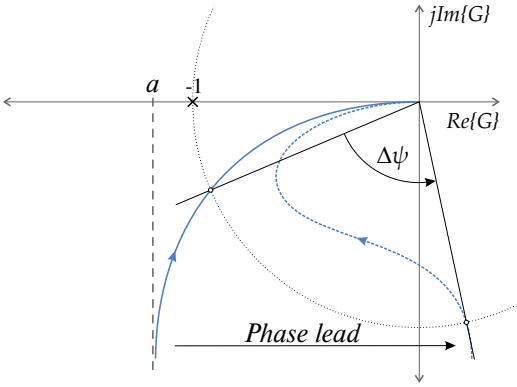

Figure 4.3: Nyquist plot of $G_{open}(s)$ (solid) and $G_{open}(s)G_{lead}(s)$ (dashed).

The damping capability of the improved droop becomes clear by looking at the intersection with the unit circle, observing an increase $\Delta\psi$ in the phase margin. Moreover, it is worth noting that a larger droop gain k_P or a slower filter constant ω_{fP}, which were shown in Fig. 3.15 to decrease the damping, could as well be implemented provided that the lead controller is set in a way that enough phase margin is allowed. Setting this parameter correctly is therefore crucial to assure an adequate damping of the system, which will be discussed in the following Section.

4.2 STABILITY ASSESSMENT OF A SINGLE INVERTER WITH IMPROVED DROOP CONTROLLER

Several authors have shown experimentally that the improved droop controller can successfully damp a given power inverter when the dynamic droop gain k_{Pd} is properly tuned [16, 17, 20, 35, 59, 60], but a fundamental groundwork yielding a simple analytical criterion for its optimal choice is up-to-date missing. In order to derive a proper method to tune this controller, lets consider the closed-loop diagram of Fig. 4.4.

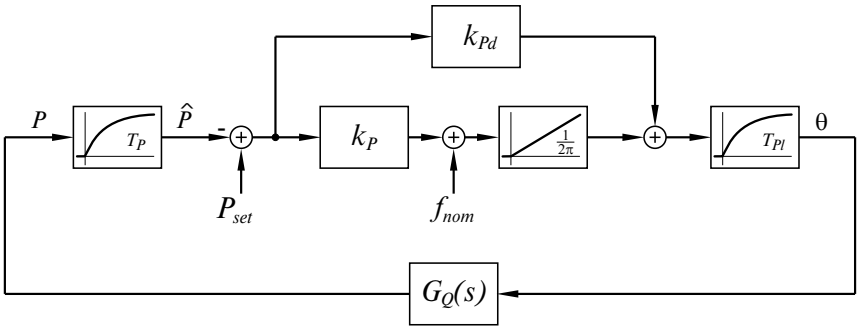

Figure 4.4: Equivalent block diagram of a single inverter with improved droop controller

This block diagram shows the equivalent dynamics of a single inverter connected to a stiff grid. The improved droop is implemented as a PI controller, while a second low-pass filter with time constant T_{Pl} was included as discussed before. The element $G_Q(s)$ introduces the closed-loop behavior of the reactive power controller when the inverter is connected to a stiff grid, as discussed in Chapter 3.

Two main paths can be recognized from this diagram. On the one hand, the integral branch of the PI controller represents the conventional droop relating the instantaneous frequency of the inverter to the power injected. On the other hand, the proportional branch generates an offset in the phase as a function of the power. To further understand how the dynamic droop gain affects the closed-loop dynamics of the inverter, this diagram can be reshaped as seen in Fig. 4.5 and the loop can be cut open at the output of the gain k_{Pd}.

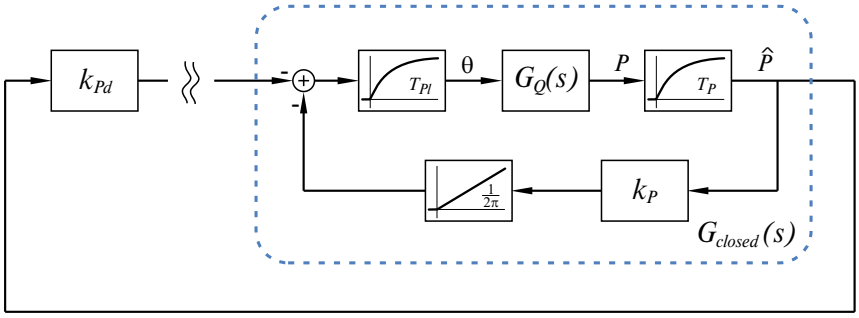

Figure 4.5: Reshaped block diagram of a single inverter with improved droop controller

The section outlined in blue and the related transfer function $G_{closed}(s)$ represent the closed-loop dynamics of the conventional droop-controlled inverter. If no improved droop was implemented ($k_{Pd} = 0$), the outer loop remains open and the poles of $G_{closed}(s)$ determine the stability of the inverter. However, closing the loop with the improved droop gain k_{Pd} affects the location of the poles of $G_{closed}(s)$, which can be made clear through the root locus plot of Fig. 4.6.

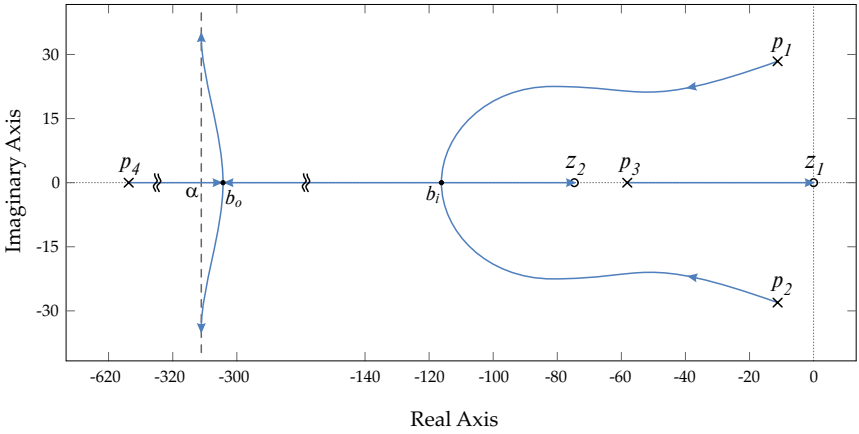

Figure 4.6: Root locus of $G_{closed}(s)$

The open-loop complex pole pair p_1, p_2 signals a poorly damped response of the inverter without improved droop. A zero z_1 appears at the origin due to the presence of the integrator in the feedback path, while the higher frequency pole p_4 originates from the band-limiting low-pass filter with time constant T_{Pl}. If this second low-pass filter was not implemented, an equivalent pole p_4 would still exist, governed by the limited bandwidth of the inverter's internal voltage and current loops. The pole-zero pair p_3, z_2 stems from the reactive power closed loop $G_Q(s)$.

A higher gain k_{Pd} increases the damping of the poles p_1, p_2, while p_3 shifts to the right becoming slower. With a proper choice of the gain, both p_1 and p_2 can be located at the break-in point b_i yielding a critically damped response. Further increasing the gain separates the pole pair, shifting one pole to the right towards z_2 and the other to the left. Notice that a break-out point b_o appears between p_4 and b_i, and there are two asymptotes with centroid α and depart angle of ± 90 degrees. Care should be therefore taken when selecting a large loop gain, which can yield high frequency oscillatory behavior due to the interaction with p_4.

4.3 DEPENDENCE ON THE STATIC DROOP GAINS

The root locus plot of Fig. 4.6 was derived for the inverter parameters shown in [37]. However, it is important to make sure that the root locus remains qualitatively similar for other droop values k_P and k_Q before formalizing a method for finding the optimal gain k_{Pd}. With this purpose, the root-contour (family of root-loci) shown in Fig. 4.7 is introduced. In this plot, the root-loci of $G_{closed}(s)$ are shown for different droop values. The first plot shown in Fig. 4.6 is kept in black as a reference. The blue lines show the new root-loci when varying the active power droop, while the green lines represent a change in reactive power droop. In order to allow for a qualitative comparison of these plots, each root locus plot was scaled horizontally in a way that the zero z_2 is located at the same place in the graphic.

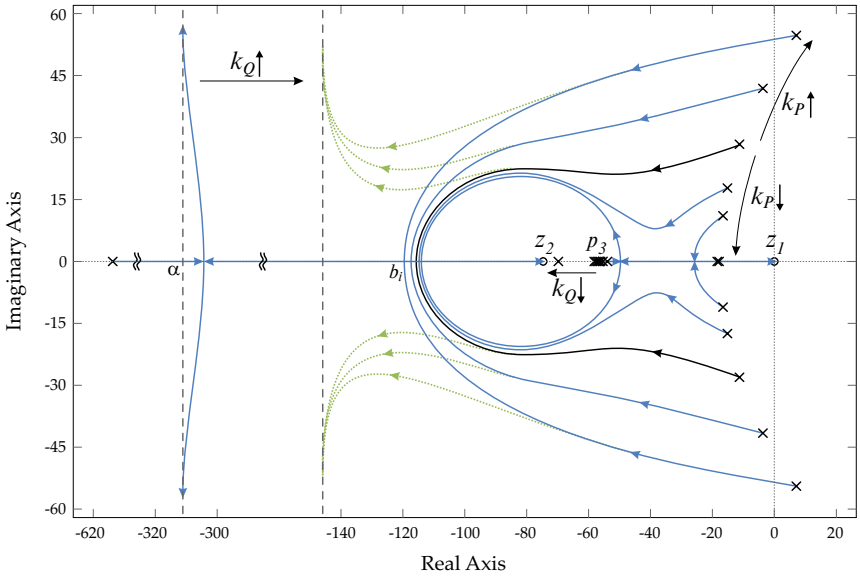

Figure 4.7: Root contour of $G_{closed}(s)$ for different values of k_P and k_Q

To better understand this figure, the root-contour shall be analyzed in parts as follows:

4.3.1 *Increase in active power droop*

For larger values of k_P, the poles of $G_{closed}(s)$ become worse damped. This is in accordance with the Nyquist plot of Fig. 3.15, which showed a decrease in phase

margin when increasing k_P. The break-in point stays almost unchanged and so does the behavior in higher frequencies. An optimal value of k_{Pd} can be found, which shifts both poles to the break-in point.

4.3.2 *Decrease in active power droop*

On the other hand, a smaller active droop further damps the poles of $G_{closed}(s)$. This could give rise to a new break-in and break-out pair between p_3 and z_2, providing for a region of lower frequencies in which critical damping could be achieved. Furthermore, a value of k_P that is small enough would turn the complex pole pair into two real poles, removing the break-in point and rendering the use of the improved droop controller unnecessary, but power output of the inverter could saturate since more active power has to be provided for the same frequency deviation.

4.3.3 *Increase in reactive power droop*

Increasing the reactive power droop moves the pole-zero pair z_2, p_3 farther apart from each other and to a higher frequency range, which makes the asymptote α become closer to them. For a value of k_Q large enough, the break-in point b_i disappears, limiting the maximal damping achievable. Note that, if no break-in point is provided, a critical damping cannot be achieved.

4.3.4 *Decrease in reactive power droop*

A small enough value of k_Q improves the stability of the inverter, allowing a smaller voltage deviation. In the root locus plot this translates into a slight shift of all open-loop poles to the left, while the locus itself stays almost unchanged. As when decreasing the active power droop, saturation of the inverter could be an issue.

From this analysis it follows that the improved droop controller can considerably damp an inverter even when the chosen static droops yield an oscillatory behavior. However, the optimal damping achievable with the improved droop controller is still limited by the choice of static droops.

4.4 TUNING THE IMPROVED DROOP CONTROLLER FOR A SINGLE INVERTER

Based on the stability analysis introduced, three methods can be derived to systematically tune the dynamic droop gain.

4.4.1 *Controller design based on root locus*

The root locus analysis provides a robust way of tuning the dynamic droop parameter k_{Pd}, choosing a value that optimizes the damping of the complex pole pair. The advantage of selecting the loop gain via root locus is that the location of the closed-loop poles can be precisely computed, yielding an optimal damping for a given configuration. However, the achievable optimal damping was shown to depend on the static droop values, which makes the search for an optimal gain hard to automate, having to account for the different possibilities discussed before, whether there is one, two, or no region on the real axis to which the complex poles can be shifted. Whenever possible, the dynamic droop gain should be chosen in a way that critical damping of the complex pole pair can be achieved.

4.4.2 *Controller design based on Bode plot*

A different approach to designing the dynamic droop is by looking at the Bode plot of $G_{closed}(s)$, which is shown in Fig. 4.8. A factor of $2\pi k_P$ is included to normalize the plot so that the amplitude is unitary at a frequency of 1 radian per second, which results from removing the gain from the integral feedback loop seen in Fig. 4.5.

The Bode plot shows a maximum gain at the frequency ω_m, which is the center frequency of the complex pole pair on G_{closed}. At this frequency, the phase crosses 0 degrees, while the magnitude varies depending on the damping of the poles which can be seen in dotted lines. The effects that different droops and the line impedance have are already accounted for in the closed-loop transfer function G_{closed}, yielding different center frequencies ω_m and damping. Since the gain is unitary at a frequency of 1 rad/s, the straight-line bode plot yields a maximum gain of ω_m. Therefore, by decreasing the loop gain ω_m times, the amplitude plot moves downwards, shifting the gain crossover frequency ω_c to ω_m, hence maximizing the phase margin ψ. Further decreasing the loop gain is unnecessary, since it would overdamp the closed-loop response.

Since this method is based on the straight-line bode plot, the actual phase margin obtained might not be minimal. However, an improvement on the phase margin

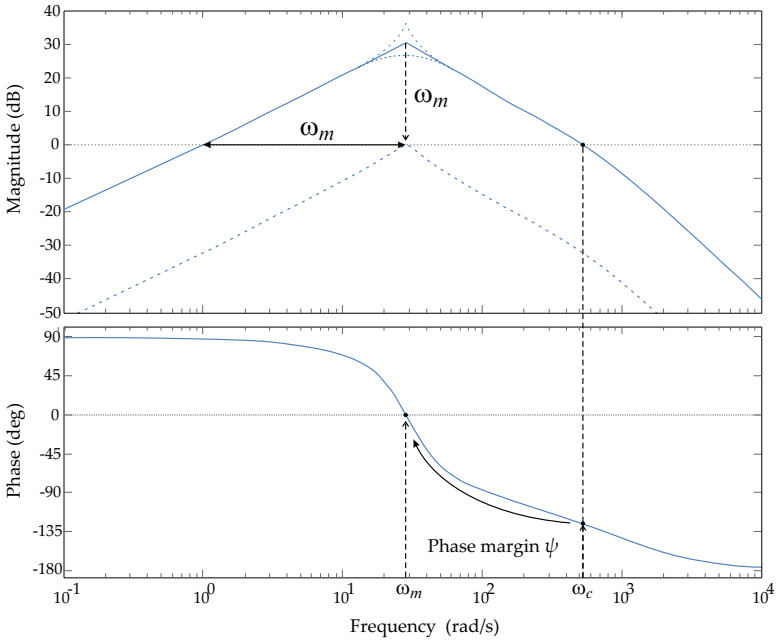

Figure 4.8: Bode plot of $2\pi k_P G_{closed}(s)$

is still achieved, enhancing the dynamics of the inverter. Although this does not provide any quantitative information a priori on the closed-loop poles of the system, it is a simple yet effective way of designing the improved droop controller which only requires computing the center frequency of the complex pole pair of $G_{closed}(s)$.

The dynamic droop gain is hence obtained from

$$k_{Pd} = \frac{2\pi k_P}{\omega_m}. \tag{4.8}$$

If G_{closed} does not present a complex pole pair, the system is already critically damped and no improved droop gain is necessary ($k_{Pd} = 0$).

4.4.3 *Controller design based on line impedance*

The third method proposed to design the dynamic droop gain k_{Pd} is less based on control engineering tools and more founded on the physical properties of power

generation. As discussed before, the role of the dynamic droop is to compensate for the delayed action of the generating source by providing a direct path between power and phase, helping to achieve a new stationary operating point after a given disturbance. With this in mind, the linearized line parameters can serve as indicators of the coupling between power and phase, and in turn be used to derive the dynamic droop gain k_{Pd}.

In particular, the line parameter $k_{P\theta}$ was calculated in Eq. (3.54) as

$$k_{P\theta} = \left.\frac{\partial P}{\partial \theta}\right|_{x_{lin}} \tag{4.9}$$

where x_{lin} represents the chosen linearization point at which the partial derivative is evaluated. This linearized gain relates to a small change in phase equivalent to the resulting change in power, which is precisely what the dynamic droop gain k_{Pd} aims to compensate. According to this, the dynamic droop gain can easily be estimated as

$$k_{Pd} = \left.\frac{\partial \theta}{\partial P}\right|_{x_{lin}} = \frac{1}{k_{P\theta}}. \tag{4.10}$$

Note that the gain designed with this method only depends on the line impedance and on the choice of linearization point. Neither the dynamics of the power inverter nor the magnitude of the droops, which were shown to impact the dynamics of the system, are considered in the choice of k_{Pd}. This renders this method extremely simple to compute, at the expense of control quality. Nevertheless, the results obtained with this approach are usually satisfactory for most real-world inverter configurations.

Although the resulting damping achieved with this method is far from optimal, the role of coupling through the power line in the design of the dynamic droop gain is worth paying attention at, which will be addressed again in Chapter 6.

4.5 SIMULATION RESULTS

In order to illustrate the results obtained with the three design methods proposed, the response of the same benchmark system as discussed in Chapter 3 is studied when implementing the improved droop controller. All the same parameters of the system are used, only adding an improved droop gain to the inverter.

Table 4.1 shows the dynamic droop gains in mrad/kW and the resulting poles of the system obtained with the three methods, as well as the poles of the inverter

without dynamic gain. The equivalent zero ω_d that results from the improved droop controller is shown as well.

Table 4.1: Resulting poles for different dynamic droop gains

Open-loop $k_{Pd} = 0$ $\omega_d = \infty$	Root locus $k_{Pd} = 2.88$ $\omega_d = 32.62$	Bode plot $k_{Pd} = 8.06$ $\omega_d = 11.66$	Impedance $k_{Pd} = 2.39$ $\omega_d = 39.24$
-629.94	-525.10	-597.04	-602.87
$-13.66 + 29.62j$	-95.30	$-36.74 + 6.67j$	$-30.45 + 17.38j$
$-13.66 - 29.62j$	-95.30	$-36.74 - 6.67j$	$-30.45 - 17.38j$
-67.98	-9.55	-54.72	-61.47

Note that the design based on root locus yields all real poles, which is achieved by increasing the gain until both complex poles are shifted to the break-in point present in the root locus. The other two methods preserve the pair of complex poles but with improved damping.

Figure 4.9 shows the power output of the inverter when a frequency drop of 100 mHz is introduced at the transformer. The response of the inverter without dynamic droop is shown in gray while the blue lines show the response of the inverter for the different dynamic droop gains shown in Table 4.1. Although such a step in frequency is unlikely to be present in the real world, this simulation helps illustrate the transient dynamics of the inverter.

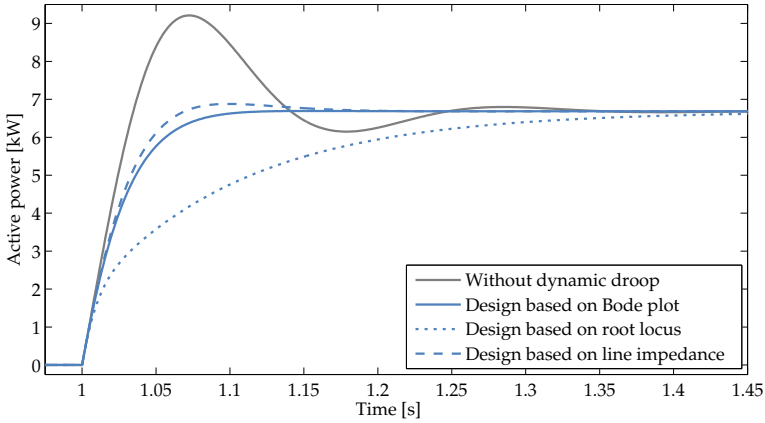

Figure 4.9: Response of the inverter to a frequency step at the transformer with different values of k_{Pd}

An interesting result can be observed by comparing the step responses of the system. The design based on line impedance damps the initial oscillatory behavior of the inverter without improved droop, yet the step response stays underdamped. The response obtained with the design based on Bode plot seems fairly damped, although a small overshoot can be noticed. On the other hand, the droop gain based on root locus, which critically damps both complex poles, yields a transient response which might seem unnecessary slow and overdamped. This is caused by the dominant effect of the slowest pole of the system, since increasing the gain needed to shift both complex poles to the real axis also shifts the slowest pole to the right, making it slower.

Under the same test scenario, it is interesting to observe as well the instantaneous frequency of the inverter, which is shown in Fig. 4.10. The dynamic droop gain subtly "pushes" the frequency towards its steady state value, resulting in a better transient response. Note that the design based on root locus yields the fastest rise time but a slower settling time, as expected from the resulting eigenvalues.

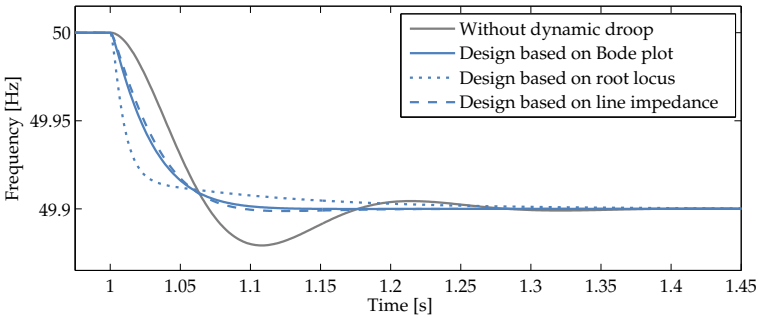

Figure 4.10: Instantaneous frequency of the inverter after a frequency step at the transformer with different values of k_{Pd}

In all cases, the transient response settles within 200-300 ms, while the right choice of dynamic droop gain turns the system faster. However, the goal of the improved droop controller is not to make the system faster but better damped, in order to avoid undesirable oscillations. Faster dynamics could actually be harmful to the stability of the system, since the model used to design the improved droop controller assumes that the internal inverter dynamics and the power line dynamics can be neglected. A given configuration resulting in an excessively fast response could therefore lead to interactions with unmodeled dynamics yielding an unstable behavior. This will be better illustrated in the next Section.

4.6 INADMISSIBLE FAST DYNAMICS

The example shown before is based on real-world inverter parameters, whereas the impedance chosen was a result of a statistical analysis made on a real-world low-voltage grid as presented in Chapter 2. A larger line impedance was shown in Chapter 3 to better damp the system, while a smaller value increases the coupling of the inverter yielding worse damped oscillatory modes and even unstable behavior.

In order to further study the damping capabilities of the improved droop controller, lets assume that the power line between the inverter and the transformer is ten times smaller, i.e. $\tilde{Z} = 0.02 + 0.04j\ \Omega$. The resulting poles obtained without dynamic droop and those resulting from each of the methods proposed are shown in Table 4.2, as well as the gain k_{Pd} and the equivalent zero ω_d related to each case.

Table 4.2: Resulting poles for different dynamic droop gains with smaller impedance

Open-loop $k_{Pd} = 0$ $\omega_d = \infty$	Root locus $k_{Pd} = 1.77$ $\omega_d = 52.92$	Bode plot $k_{Pd} = 0.95$ $\omega_d = 98.67$	Impedance $k_{Pd} = 0.31$ $\omega_d = 300.79$
-643.02	-336.56	-533.86	-611.51
$-3.80 + 98.60j$	-177.01	$-61.97 + 93.86j$	$-20.19 + 99.81j$
$-3.80 - 98.60j$	-177.01	$-61.97 - 93.86j$	$-20.19 - 99.81j$
-98.33	-58.36	-91.16	-97.07

As it was the case before, the dynamic droop controller shows its ability to damp the system. The complex poles resulting from the inverter without improved droop are damped in all cases, while the design based on root locus even accomplishes a critical damping of them, at least theoretically. However, the simulation of the full model without disregarding higher order dynamics shows that the system is actually unstable for half of the cases shown before, which can be seen in Fig. 4.11.

The response of the system without improved droop is clearly underdamped yet stable. According to the analysis presented before, increasing k_{Pd} should shift the complex poles along the root locus as shown in Fig. 4.6, resulting in a faster and better damped response. Nonetheless, the simulation shows a different behavior. The smallest of the gain values, i.e. the one obtained with the method based on the line impedance, results in faster and worse damped dynamics. This means that the complex pole pair did not shift to the left as much as expected from Table 4.2.

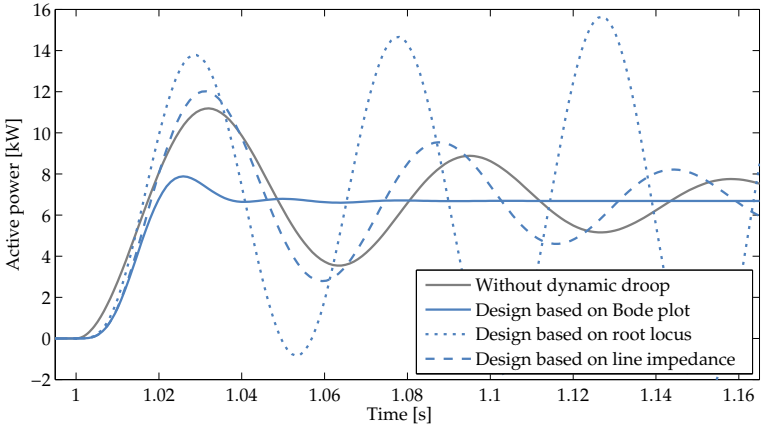

Figure 4.11: Response of the inverter to a frequency step at the transformer with different values of k_{Pd} with smaller impedance

Further increasing the gain up to the value obtained based on Bode plot results in a stable and better damped response, while the improved droop gain calculated using the root locus yields instability. This does not relate to the behavior expected from the analysis derived before and rather signals that the model used to analyze the stability of the system was wrong. This is indeed the case, since the model was derived based on the assumption that the inverter's internal dynamics and the power line dynamics could be neglected, while the resulting eigenvalues shown in Table 4.2 are rather fast, located close to the grid frequency, which suggests that the model might not be accurate. The system without improved droop has a pair of poles with a natural frequency of about 16 Hz. For the other gain values shown from left to right, the complex poles have a natural frequency of 28, 18 and 16 Hz respectively, which is about half the nominal grid frequency of 50 Hz. Furthermore, the equivalent zero of the improved droop controller lies between 8 and 48 Hz, which is overly close to the grid frequency.

Interestingly enough, the dynamic gain based on Bode plot yields a stable behavior, even though the model used is not accurate. This is the case because of the tradeoff between the need of model accuracy and the resulting control performance of this method. In the Bode plot, all system parameters are computed together resulting in a single center frequency which is used to derive the dynamic droop gain, maximizing the phase margin of the system. Unmodeled higher frequency dynamics alter the accuracy of the plot, but an optimization of the phase margin is still achieved. In the case of the root locus plot, a gain is found which shifts the poles to a precise location of the s domain, while the trajectory of the

poles is strongly affected by each and all of the parameters of the system. Hence, the sensitivity of this method to unmodeled dynamics is larger and the resulting dynamics of the real system can be in turn unstable.

An enhanced model of the system could be derived considering the faster dynamics that arise from the power line impedance as discussed in Chapter 3. In this way, new root locus plot and Bode plots could be obtained, allowing for a better design of the dynamic gain. However, there are a few reasons not to do this. In the first place, the order of the model would increase by two, which might not be prohibitive for the analysis of a single inverter, but would complicate the later extrapolation of the results obtained in this section to a system with many inverters operating in parallel. Moreover, the simple analysis in a quasi-stationary reference frame cannot reproduce correctly current harmonics and asymmetries in the three-phase system, which introduce further errors in the model in a frequency range close to 50 Hz and higher. In a real-world grid the voltages and currents are rarely perfectly sinusoidal, presenting nonlinear distortion and constant stochastic disturbances caused by load changes. This makes it difficult, if not impossible, to derive a small signal linear dynamic model which is accurate enough so as to allow for the design of a controller in a frequency range close to the nominal frequency of the grid. Still, the inverter under consideration should be able to be connected to the grid through a smaller line impedance and yet be stable. A different approach to solving these unpredicted instability issues is in this sense required.

4.7 SLOWER FILTER DYNAMICS

When studying the stability of a single inverter connected to the grid it was shown that reducing the bandwidth of the reactive power filter ω_{fQ} shifts the internal closed-loop dynamics $G_Q(s)$ to a lower frequency range, while reducing the active power filter cut-off frequency ω_{fP} has a negative effect on the relative stability of the system. Increasing the bandwidth of the filters is impracticable, since enough filtering is necessary for the estimation of active and reactive power from the measured voltages and currents.

Although a slower filter response degrades the stability of the system, the resulting dynamic droop gain can compensate this destabilizing effect. To illustrate this process, lets consider the same scenario as before in which the line impedance was reduced ten times to $\tilde{Z} = 0.02 + 0.04j\ \Omega$. In addition, the filter cut-off frequencies ω_{fp} and ω_{fQ} shall now be reduced ten times as well, resulting in

$\omega_{fP} = \omega_{fQ} = \pi$. With these values, the system without improved droop becomes slower and unstable, which can be seen in the first column of Table 4.3. In spite of this, the three methods proposed provide values for the dynamic gain that stabilize the system.

Table 4.3: Resulting poles for different dynamic droop gains with smaller impedance and slower filter constants

Open-loop $k_{Pd} = 0$ $\omega_d = \infty$	Root locus $k_{Pd} = 5.85$ $\omega_d = 16.09$	Bode plot $k_{Pd} = 3.05$ $\omega_d = 30.86$	Impedance $k_{Pd} = 0.31$ $\omega_d = 300.79$
-629.82	-564.64	-597.70	-626.68
$0.15 + 30.86j$	-32.81	$-16.23 + 27.28j$	$-1.72 + 30.89j$
$0.15 - 30.86j$	-32.81	$-16.23 - 27.28j$	$-1.72 - 30.89j$
-10.27	-10.13	-10.22	-10.26

Unlike before, the resulting center frequencies of the oscillatory modes are much lower than the nominal grid frequency. The open loop system oscillates with a frequency of about 4.9 Hz, while the complex pole pairs resulting from the three methods yield natural frequencies of 5.2, 5.0, and 4.9 Hz, from left to right.

The response of the system to a frequency step at the transformer is simulated as before, which can be seen in Fig. 4.12. Given that the natural frequencies are now much slower than the grid frequency, the simulation reproduces the dynamics from Table 4.3 as expected. The marginal stability resulting from the dynamic gain derived with the method based on line impedance can as well be noticed.

The procedure just shown constitutes a method to stabilize a given system which otherwise would result in fast and unstable behavior. The first step consists in making the system slower and worse damped through the choice of a lower cutoff frequency for the power filters. Subsequently, the dynamic droop gain is designed to damp the system. As a result, a slower and better damped response can be achieved.

The example scenario shown was obtained considering a smaller line impedance. However, the same approach is valid when an unfavorable choice of droop parameters yields unacceptably fast dynamics.

As a consequence of turning the inverter's response slower, a larger dynamic droop is necessary in order to push the phase forward and compensate for the delayed action of the filters. A disadvantage of larger dynamic droop gains could be argued when it comes to noise sensitivity. However, the equivalent zero on the

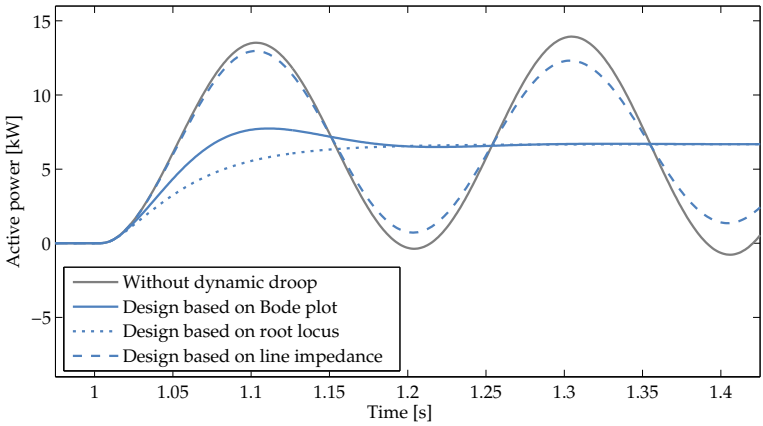

Figure 4.12: Response of the inverter to a frequency step at the transformer with different values of k_{Pd}

PI controller lies in the range of a few Hz, which should not jeopardize the stability of the system due to its sensitivity to noise and the faster nonlinear processes present in a power grid.

4.8 COMPARISON OF THE METHODS PROPOSED

The three methods proposed in this chapter were shown capable of deriving a dynamic droop gain that stabilizes a given inverter connected to the grid within certain limits. Table 4.4 resumes the characteristics of each method evaluated according to different criteria. A plus sign means good, a circle average, and a minus sign poor performance.

The method based on root locus was the only capable of achieving critical damping of the complex poles, considering explicitly all parameters of the system when computing the transfer function $G_{closed}(s)$. This makes it powerful but hard to compute, which in turns makes it prone to error caused by unmodeled dynamics.

The method based on Bode plot only depends on the center frequency of the complex pole pair. All other parameters are accounted for implicitly in this value. Although the resulting poles are not critically damped, this method is the best compromise between closed-loop dynamics and robustness against model uncertainties.

Table 4.4: Comparison of the different methods proposed to derive the dynamic droop gain

	RL	Bode	$\tilde{Z}$
Easiness to compute	-	○	+
Sensitivity to unmodeled dynamics	-	○	-
Damping of the resulting closed-loop poles	+	○	-
Accounts for no need of k_{Pd}	+	+	-
Accounts for the values of k_P and k_Q	+	○	-
Accounts for the value of the line impedance	+	○	+
Accounts for the values of ω_{fP} and ω_{fQ}	+	+	-

The method based on line impedance was proven to be the simplest to compute, yet the resulting performance is far from being optimal. The dynamic droop gain is derived only based on the impedance parameters and linearization point. Therefore, the sensitivity of this method to changes in the rest of the system parameters is poor. However, the role of coupling through the power line in the design of the dynamic droop gain is worth paying attention at, especially when several inverters are connected to each other through impedances of different values. For such a scenario, some extension of these methods or even a combination between them shall be studied. This will be addressed in Chapter 6.

5

MODEL OF A LOW-VOLTAGE GRID WITH DISTRIBUTED GENERATION

The dynamics studied so far has been derived considering a single inverter connected to an ideal stiff grid. However, in a real-world grid the inverters are not isolated but rather interconnected through power lines, which couple their dynamics and give rise to more complex behavior. In addition, the meshed nature of the grid can render the concept of a single PCC inappropriate. In this sense, a proper model for a group of inverters in a distributed grid is needed, which has to reproduce the complex phenomena that arises from their coupling.

5.1 SYNCHRONIZATION

When several simple systems are put together into a larger more complex structure, surprising behavior can arise. When the behavior of such a system is not a property of any single portion of that system but rather a property that emerges due to interactions among them, it is called *emergent behavior*. The existence of emergent properties is one of the most distinguishing features of complex systems. Particularly interesting is the phenomenon of synchronization, which is the adjustment of the rhythms of oscillating objects due to their weak interaction [61]. Although the terms *rhythm* and *oscillating objects* are vaguely defined, the synchronization of several complex systems can be studied by deriving mathematical models accordingly.

The first documented scientific observation of synchronization phenomena dates back to 1665, when the physicist Christiaan Huygens noted that two pendulum clocks hanging from the same wooden beam will swing coherently. However, the basic idea behind emergent behavior has been around since the time of Aristotle, who first postulated that the whole is greater than the sum of the parts. In this sense, the complexity of the resulting synchronization is not in the individual objects, but rather in the way in which they interconnect.

Nowadays, the emergence of synchronization is a fascinating topic in various scientific disciplines that range from engineering, chemistry, and biology, to neuroscience and sociology. There are hundreds of examples of this, ranging from synchronous pendulums as those from Huygens to more abstract behavior such as birds flying in flocks, fish schools, voting patterns and even trends in the fashion industry. The synchronization of several rotating generators in a power system is no exception to this phenomenon.

5.1.1 *The Kuramoto model*

The simplest and most used model for synchronization phenomena available today is the so called Kuramoto Model, propsed in 1975 by Yoshiki Kuramoto [62]. The model considers a set of N coupled oscillators, each of which is governed by the equation

$$\dot{\theta}_i = \omega_i + \sum_{j=1}^{N} \mu_{ij} \sin(\theta_j - \theta_i), \qquad i = 1, ..., N. \tag{5.1}$$

Each oscillator has an intrinsic random natural frequency ω_i, distributed with a given probability density, and is coupled to all other oscillators through the gains μ_{ij}. If one isolates the oscillators ($\mu_{ij} = 0 \forall i, j$), each one will oscillate with its distinct frequency ω_i. However, all oscillators will synchronize spontaneously to a collective frequency when sufficient coupling is provided. Despite its apparent simplicity, this model gives rise to highly complex dynamic behavior, and it can be further modified to include damping and other sorts of coupling between nodes [63].

A simple graphical interpretation of this phenomenon can be seen in Fig. 5.1, which shows three points connected to each other through springs while rotating in a circle. Note that this is a simplified two-dimensional representation and no collisions are possible. If the springs were not provided, each point will continue to rotate with its natural frequency ω_i. When the springs are added to the system, each oscillator becomes coupled with the other two. In this way, any difference between their frequencies will compress or expand a spring, generating a compensating force that accelerates or decelerates the oscillators. As a result of the coupling, a synchronization of the oscillators arises and the three points rotate synchronously. Should a disturbance on the system modify this phase difference, the synchronization process starts over again and a new equilibrium state is achieved.

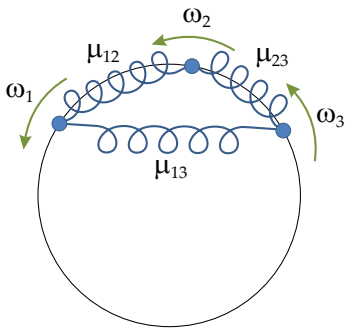

Figure 5.1: Mechanical analog of three coupled oscillators.

This model has found applications in the power generation area, since Eq. (5.1) is identical to the simplified model of a synchronous generator in a HV power grid, whereas the coupling μ_{ij} relates to the inductance of the power line [4].

Surprisingly, this fully nonlinear dynamic model can be solved exactly in the limit of infinite number N of oscillators, assessing the absolute stability of the system for a given coupling between oscillators. The existence of such a solution has fascinated researchers for decades and has yielded sophisticated methods to study the nonlinear dynamics of such systems. Particularly worth to mention is the capacity to asses the transient stability of a power system and to estimate its region of attraction, that is the stability of a new equilibrium state arising after a large change in the network parameters or topology, as it is usual after a fault event.

However, there are some disadvantages and limitations related to this. For instance, the assumption that a closed-form solution with $N \to \infty$ is related to a real power system can be accepted in a large-scale interconnected system such as the European power grid, but to perform a similar analysis in a LV grid with only 10 or 20 generating units might not be logical. Moreover, the authors in [64] postulate that a MG with several droop-controlled inverters is mathematically equivalent to a group of coupled oscillators. Nonetheless, this is only the case when considering a single common load in the grid and perfectly inductive power lines, which is certainly not the case in a real LV grid.

Some limitations on the model can be bypassed by modifing Eq. (5.1) accordingly. For instance, the non-uniform Kuramoto model introduced in [65] incorporates the resistive nature of the power lines in a LV grid to the model but further neglects the dynamics of voltage control. As a matter of fact, coupled and higher order dynamics are hard to integrate into the model, and a closed-form solution

to the synchronization problem might not be feasible. Compared with the simple mechanical analog of Fig. 5.1, including the voltage dynamics into the model would mean that the points do not simply rotate in a common circle, but also the radius of each circle changes with time.

Last but not least, it is essential to note that a nonlinear analysis in a LV grid only makes sense in the context of transient stability and post-fault events, whereas the small-signal dynamics of a system during normal functioning has to be stable as well. In this case, the selection of the inverters' control parameters is a small-signal stability problem for which a linearization at the working point is sufficient.

For these purposes, the following will focus on deriving a complete model for the dynamics of a group of droop-controlled inverters in a LV grid considering their coupling through the power flow in the grid and the linear dynamics of each inverter. This model will later be linearized and used for controller design.

5.2 NONLINEAR MIMO POWER FLOW MODEL

In order to calculate the power flow through a network, it is necessary to derive the voltages and currents at each node, which are related to each other through the admittance matrix $\tilde{\boldsymbol{Y}}_{\boldsymbol{NetEq}}$ (see Chapter 2), such that

$$\tilde{\boldsymbol{I}} = \tilde{\boldsymbol{Y}}_{\boldsymbol{NetEq}} \tilde{\boldsymbol{U}}_{\boldsymbol{E}}. \tag{5.2}$$

Note that $\tilde{\boldsymbol{I}}$ and $\tilde{\boldsymbol{U}}_{\boldsymbol{E}}$ are vectors that contain the voltages and currents at each of the n nodes of the power grid to which energy sources are connected.

The network model is completed as shown in Fig. 5.2, recalling the Thévenin equivalent of the power inverter, which includes a non-zero output impedance.

Adding the output impedance of the inverters in series yields the equivalent admittance matrix $\tilde{\boldsymbol{Y}}_{\boldsymbol{Eq}}$, which relates the inverter currents $\tilde{I}_i$ to their voltages $\tilde{U}_i$. This admittance can easily be computed from

$$\tilde{\boldsymbol{Y}}_{\boldsymbol{Eq}}{}^{-1} = \tilde{\boldsymbol{Y}}_{\boldsymbol{NetEq}}{}^{-1} + \tilde{\boldsymbol{Z}}_{\boldsymbol{Out}}, \tag{5.3}$$

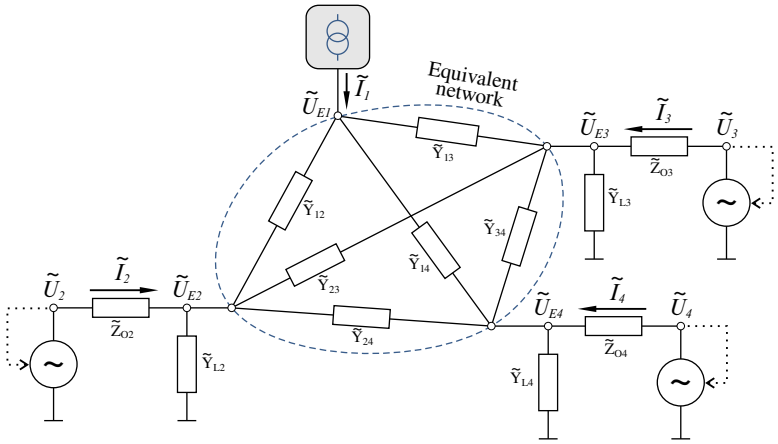

Figure 5.2: Example of an equivalent LV grid with three inverters and the admittances between nodes.

with the diagonal output impedance matrix

$$\tilde{\boldsymbol{Z}}_{\boldsymbol{Out}} = \begin{pmatrix} 0 & 0 & 0 & 0 \\ 0 & \tilde{Z}_{O2} & 0 & 0 \\ 0 & 0 & \tilde{Z}_{O3} & 0 \\ 0 & 0 & 0 & \tilde{Z}_{O4} \end{pmatrix}. \tag{5.4}$$

The vector of apparent powers $\tilde{\boldsymbol{S}}$ can then be computed as the element-wise product of the voltage vector with the complex conjugate of the current, such that:

$$\tilde{\boldsymbol{S}} = \tilde{\boldsymbol{U}}.\tilde{\boldsymbol{I}}^* \tag{5.5}$$

Equations (5.2) and (5.5) together with the phasor equation $\tilde{\boldsymbol{U}} = \boldsymbol{U}e^{j\boldsymbol{\theta}}$ add up to the nonlinear MIMO system shown in Fig. 5.3, which describes the power flow in the grid, in a first instance without dynamic phasors. $2n$ inputs are grouped in the vectors $\boldsymbol{U}$ and $\boldsymbol{\theta}$, and $2n$ outputs are grouped in $\boldsymbol{P}$ and $\boldsymbol{Q}$. All signals on this diagram are vectors as well.

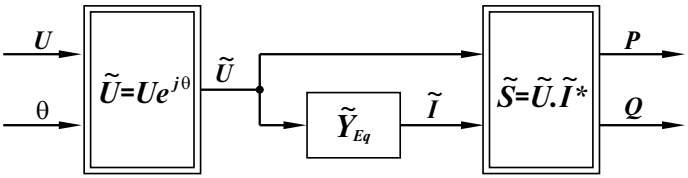

Figure 5.3: Nonlinear power flow model

5.3 LINEAR MIMO INVERTER MODEL

For the case of several inverters, the model presented in Chapter 3 can easily be extended changing all scalars to vectors. In this case, the voltages U_i and phases θ_i at a given node i of a total of n nodes are grouped together in the vectors

$$\boldsymbol{U} = \begin{pmatrix} U_1 \\ U_2 \\ \dots \\ U_n \end{pmatrix}, \qquad \boldsymbol{\theta} = \begin{pmatrix} \theta_1 \\ \theta_2 \\ \dots \\ \theta_n \end{pmatrix}. \tag{5.6}$$

The same is done with every other variable in Fig. 3.3, while $\boldsymbol{K_P}$ and $\boldsymbol{K_Q}$ are $n \times n$ diagonal matrices with the droop coefficients $k_{P_1}, k_{P_2}, ...k_{P_n}$ and $k_{Q_1}, k_{Q_2}, ...k_{Q_n}$. This method describes a linear MIMO system with $2n$ inputs grouped in the vectors $\boldsymbol{P}$ and $\boldsymbol{Q}$, $2n$ outputs grouped in $\boldsymbol{U}$ and $\boldsymbol{\theta}$, and $3n$ state variables in the vectors $\boldsymbol{\theta}$, $\hat{\boldsymbol{P}}$, and $\hat{\boldsymbol{Q}}$.

The block diagram of Fig. 3.3 stays unchanged, although it has to be noted now that all signals on the diagram turn into vectors. This block diagram is repeated with vector notation in Fig. 5.4 for clarity

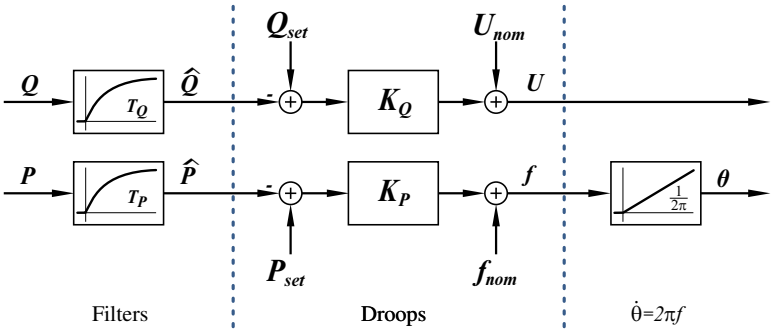

Figure 5.4: Simplified block diagram of a set of droop-controlled inverters

5.4 JOINT MODEL

Linking the inverter and grid models together delivers the closed-loop nonlinear system shown in Fig. 5.5, which describes the power flow between inverters coupled through a power grid. The dynamic phasor model is shown with a dashed contour, since its implementation is optional.

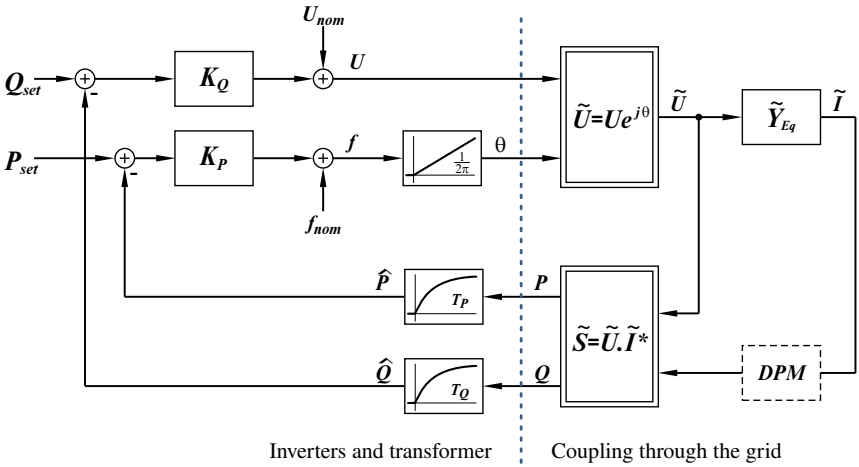

Figure 5.5: Proposed nonlinear model for multiple interconnected inverters

This model can be used to simulate the dynamics of one or more inverters connected to a power grid in a simple yet powerful way. Its realization in MATLAB/Simulink is straightforward, following the block diagram of Fig. 5.5. The scalability of this approach is also a point worth to mention, since all signals on this diagram are actually vectors whose elements describe different nodes of the grid.

5.5 GRID-CONNECTED AND AUTONOMOUS OPERATION

When studying the stability of parallel-connected power inverters in LV grids, it is common to find different modeling approaches depending on the case that is being considered. For a grid-connected MG, the transformer is generally represented by an infinite bus with a given amplitude and frequency which cannot be influenced by the MG. To the contrary, the transformer node is ignored in autonomous operation. Both approaches can be obtained modifying the simple model proposed. Moreover, a third option could also be considered.

The case of a stiff grid can be easily achieved by setting the droop parameters of the corresponding node t to zero. In this case, the state variables $\hat{P}_t$ and $\hat{Q}_t$ vanish, while the nominal values U_{n_t} and f_{n_t} are left as inputs, reducing the order of the system. This provides a simple way to simulate disturbances such as voltage drops or frequency swings at the transformer.

Ignoring the transformer can as well be done, simply removing the equations for the given node. This makes it possible to study the interaction between several inverters in autonomous operation. Considering more than one transformer is also possible, although this is rarely the case in LV grids.

The third option is to establish equivalent droops and dynamics at the transformer node, replacing the corresponding droop parameters and time constants with those of the equivalent MV grid. This lays down a simulation framework for future scenarios, where the amount of load-following energy generated in a decentralized manner could surpass the one available on the MV grid. The impact of the dynamics between medium and low-voltage grids could hence be studied in this way.

5.6 SMALL-SIGNAL DYNAMICS OF MULTIPLE INVERTERS

The nonlinear model derived accounts for the local dynamics of each inverter and the emergent behavior that arises from their coupling through the grid. The dynamics of the power flow between n nodes can be easily simulated with this complex-valued nonlinear model. However, this approach does not provide any information a priori about the stability of the system. With this purpose, the system can be linearized at an operating point, allowing for an eigenvalue analysis of the complete system.

The linear MIMO model for a set of droop-controlled inverters shown in Fig. 5.4 can be directly described in state space form as:

$$\dot{\boldsymbol{x}}_{\boldsymbol{Inv}} = \boldsymbol{A}_{\boldsymbol{Inv}}\boldsymbol{x}_{\boldsymbol{Inv}} + \boldsymbol{B}_{\boldsymbol{Inv}}\boldsymbol{u}_{\boldsymbol{Inv}}, \quad \boldsymbol{y}_{\boldsymbol{Inv}} = \boldsymbol{C}_{\boldsymbol{Inv}}\boldsymbol{x}_{\boldsymbol{Inv}} \tag{5.7}$$

with the matrices:

$$\boldsymbol{A}_{\boldsymbol{Inv}} = \begin{pmatrix} \boldsymbol{0} & -2\pi\boldsymbol{K}_{\boldsymbol{P}} & \boldsymbol{0} \\ \boldsymbol{0} & -\boldsymbol{\omega}_{\boldsymbol{f_P}} & \boldsymbol{0} \\ \boldsymbol{0} & \boldsymbol{0} & -\boldsymbol{\omega}_{\boldsymbol{f_Q}} \end{pmatrix} \tag{5.8}$$

$$\boldsymbol{B_{Inv}} = \begin{pmatrix} \mathbf{0} & \mathbf{0} \\ \boldsymbol{\omega_{f_P}} & \mathbf{0} \\ \mathbf{0} & \boldsymbol{\omega_{f_Q}} \end{pmatrix} \tag{5.9}$$

$$\boldsymbol{C_{Inv}} = \begin{pmatrix} \mathbf{1} & \mathbf{0} & \mathbf{0} \\ \mathbf{0} & \mathbf{0} & -\boldsymbol{K_Q} \end{pmatrix} \tag{5.10}$$

considering the states $\boldsymbol{x_{Inv}}$, inputs $\boldsymbol{u_{Inv}}$, and outputs $\boldsymbol{y_{Inv}}$:

$$\boldsymbol{x_{Inv}} = \begin{pmatrix} \boldsymbol{\theta} \\ \hat{\boldsymbol{P}} \\ \hat{\boldsymbol{Q}} \end{pmatrix}, \quad \boldsymbol{u_{Inv}} = \begin{pmatrix} \boldsymbol{P} \\ \boldsymbol{Q} \end{pmatrix}, \quad \boldsymbol{y_{Inv}} = \begin{pmatrix} \boldsymbol{\theta} \\ \boldsymbol{U} \end{pmatrix}, \tag{5.11}$$

where $\mathbf{1}$ and $\mathbf{0}$ indicate identity and zero matrices respectively.

Recall that $\boldsymbol{\theta}$, $\hat{\boldsymbol{P}}$, $\hat{\boldsymbol{Q}}$, $\boldsymbol{P}$, $\boldsymbol{Q}$, and $\boldsymbol{U}$ are vectors with n elements, while the matrices $\boldsymbol{A_{Inv}}$, $\boldsymbol{B_{Inv}}$ and $\boldsymbol{C_{Inv}}$ result of size $3n \times 3n$, $3n \times 2n$, and $2n \times 3n$ respectively.

The coupling through the grid can be considered as a nonlinear gain, which must be linearized at the complex operating point $\tilde{\boldsymbol{U}}_{\mathbf{0}} = \boldsymbol{U_0} e^{j\boldsymbol{\theta_0}} = \boldsymbol{U_{0r}} + j\boldsymbol{U_{0i}}$.

A matrix representation of the linearized power flow in the grid is possible recalling equations (3.23) through (3.28), which yield

$$\begin{pmatrix} \boldsymbol{\Delta P} \\ \boldsymbol{\Delta Q} \end{pmatrix} = \underbrace{\begin{pmatrix} \boldsymbol{U_{0r}}^d & \boldsymbol{U_{0i}}^d \\ \boldsymbol{U_{0i}}^d & -\boldsymbol{U_{0r}}^d \end{pmatrix}}_{\boldsymbol{U_{0r,i}}} \begin{pmatrix} \boldsymbol{\Delta I_r} \\ \boldsymbol{\Delta I_i} \end{pmatrix} + \underbrace{\begin{pmatrix} \boldsymbol{I_{0r}}^d & \boldsymbol{I_{0i}}^d \\ -\boldsymbol{I_{0i}}^d & \boldsymbol{I_{0r}}^d \end{pmatrix}}_{\boldsymbol{I_{0r,i}}} \begin{pmatrix} \boldsymbol{\Delta U_r} \\ \boldsymbol{\Delta U_i} \end{pmatrix} \tag{5.12}$$

The symbol ^{d} indicates an extension of the vector to a diagonal matrix whose non-zero elements are those of the vector, in the same order. This is a simple mathematical subtlety that allows for a compact representation of the linearized equations (3.23) through (3.28) in matrix form.

The currents and voltages are related through the equivalent impedance matrix $\tilde{\boldsymbol{Y}}_{\boldsymbol{eq}}$, which can be separated into a conductance matrix and a susceptance matrix, resulting in

$$\boldsymbol{G_{Eq}} = Re\{\tilde{\boldsymbol{Y}}_{\boldsymbol{Eq}}\}, \quad \boldsymbol{B_{Eq}} = Im\{\tilde{\boldsymbol{Y}}_{\boldsymbol{Eq}}\}, \tag{5.13}$$

$$\begin{pmatrix} \boldsymbol{\Delta I_r} \\ \boldsymbol{\Delta I_i} \end{pmatrix} = \underbrace{\begin{pmatrix} \boldsymbol{G_{Eq}} & \boldsymbol{-B_{Eq}} \\ \boldsymbol{B_{Eq}} & \boldsymbol{G_{Eq}} \end{pmatrix}}_{\boldsymbol{Y_{r,i}}} \begin{pmatrix} \boldsymbol{\Delta U_r} \\ \boldsymbol{\Delta U_i} \end{pmatrix} \tag{5.14}$$

Last but not least, the phasor equation can be separated into real and imaginary parts, and linearized as a function of its amplitude and phase, as shown in Eq. (3.31), which yields

$$\begin{pmatrix} \boldsymbol{\Delta U_r} \\ \boldsymbol{\Delta U_i} \end{pmatrix} = \underbrace{\begin{pmatrix} -\boldsymbol{U_0}^d \circ \sin(\boldsymbol{\theta_0})^d & \cos(\boldsymbol{\theta_0})^d \\ \boldsymbol{U_0}^d \circ \cos(\boldsymbol{\theta_0})^d & \sin(\boldsymbol{\theta_0})^d \end{pmatrix}}_{\boldsymbol{T_0}} \begin{pmatrix} \boldsymbol{\Delta \theta} \\ \boldsymbol{\Delta U} \end{pmatrix} \tag{5.15}$$

Replacing equations (5.14) and (5.15) into Eq. (5.12) yields the linearized power flow equation

$$\begin{pmatrix} \boldsymbol{\Delta P} \\ \boldsymbol{\Delta Q} \end{pmatrix} = \boldsymbol{N} \begin{pmatrix} \boldsymbol{\Delta \theta} \\ \boldsymbol{\Delta U} \end{pmatrix}, \tag{5.16}$$

with

$$\boldsymbol{N} = \left(\boldsymbol{U_{0r,i}} \boldsymbol{Y_{r,i}} + \boldsymbol{I_{0r,i}}\right) \boldsymbol{T_0}. \tag{5.17}$$

The matrix $\boldsymbol{N}$ is of size $2n \times 2n$ and represents the linearized coupling of the inverters due to the power flow through the grid.

Combining the inverter model of Eq. (5.7) with the linearized coupling matrix on Eq. (5.16) gives rise to the closed-loop system matrix $\boldsymbol{A_{sys}}$, whose eigenvalues characterize the small signal dynamics - and hence the stability - of the power flow between inverters:

$$\boldsymbol{A_{sys}} = \boldsymbol{A_{Inv}} + \boldsymbol{B_{Inv}}\, \boldsymbol{N}\, \boldsymbol{C_{Inv}}. \tag{5.18}$$

Considering the frequency $\boldsymbol{\Delta f_{nom}}$ and voltage amplitude $\boldsymbol{\Delta U_{nom}}$ at each node as inputs and the resulting power flow $\boldsymbol{\Delta P}$, $\boldsymbol{\Delta Q}$ as outputs, the state-space representation of the linearized system is completed by the matrices:

$$\boldsymbol{B_{sys}} = \begin{pmatrix} & 2\pi\mathbf{1} & \mathbf{0} \\ \begin{pmatrix} \boldsymbol{\omega_{fP}} & \mathbf{0} \\ \mathbf{0} & \boldsymbol{\omega_{fQ}} \end{pmatrix} N & & \begin{pmatrix} \mathbf{0} & \mathbf{0} \\ \mathbf{0} & \mathbf{1} \end{pmatrix} \end{pmatrix} \tag{5.19}$$

$$\boldsymbol{C_{sys}} = \boldsymbol{N} \begin{pmatrix} \mathbf{1} & \mathbf{0} & \mathbf{0} \\ \mathbf{0} & \mathbf{0} & \mathbf{0} \end{pmatrix} \tag{5.20}$$

$$\boldsymbol{D_{sys}} = \boldsymbol{N} \begin{pmatrix} \mathbf{0} & \mathbf{0} \\ \mathbf{0} & \mathbf{1} \end{pmatrix}. \tag{5.21}$$

The transfer functions from each input to each output can be obtained by evaluating the transfer matrix

$$\boldsymbol{G_{sys}} = \boldsymbol{C_{sys}}(s\mathbf{1} - \boldsymbol{A_{sys}})^{-1}\boldsymbol{B_{sys}} + \boldsymbol{D_{sys}}. \tag{5.22}$$

For a system with n inverters in autonomous operation, the matrix $\boldsymbol{A_{sys}}$ is of size $3n \times 3n$. The rank of this matrix is however $3n-1$. This is a small drawback of the proposed modeling approach, which implies describing the phase locally at every inverter, whereas the actual power flow is not governed by the absolute phases of the voltage phasor at the nodes but by the phase differences between them. Most authors [7, 16, 18, 40, 57, 58, 66, 67] consider this physical property when modeling power interactions through the grid from start on, selecting one node as base and referring all other inverter phases to it. In the grid-connected case, the transformer is selected as a reference. As a result, the modeling technique is restricted to a given configuration and has to be modified, however slightly, when adding or removing inverters to the system, or when changing the configuration of the grid. The proposed modular model does not depend on a reference, hence simplifying the modeling for any chosen configuration. Ultimately, the reduced rank of the system matrix only produces an extra pole at zero, which can be easily disregarded when studying the eigenvalues of the system.

For the grid-connected case, in which $n - 1$ inverters are connected to an ideal transformer through a grid, the rank of $\boldsymbol{A_{sys}}$ further reduces in two to $3(n - 1)$, since the two state variables related to the estimation of active and reactive power at the transformer vanish when considering it as an ideal voltage source with no dynamics. In this case, the eigenvalue analysis yields two extra poles at the origin, which must as well be disregarded. With this in mind, the small-signal stability of a given LV grid with DG can be studied computing the eigenvalues of the matrix $\boldsymbol{A_{sys}}$, disregarding additional poles at the origin when proper.

5.7 VERIFICATION OF THE MODEL

A validation scenario for the proposed model can be seen in Fig. 5.6, which consists in three inverters functioning in autonomous operation. The same configuration and parameters as in [37] are chosen in order to compare results. Two loads of value $\tilde{Z}_{L1} = 25\ \Omega$ and $\tilde{Z}_{L3} = 20\ \Omega$ are connected at nodes 1 and 3,

representing 12.9 kW of load. The inverters are configured to provide 3.8, 4.3, and 4.8 kW of active power and 0, -200 and 200 var of reactive power at steady state.

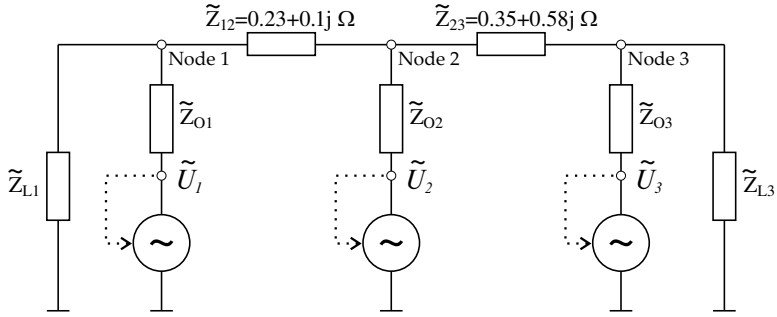

Figure 5.6: Three inverters in autonomous operation

The authors in [37] have shown experimental results from a MG with this configuration after being excited with a controlled current source in parallel to the load at node 1, providing a step change of 3.8 kW. In the proposed model, this translates to an equivalent decrease of the load impedance $\tilde{Z}_{L1}$, which is changed to $\tilde{Z}_{L1} = 15\ \Omega$. This yields the simulation results shown in Fig. 5.7. The complete model of the system as shown in [37] was implemented in MATLAB/Simulink and the solid lines show the resulting behavior obtained with this model. On the other hand, the dashed lines show the behavior of the proposed model. A verification against experimental results can be done by comparing to the measurements shown in [37], Fig. 14 and 15.

Some small deviation from nominal values are observed in the simulation, which are due to the fact that the proposed model neglects power loses in the inverter, whereas the reference model includes small resistors that introduce power loses in the output filter of the inverter.

In order to examine the low frequency modes under a severe step in RL load, the authors in [37] repeated the experiment exciting the unloaded system with a load step of 16.8 kW, 12 kvar at bus 1. To recreate this disturbance, the equivalent admittance parameters $\tilde{Y}_{L1}$ and $\tilde{Y}_{L3}$ are initially set to zero, while the load step is achieved changing $\tilde{Y}_{L1}$ to $116.3 - 83.1j\ mS$. Simulation results for the proposed model are shown in Fig. 5.8. The solid lines represent the full model, while the dashed line shows the behavior of the proposed model. Note the small 50 Hz ripple present in the full model, which is due to resonance in the inductive load. Please refer to [37], Fig. 16 and 17, for a comparison with experimental results.

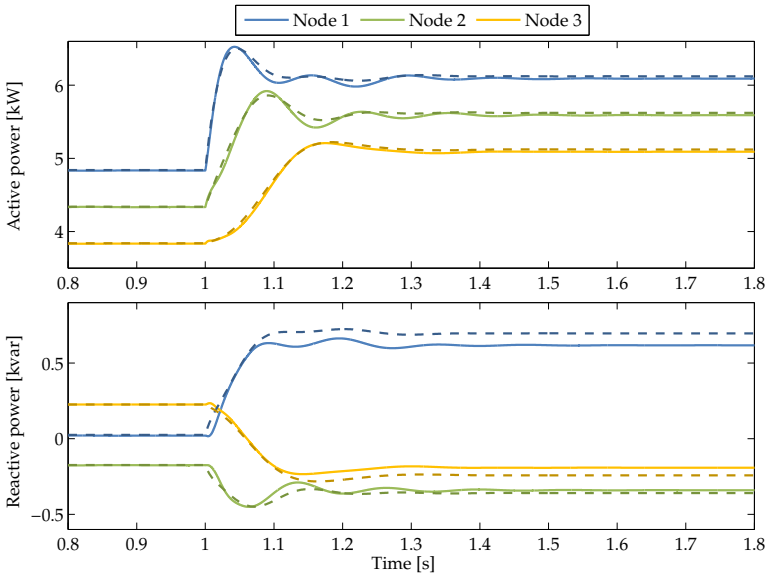

Figure 5.7: Active and reactive power delivered by the inverters after a 3.8 kW load step at node 1

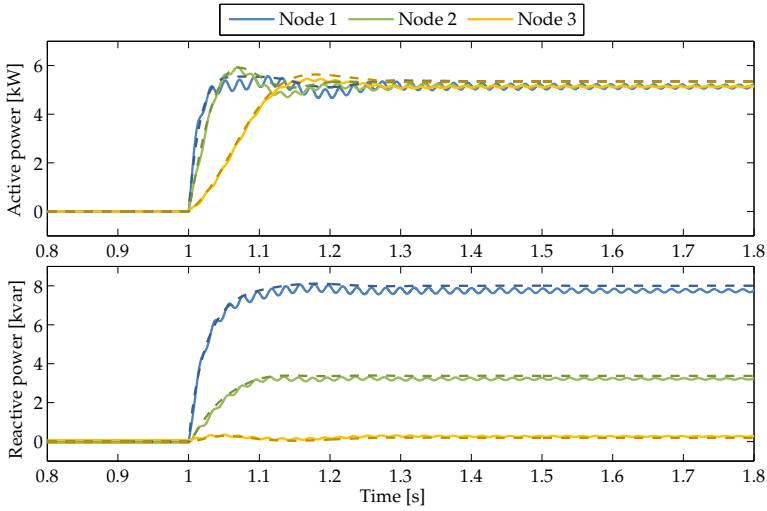

Figure 5.8: Active and reactive power delivered by the inverters after a 16.8 kW + 12 kvar load step at node 1

The complete linearized state space model for this three-inverter autonomous MG yields 43 state variables, most of which are related to faster modes, while considering only the slower dynamics of the power controller reduces the order of the system to only 9. The active and reactive power response simulated in Fig. 5.7 and 5.8 are analogous to those obtained through the detailed modeling of the system and experimentally through measurements in a real test system in [37]. Some minor differences arise, proper of neglecting high order dynamics. Note as well that the curves do not match perfectly mostly because of the initial conditions following the disturbance, whereas the eigenfrequency and damping on all curves are very similar. Thus, it is worth to highlight that the low frequency modes present in a typical LV grid are still correctly reproduced with the proposed approach, even though the faster dynamics are neglected.

5.8 EIGENVALUES AND SENSITIVITY ANALYSIS

The model just studied is composed of three inverters in autonomous operation, which results in an $\boldsymbol{A_{sys}}$ matrix with rank eight. Replacing with the parameters used for the simulation, the eight eigenvalues λ_i of Table 5.1 are obtained.

Table 5.1: Eigenvalues of the simulated system

λ_i	Damping	Freq. (rad/s)
$-11.76 + 44.35j$	0.256	45.89
$-11.76 - 44.35j$	0.256	45.89
$-14.31 + 21.49j$	0.554	25.82
$-14.31 - 21.49j$	0.554	25.82
-31.42	1	31.42
-31.42	1	31.42
-55.83	1	55.83
-97.50	1	97.50

These eigenvalues result of the interaction of all three inverters with each other through the inductances $\tilde{Z}_{12}$ and $\tilde{Z}_{23}$. A direct relationship between each pole and a given inverter is not perceivable, since the eigenvalues result from the dynamics of the system as a whole and not from an inverter in particular. However, it is possible to define a sensitivity of each eigenvalue to the variation of the droop parameter k_{P_j} of each inverter j, as described by Eq. (5.23).

$$S_j = \left| \frac{1}{\lambda_i} \frac{\partial \lambda_i}{\partial k_{P_j}} \right| \tag{5.23}$$

The resulting sensitivities for the system under simulation have been computed numerically and are shown in Table 5.2.

Table 5.2: Eigenvalues of the simulated system

λ_i	S_1	S_2	S_3
$-11.76 + 44.35j$	0.2048	0.2907	0.0090
$-11.76 - 44.35j$	0.2048	0.2907	0.0090
$-14.31 + 21.49j$	0.1417	0.0536	0.3875
$-14.31 - 21.49j$	0.1417	0.0536	0.3875
-31.42	0.0001	0.0000	0.0002
-31.42	0.0002	0.0001	0.0000
-55.83	0.0252	0.0275	0.0001
-97.50	0.0132	0.0002	0.0180

By computing the sensitivity of the poles, it is possible to understand the relationship between the modes of the system and each individual inverter. As a matter of fact, it turns out that not every inverter has the same impact on the eigenvalues of the system. For instance, the first and worst damped complex pole pair is mostly related to inverter number two, whereas the second complex pole pair can be better influenced through the third inverter.

This sensitivity information could be used to tune the system in a way that maximum damping is achieved. Indeed, similar sensitivity measures are normally used in optimization problems, which interpret a vector of sensitivities $\boldsymbol{S} = (S_1, S_2, ..., S_n)$ as the direction of steepest descent in which a minimum can be found [9]. However, this requires modifying the static droop gains, which might not be possible in a complex system that has to cope with other constraints. Implementing improved droop controllers on each inverter can in fact optimize the dynamic response of the system, which will be addressed in Chapter 6.

6

IMPROVED DROOP CONTROLLER FOR MULTIPLE INVERTERS

Having dealt with the optimal selection of the dynamic droop gain for a single inverter in Chapter 4, it is now necessary to extend this process for a system with several inverters operating in parallel.

In many works [16, 18, 20, 35] the dynamic droop gains of several inverters operating in parallel are tuned independently supposing an ideal star configuration of the system. In that case, each inverter is connected directly through a single equivalent impedance to a common node at which an ideal voltage source is present, which is usually referred to as point of common coupling (PCC). This decouples the dynamics of each inverter from all the others, reducing the problem to the one of a single inverter connected to a stiff grid. However, the assumption of a perfect decoupling between inverters is far from reality, since the impedance between two given inverters on a real low-voltage grid can even be smaller than the one between each inverter and the stiff grid, as shown in Chapter 2.

To address this issue, some different method for tuning the dynamic droop gain has to be proposed, which must consider not only the dynamics of each inverter but also the coupling between them. With this in mind, two methods for the derivation of the dynamic droop gains of a group of inverters will be derived, based on the methods studied for a single inverter.

6.1 SMALL-SIGNAL DYNAMICS OF MULTIPLE INVERTERS WITH IMPROVED DROOP CONTROLLER

The linear system matrix $\boldsymbol{A_{sys}}$ of Eq. (5.18) has been derived considering traditional droop-controlled voltage source inverters. This has to be modified to

contemplate the action of the improved droop controller on the dynamics of the system, which adds a power-dependent term to the phase θ of each inverter:

$$\Delta\dot{\theta}_i = -2\pi k_{P_i}\,\Delta\hat{P} - k_{Pd_i}\Delta\dot{\hat{P}}_i \tag{6.1}$$

Incorporating the action of the improved droop controller to each inverter of the system yields the linear model

$$\begin{pmatrix} \boldsymbol{\Delta\dot{\theta}} \\ \boldsymbol{\Delta\dot{\hat{P}}} \\ \boldsymbol{\Delta\dot{\hat{Q}}} \end{pmatrix} = \boldsymbol{A_{sys}} \begin{pmatrix} \boldsymbol{\Delta\theta} \\ \boldsymbol{\Delta\hat{P}} \\ \boldsymbol{\Delta\hat{Q}} \end{pmatrix} - \begin{pmatrix} \boldsymbol{K_{Pd}\Delta\dot{\hat{P}}} \\ \mathbf{0} \\ \mathbf{0} \end{pmatrix} \tag{6.2}$$

which can be rewritten in the form $\boldsymbol{T\dot{x}_{sys}} = \boldsymbol{A_{sys}x_{sys}}$, with

$$\boldsymbol{T} = \begin{pmatrix} \mathbf{1} & \boldsymbol{K_{Pd}} & \mathbf{0} \\ \mathbf{0} & \mathbf{1} & \mathbf{0} \\ \mathbf{0} & \mathbf{0} & \mathbf{1} \end{pmatrix}. \tag{6.3}$$

The matrix $\boldsymbol{K_{Pd}}$ is diagonal, being composed of the dynamic droop coefficients $k_{Pd_1}, k_{Pd_2}, ...k_{Pd_n}$. Since all non-diagonal elements are zero, these coefficients can simply be written as a row vector $\boldsymbol{k_{Pd}} = diag(\boldsymbol{K_{Pd}})$, where $diag()$ is the main diagonal of the matrix.

The stability of the new system can then be analyzed through the eigenvalues $\lambda_i = \sigma_i + j\omega_i$ of the matrix $\boldsymbol{A^*_{sys}} = \boldsymbol{T^{-1}A_{sys}}$. The invertibility of $\boldsymbol{T}$ is trivially proved, since it is an upper triangular matrix with every element on the main diagonal different from zero. Note that, for the case of conventional droop controller [40] ($\boldsymbol{K_{Pd}} = \mathbf{0}$), the system matrix $\boldsymbol{A^*_{sys}}$ reduces to $\boldsymbol{A_{sys}}$.

6.2 DESIGN METHOD A: EXTENSION OF THE CONTROLLER DESIGN BASED ON ROOT LOCUS

In Chapter 4, studying the root locus plot of a single inverter led to a systematic approach to finding an optimal gain for the dynamic droop controller. As a result, a single parameter can be chosen in a way that the poles of the linearized system are shifted to the desired location, achieving critical damping. This root locus analysis can be extended for the case in which more than one parameter varies to the so-called root contours analysis. However, this is only possible when dealing

with a small number of inverters - normally two - while the selection of parameters is done manually by a human having specific knowledge and intuition on the interpretation of these plots. Besides, each root locus plot does not strictly apply to a system with more than one simultaneously varying gain.

The search for a set of dynamic droop gains is formulated in this occasion as an optimization problem, minimizing a cost function $\Phi(\boldsymbol{k_{Pd}})$. Since it is particularly interesting to avoid system instability but not necessary to improve the response time, the angle δ_i of each eigenvalue λ_i of the linearized system matrix $\boldsymbol{A^*_{sys}}$ is taken into consideration. With this concept, the following cost function can be established:

$$\Phi = \sum_i \delta_i^2, \quad \text{where} \tag{6.4}$$

$$\delta_i = \tan^{-1}\left(\frac{|\omega_i|}{-\sigma_i}\right), \tag{6.5}$$

with $\tan^{-1}$ defined between 0 and π.

The cost is therefore related to the damping ratio of the eigenvalues, which characterize the small-signal dynamics of the system. A smaller cost means in this context better damping. For $0 < |\delta_i| < \pi/2$, the cosine of the angle is the damping ratio of the ith eigenvalue, which increases when minimizing δ_i. Angles greater or equal than $\pi/2$ imply poles with non-negative real part, which indicate system instability and should be avoided by all means. Finally, the case $\delta_i = 0$ represents real negative poles, which are not of interest since they influence the response time of the system but do not compromise its stability.

The optimization is solved numerically by a first-order gradient descent algorithm. This algorithm increases the dynamic droop gains in the direction of maximum damping according to the negative of the gradient, until a stop criterion is reached. In this sense, the Jacobi matrix computed at each iteration step is similar to the one resulting from a sensitivity analysis, although in this case the matrix obtained relates to the sensitivity to the dynamic droop gain.

Figure 6.1 illustrates the optimization process for a system with two inverters in grid-connected mode, resulting in six poles. The original location of the closed-loop poles is denoted on the complex plane with the subscript $_1$, while the location after the optimization carries the subscript $_2$. The pole angles are minimized, hence diminishing the cost Φ and increasing their damping. An interesting side effect is the movement to the right of one of the poles on the real axis, which maintains zero angle and therefore is not contemplated by the optimization.

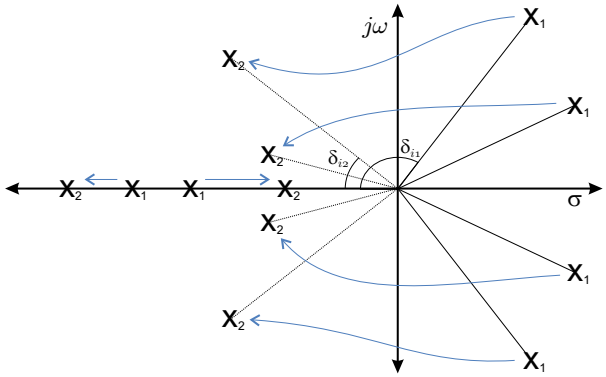

Figure 6.1: Pole movement during optimization. The angle δ of each pole diminishes as the cost function is minimized

The cost function will have a minimum at zero only for the case when system poles can be shifted to the real negative semi-axis by the derivative action on the droops. However, this is not necessarily always the case, since the controller matrix is constrained as it follows from Eq. (6.3), and therefore not every pole can be placed at an arbitrary position. This was as well observed in Fig. 4.7 when studying a single inverter. The damping of the remaining complex conjugate poles can be optimized, but a convergence to zero cost cannot be guaranteed.

6.2.1 *Optimization stop criterion*

The optimization is run iteratively until the gradient step is smaller than a value ϵ, signaling that an extremum has been found. Yet in doing this, the related system of nonlinear equations is only assumed to be convex, which does not guarantee the reached minimum to be global. This is not necessarily an issue, since the proposed optimization is only aimed to stabilize the system by keeping the poles on the left half-plane and maximizing their damping, but not thoroughly searching for an optimal configuration which would complicate the optimization problem and extend the amount of processing power needed, providing little improvement on the dynamics of the system itself.

Moreover, since only the angles of the poles are contemplated on the optimization and not their position on the real negative semi-axis, a discontinuity is implied on the cost function. Those real negative poles will be influenced by the optimized parameters as shown in Fig. 6.1 although not implicitly considered on the selection of the steepest descent. This could cause poles to slide to the right on the real

axis until becoming unstable, increasing abruptly the cost function. In this case, a critical condition is reached and the optimization stops, returning the controller obtained in the preceding iteration.

6.3 DESIGN METHOD B: EXTENSION OF THE CONTROLLER DESIGN BASED ON BODE PLOT

Alternatively to the design based on root locus, which computes exactly the location of all the eigenvalues of the system, the simplified design methods based on Bode plot and line impedance shown for a single inverter in Chapter 4 only compute one single parameter that increases the damping of the system, without the need to derive any complex root-locus plots. However, these two methods are not easy to extrapolate to the case of several inverters.

The design for a single inverter based on Bode plot yields a gain that maximizes the phase margin of a single inverter. For a system with multiple inverters, the concepts of phase and amplitude margin are not uniquely defined but rather dependent on the chosen input/output pairs. Several proposals can be found in the literature to transfer these fundamental concepts to MIMO systems, but they do not exactly match the concept of stability margin of the SISO case [68]. Even the idea of a single Bode plot does not make sense for MIMO systems and instead a Bode plot for every transfer function from input i to output j has to be studied.

The design based on line impedance stressed the role that the coupling between a single inverter and the transformer has on its stability. A linearized line parameter was used as an indicator of this coupling and a dynamic droop gain was derived proportionally to it. However, a system with multiple inverters does not have a single line parameter but an impedance matrix whose elements determine the equivalent coupling between any two nodes of the system. In this sense, some operation has to be performed on this matrix in order to derive a dynamic droop gain that considers the coupling between a given inverter and every other inverter of the system.

Tuning each inverter by only considering its local dynamics is always an option but this can yield erroneous results, since the dynamics of the complete system are heavily dependent on the interactions between inverters as discussed before. Particularly in a real-world low-voltage grid, an inverter cannot be considered a closed system anymore, since the interaction with other inverters alters the dynamics of the system as a whole. As shown in Chapter 5, the eigenvalues of the system are not uniquely dependent on a single inverter and, although a relationship between each oscillating mode and a given inverter can be derived by means

of a sensitivity analysis, there is still a correspondence between all inverters and all modes.

An interesting consequence observed when studying the Bode plot of a single inverter is that the resulting dynamic droop gain is essentially proportional to the natural frequency of the complex pole pair of the system without improved droop. In the case of several inverters, there might be more than a single complex pole pair among the eigenvalues of the matrix $\boldsymbol{A_{sys}}$ which have to be dealt with. A simple yet practical way of doing this is to find an equivalent natural frequency of the interconnected system, which can be computed as

$$\omega_m = \sqrt[K]{\prod_{j=1}^{K} |\lambda_j|}, \tag{6.6}$$

where K is the number of complex poles λ_j of the system without dynamic droops ($\boldsymbol{k_{Pd}} = \mathbf{0}$). This geometric mean of all the oscillatory modes allows for the tuning of the dynamic droop gains in an analogous way as it was done for a single inverter, considering the dynamics of the whole system. The vector $\boldsymbol{k_{Pd}}$ can be obtained from

$$\boldsymbol{k_{Pd}} = \frac{2\pi}{\omega_m} diag(\boldsymbol{k_P}). \tag{6.7}$$

A set of dynamic droop gains can be derived with this simple approach which only requires to compute the eigenvalues of the matrix $\boldsymbol{A_{sys}}$ once instead of depending on an iterative optimization method that can be computationally intensive. However, simplicity comes at the price of having to assign to all the inverters the same time constant to their derivative term. This is not optimal, since the same dynamic droop gain acting on a different inverter can influence the dynamics of the system in different ways.

Moreover, the mean frequency ω_m is computed with the matrix $\boldsymbol{A_{sys}}$, which describes the dynamics of the interconnected inverters with the improved droop control loop left open. Traditional SISO controller design bases on the idea that the open-loop transfer function can be studied and modified to optimize the closed-loop dynamics of the system. However, this is a well-known limitation of controller design for MIMO systems, since the open-loop transfer function for a given input-output pair depends on the way all other loops are closed. Studying the impact that closing other loops has on the dynamics of a given input-output pair will help better assign the dynamic droop gains to each inverter. The concept of relative gain array can be introduced to handle this, which will extract infor-

mation of the coupling between inverters out of the matrix $\boldsymbol{N}$ and exploit it for better damping.

6.3.1 *RGA - Relative gain array*

In a large system that is composed of many dynamic subprocesses that are coupled in a given way, the variables of those processes can interact with each other. In order to control such a system, there are mainly two possibilities. The first approach is known as *multivariable control*, which is a strategy that consists on controlling each subprocess with additional information from the other processes. Although such a control system usually yields satisfactory results, for its implementation it is necessary that all the variables of the system are available at a local level, which can not be the case in a power grid with distributed generation and lack of reliable real-time communication.

The second possibility to control such a system is by means of *multiloop control*. In an ideal multiloop control system, each given subprocess is controlled locally and regardless of the rest of the system as if it was isolated, while changes on the variables of the other processes are considered simply as disturbances. Unfortunately, these disturbances are as well fed back into other control loops, and they interact with each other. A power system with droop-controlled inverters suits perfectly into this scheme, since each inverter represents a local control loop, while all the inverters are coupled to each other through the grid. Understanding the coupling between these multiple control loops is therefore crucial for the implementation of such a multiloop control system.

A widely used tool in control system design for MIMO systems is the relative gain analysis [69, 70]. This technique bases on the Relative Gain Array (RGA), which is a matrix that measures the interaction of all possible SISO pairings between the inputs and outputs of a MIMO system. To better illustrate this, lets study a square linear MIMO system $\boldsymbol{G_C}(s)$, with n inputs u and n outputs y which is controlled by a multiloop controller, as shown in Fig. 6.2.

The idea behind the RGA is to find a measure that determines how the relationship between a given input u_j and a given output y_i is affected by the control of all other variables. The relative gain of a given input-output pair is hence defined as the ratio of two stationary gains that represent first the uncontrolled gain (all other loops open) and second the controlled gain, i.e. the apparent gain when all

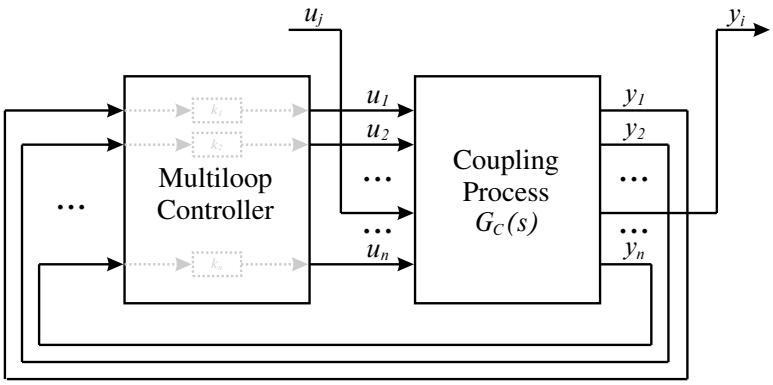

Figure 6.2: Controlled MIMO system with a disconnected input-output pair

other control loops are closed in a way that all other outputs are set to zero. This can be expressed mathematically as

$$\rho_{ij} = \frac{\left.\frac{\partial y_i}{\partial u_j}\right|_{u_k=0 \ \forall \ k\neq j}}{\left.\frac{\partial y_i}{\partial u_j}\right|_{y_k=0 \ \forall \ k\neq i}}. \tag{6.8}$$

Note that this stationary relative gain does not depend on the multiloop controller implemented, provided that it effectively forces the other outputs to zero. A limitation of this analysis is that the MIMO system $\boldsymbol{G_C}(s)$ cannot contain pure integrators, although some workarounds to this exist [71]. Extending Eq. (6.8) to every possible input-output pair gives rise to the RGA matrix, which consolidates all the information on the coupling of the system. The element of the j-th column and i-th row of the RGA matrix gives information of the coupling between the j-th input and i-th output.

$$\boldsymbol{RGA} = \begin{pmatrix} \rho_{11} & \rho_{12} & \cdots & \rho_{1n} \\ \rho_{21} & \rho_{22} & \cdots & \rho_{2n} \\ \vdots & \vdots & \ddots & \vdots \\ \rho_{n1} & \rho_{n2} & \cdots & \rho_{nn} \end{pmatrix} \tag{6.9}$$

An alternative way of computing the RGA matrix is by using the MIMO transfer matrix $\boldsymbol{G}(s)$, which yields

$$\boldsymbol{RGA} = \boldsymbol{G}(0) \odot \boldsymbol{G}(0)^{-T}. \tag{6.10}$$

The symbol $\odot$ denotes element-wise or Hadamard product and $^{-T}$ the transposed inverse of the matrix. Note that the relative gains are usually computed at stationary state, i.e. $s = 0$, whereas an extension to the dynamic RGA ($\boldsymbol{DRGA}(s)$) can be performed by computing the RGA matrix as a function of s [72].

There are some useful properties and interpretations of the RGA matrix that assist in control design, some of which include the following:

- The RGA matrix is a normalized measure of coupling. For a system with full rank, any row or column adds up to one, independently of the scaling of the process $\boldsymbol{G}(s)$.
- If ρ_{ij} is close to zero, the input-output pair ij is decoupled, i.e. the input u_j has no effect on the output y_i.
- Values of ρ_{ij} close to one indicate ideal coupling. The multiloop controller should be designed in a way that input-output pairs with relative gains close to unity are chosen.
- If the RGA matrix is close to diagonal, then the MIMO system is decoupled and well suited for multiloop control.

6.3.2 *RGA applied to the linearized model of the grid*

The linear model of distributed generation derived in Chapter 5 describes the dynamics of the inverters and their coupling through the grid. The inverters represent a multiloop controller while the coupling through the grid is described through the linearized matrix gain N, such that

$$\begin{pmatrix} \boldsymbol{\Delta P} \\ \boldsymbol{\Delta Q} \end{pmatrix} = \boldsymbol{N} \begin{pmatrix} \boldsymbol{\Delta \theta} \\ \boldsymbol{\Delta U} \end{pmatrix}. \tag{6.11}$$

Since the dynamics associated to the inductive and capacitive nature of the power lines are neglected, the RGA matrix shall be directly obtained from

$$\boldsymbol{RGA} = \boldsymbol{N} \odot \boldsymbol{N}^{-T}. \tag{6.12}$$

Despite this simple approach, the proposed RGA matrix cannot be computed, since the matrix $\boldsymbol{N}$ is singular. This is not surprising, since the coupling through the grid in Eq. (5.17) was described in terms of the phases θ at each node, while the power flow is actually described by the phase differences. However, it has been shown that the RGA matrix can still be computed for coupling processes

without full rank by means of the Moore–Penrose pseudoinverse $\boldsymbol{N}^{+}$ [73], resulting in

$$\boldsymbol{RGA} = \boldsymbol{N} \odot (\boldsymbol{N}^{+})^{T}. \tag{6.13}$$

Although some mathematical properties of full-rank RGA don't hold anymore, the matrix obtained still allows for the analysis of the interactions between the nodes of the system. The resulting RGA matrix can be interpreted as a normalized measure of the coupling between the voltage at each node (in amplitude and phase) and the resulting active and reactive power that flows through the grid. Each element of this matrix can be analyzed according to its position as seen in Eq. (6.14) resulting in a relative gain between a given input (voltage amplitude or phase) and a given output (active and reactive power). The RGA matrix can therefore be divided in four sub-matrices according to these inputs and outputs:

$$RGA = \left(\begin{array}{cccc|cccc} \rho_{1,1} & \rho_{1,2} & \cdots & \rho_{1,n} & \rho_{1,n+1} & \rho_{1,n+2} & \cdots & \rho_{1,2n} \\ \rho_{2,1} & \rho_{2,2} & \cdots & \rho_{2,n} & \rho_{2,n+1} & \rho_{2,n+2} & \cdots & \rho_{2,2n} \\ \vdots & \vdots & \ddots & \vdots & \vdots & \vdots & \ddots & \vdots \\ \rho_{n,1} & \rho_{n,2} & \cdots & \rho_{n,n} & \rho_{n,n+1} & \rho_{n,n+2} & \cdots & \rho_{n,2n} \\ \hline \rho_{n+1,1} & \rho_{n+1,2} & \cdots & \rho_{n+1,n} & \rho_{n+1,n+1} & \rho_{n+1,n+2} & \cdots & \rho_{n+1,2n} \\ \rho_{n+2,1} & \rho_{n+2,2} & \cdots & \rho_{n+2,n} & \rho_{n+2,n+1} & \rho_{n+2,n+2} & \cdots & \rho_{n+2,2n} \\ \vdots & \vdots & \ddots & \vdots & \vdots & \vdots & \ddots & \vdots \\ \rho_{2n,1} & \rho_{2n,2} & \cdots & \rho_{2n,n} & \rho_{2n,n+1} & \rho_{2n,n+2} & \cdots & \rho_{2n,2n} \end{array}\right) \begin{array}{l} \left.\vphantom{\begin{array}{c}a\\a\\a\\a\end{array}}\right\} \Delta P \\ \left.\vphantom{\begin{array}{c}a\\a\\a\\a\end{array}}\right\} \Delta Q \end{array} \tag{6.14}$$

$$\underbrace{\phantom{\rho_{2n,1} \quad \rho_{2n,2} \quad \cdots \quad \rho_{2n,n}}}_{\Delta\theta} \qquad \underbrace{\phantom{\rho_{2n,n+1} \quad \rho_{2n,n+2} \quad \cdots \quad \rho_{2n,2n}}}_{\Delta U}$$

To better illustrate this, lets study a simple three-node system with three power lines connected in delta, as seen in Fig. 6.3.

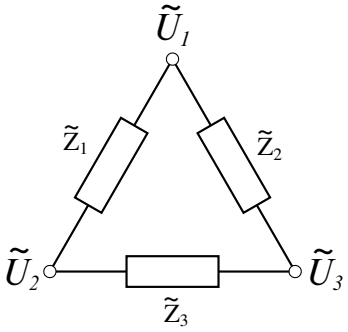

Figure 6.3: Simple three-node system

For the sake of simplicity, lets consider pure inductive and equal lines $\tilde{Z}_1 = \tilde{Z}_2 = \tilde{Z}_3 = jX$. The resulting RGA matrix is

$$\boldsymbol{RGA} = \frac{1}{9}\left(\begin{array}{ccc|ccc} 4 & 1 & 1 & 0 & 0 & 0 \\ 1 & 4 & 1 & 0 & 0 & 0 \\ 1 & 1 & 4 & 0 & 0 & 0 \\ \hline 0 & 0 & 0 & 4 & 1 & 1 \\ 0 & 0 & 0 & 1 & 4 & 1 \\ 0 & 0 & 0 & 1 & 1 & 4 \end{array}\right) \tag{6.15}$$

As expected from the inductive lines, there exist couplings between active power and phase, and reactive power and voltage amplitude. This sort of coupling is well known and is the base for the decoupled control of active and reactive power on HV grids. However, considering the lines $\tilde{Z}_1 = \tilde{Z}_2 = \tilde{Z}_3 = R + jX$ with $X = 2R$ yields a much different RGA matrix, which results in

$$\boldsymbol{RGA} = \frac{1}{45}\left(\begin{array}{ccc|ccc} 16 & 4 & 4 & 4 & 1 & 1 \\ 4 & 16 & 4 & 1 & 4 & 1 \\ 4 & 4 & 16 & 1 & 1 & 4 \\ \hline 4 & 1 & 1 & 16 & 4 & 4 \\ 1 & 4 & 1 & 4 & 16 & 4 \\ 1 & 1 & 4 & 4 & 4 & 16 \end{array}\right) \tag{6.16}$$

In this case, the coupling between active and reactive power becomes apparent and yet again it can be seen that the same control structures that are used in HV systems cannot be implemented in LV grids without having to deal with coupling.

Last but not least, it is interesting to consider different values of impedances. For instance, the RGA matrix for $X_i = 2R_i$ and $|\tilde{Z}_1| = 2|\tilde{Z}_2| = 4|\tilde{Z}_3|$ is:

$$\boldsymbol{RGA} = \frac{1}{630}\left(\begin{array}{ccc|ccc} 228 & 44 & 64 & 57 & 11 & 16 \\ 44 & 260 & 32 & 11 & 65 & 8 \\ 64 & 32 & 240 & 16 & 8 & 60 \\ \hline 57 & 11 & 16 & 228 & 44 & 64 \\ 11 & 65 & 8 & 44 & 260 & 32 \\ 16 & 8 & 60 & 64 & 32 & 240 \end{array}\right) \tag{6.17}$$

It is important to note that the largest values in the RGA matrix are related to the diagonal elements of the four sub-matrices, since the power flowing into a node

can be better controlled by manipulating the voltage at that node. The other elements of the matrix yield a measure of the relative gain between different nodes. For example, the element $\rho_{1,3}$ is larger than $\rho_{1,2}$, since the coupling between nodes 1 and 3 is stronger than the coupling between 1 and 2. A similar analysis can be done with all the elements of the matrix, obtaining a normalized measure of the interactions between the nodes. The RGA matrix is hence a simple yet powerful tool to study the coupling processes that appear in a given power grid.

6.3.3 *Setting the dynamic droop gains with help of the RGA matrix*

Traditionally, the RGA matrix is used as a measure of interactions for multivariable, decentralized control, with the goal of finding the best suitable input-output control pairs. The authors in [74, 75] have shown the effectiveness of RGA in identifying electromechanical modes in different multimachine power systems and in selecting the optimal location for placement of power system stabilizers. This helps select the signals that will participate in the control system but no quantitative information is extracted from the RGA matrix to tune these controllers. Analyzing the physical meaning of the RGA matrix as applied to the coupling matrix $\boldsymbol{N}$ can yield helpful information that aids in the tuning the dynamic droop gains.

The first n rows and columns of the RGA matrix measure the coupling between active power ΔP and the phase $\Delta\theta$ at each node. This sub-matrix can be called $\boldsymbol{RGA_{1,1}}$. Particularly, the main diagonal of $\boldsymbol{RGA_{1,1}}$ relates a change in the phase of a node to the resulting change in the active power flowing through it, which is precisely what the dynamic droop gain k_{Pd} aims to compensate.

When designing the improved droop gain for a single inverter based on line impedance, merely the linearized line parameter was used as an indicator of the coupling between power and phase. The RGA matrix operates in a similar way, giving information on this very same coupling in a more elaborated way. However, the values on the RGA matrix are normalized and have no physical meaning themselves. To overcome this, it is possible to combine this normalized indication of the coupling from the RGA matrix with the mean frequency ω_m obtained when studying the dynamics of the system. The vector of dynamic droop gains results from

$$\boldsymbol{k_{Pd}} = \frac{2\pi}{\omega_m} diag(\boldsymbol{k_P}) \odot diag(\boldsymbol{RGA_{1,1}}). \tag{6.18}$$

By combining the results from the RGA matrix with the eigenvalue analysis of the interconnected system a set of dynamic droop gains is obtained, which ac-

counts for the damping of the oscillatory processes that occur in the interconnected system while considering at the same time the coupling of each inverter and the impact of closing all other control loops. In this way, the tuning methods for a single inverter based on Bode plot and line impedance introduced in Chapter 4 are now combined together into a single method suitable for multiple inverters.

This approach results in a closed-form solution for the problem of tuning the improved-droop gain for several inverters. However, there is no information a priori on the location and damping of the closed-loop poles of the system. In order to guarantee that the resulting dynamic droop gains do effectively damp the system, the poles of the related $\boldsymbol{A}^{*}_{\boldsymbol{sys}}$ matrix should be computed, making sure that the system is stable and that the resulting dominating modes lie in a frequency range much lower than the nominal grid frequency.

6.4 SIMULATION RESULTS FOR AUTONOMOUS OPERATION

To further illustrate the functioning of both design methods, the same three-inverter scenario used for the validation of the model in Chapter 5 is used, which is repeated here for matters of clarity. This system reproduces a MG in autonomous operation, i.e. without connection to a distribution transformer. Two set of dynamic droop gains will be derived by means of the design methods introduced.

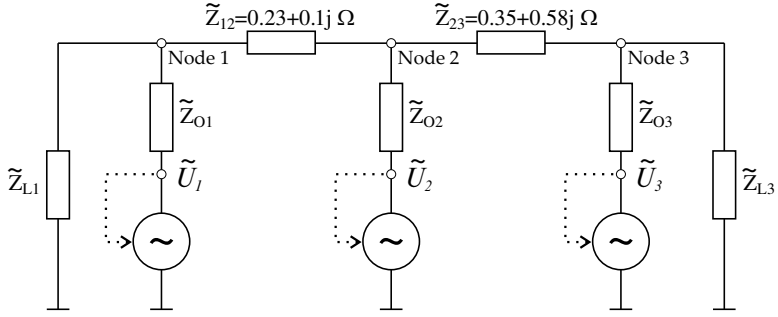

Figure 6.4: Three inverters in autonomous operation

6.4.1 *Design with method A*

The search for an optimal set of dynamic droop gains is performed by running the optimization algorithm introduced in Section 6.2. A trivial nonzero initial condition $\boldsymbol{k_{Pd}} = \mathbf{1} \cdot 10^{-6}$ is used to avoid singularities in the numerical solution. As a result, the optimization increases iteratively the value of each dynamic droop gain, while the angle δ_i of the closed-loop poles and consequently the cost function Φ converge to zero. This iterative process is pictured in Fig. 6.5, showing the evolution of the cost function and the angles of the poles. The stop criterion is fulfilled and an optimal controller is found after 29 iterations.

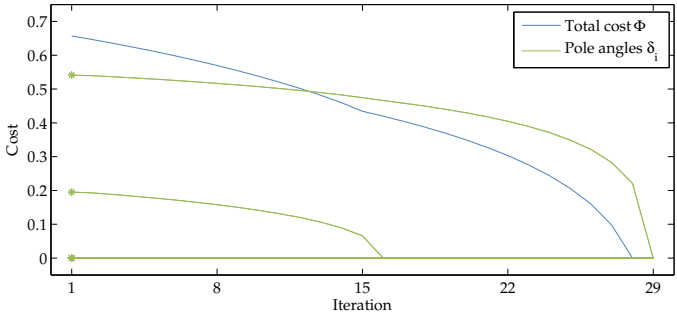

Figure 6.5: Evolution of the angles of the poles and the cost function during the optimization

The resulting vector of dynamic droop gains is

$$\boldsymbol{k_{Pd}} = 10^{-5} \begin{pmatrix} 0.801 & 1.014 & 1.325 \end{pmatrix}, \tag{6.19}$$

and the frequencies of the equivalent zeros of the improved droop controllers are

$$\boldsymbol{\omega_d} = \begin{pmatrix} 11.74 & 9.27 & 7.09 \end{pmatrix}. \tag{6.20}$$

6.4.2 *Design with method B*

The dynamic droop gains computed with method B are related to the dynamics of the system without dynamic droop and to information of the coupling obtained with the RGA matrix. The eigenvalues of the system were shown in Table 5.1. Only two pairs of complex poles result from this system, which yields a mean frequency of

$$\omega_m = \sqrt{45.89 \times 25.82} = 34.42 \text{ rad/s}. \tag{6.21}$$

The RGA analysis yields the matrix

$$RGA_{1,1} = \begin{pmatrix} 0.3716 & -0.0786 & 0.0456 \\ -0.0626 & 0.4655 & 0.1953 \\ 0.0258 & 0.0886 & 0.2575 \end{pmatrix}, \tag{6.22}$$

which results in the dynamic droop gains

$$\boldsymbol{k_{Pd}} = 10^{-5} \begin{pmatrix} 0.735 & 0.587 & 1.060 \end{pmatrix}. \tag{6.23}$$

and the frequencies of the equivalent zeros

$$\boldsymbol{\omega_d} = \begin{pmatrix} 12.79 & 16.02 & 8.86 \end{pmatrix}. \tag{6.24}$$

6.4.3 *Comparison of both methods*

The closed-loop dynamics of the system with the improved droop gains can be evaluated by computing the eigenvalues of the matrix $\boldsymbol{A^*_{sys}}$. Table 6.1 shows the resulting values for the system using the gains obtained with both methods. The eigenvalues of the system without dynamic droop gains are shown as well for reference.

Table 6.1: Eigenvalues of the system in autonomous operation with and without dynamic droop gains

$\boldsymbol{k_{Pd} = 0}$	Method A	Method B
$-11.76 + 44.35j$	-182.43	$-118.85 - 71.47j$
$-11.76 - 44.35j$	-182.43	$-118.85 + 71.47j$
$-14.31 + 21.49j$	-110.69	$-74.50 - 14.79j$
$-14.31 - 21.49j$	-72.52	$-74.50 + 14.79j$
-31.42	-31.41	-31.41
-31.42	-31.41	-31.41
-55.83	-6.22	-7.56
-97.50	-9.47	-12.98

As expected, the poles obtained with method A are all real and stable. The second pair of complex poles shifts to the real axis, while the first pair results critically damped since the stop criterion of the optimization is fulfilled at this point. Two of the poles obtained from the filter with a cutoff frequency of 5 Hz (31.42 rad/s) barely move, while the remaining poles slide along the real axis. The poles obtained with method B are not as well damped, which was expected. However, the

damping of both pairs of complex poles is as well improved with this method, while all other poles stay on the real axis.

The results shown in Table 6.1 can be better visualized on the pole diagram of Fig. 6.6. The poles in grey are those of the system without improved droop, while the ones in green represent the poles obtained with method B and those in blue the ones resulting from method A.

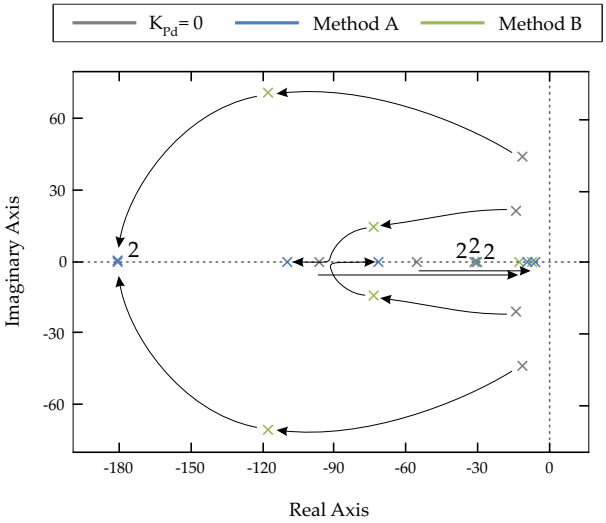

Figure 6.6: Pole diagram of the system with and without dynamic droop gains

Although two pairs of complex poles are still present on the system when implementing the dynamic droop gains obtained with method B (in green), their damping is much higher. Better still, the low frequency poles become dominant, which makes additional damping actually unnecessary. Further optimizing the damping with method A shifts all poles to the real axis, but the performance of the system is barely affected by this, since enough damping is already guaranteed by the dominant slower poles. This stresses again the fact that the design based on RGA is a compromise between different aspects of the system, while the optimization method only focuses on maximizing the damping of all poles, which is not necessarily the best approach.

The simulation done for this three-inverter system in Chapter 5 is repeated implementing the improved droop controller with the gains obtained with both methods. The same configuration and parameters are used as before, exciting the system with a load step of 3.8 kW at node 1. Figure 6.7 shows the results

obtained through simulation implementing the complete model of the system in MATLAB/Simulink. The response without dynamic droop gains is shown with dotted lines for reference.

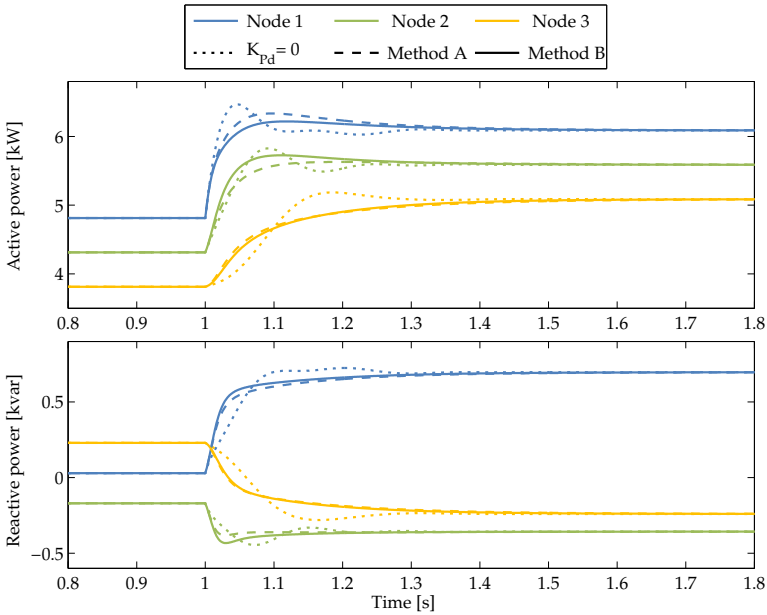

Figure 6.7: Active and reactive power delivered by the inverters after a 3.8 kW load increase at node 1

The increased damping that results from the improved droop controller can be noticed on all three nodes. Although method A is able to critically damp the system, the results obtained with method B are as well satisfactory. The same can be observed in the instantaneous frequency of the inverters, which is shown in Fig. 6.8

The original delayed reaction of the inverters, shown in Fig. 6.8 with dotted lines, is successfully improved by the action of the dynamic droops. Note that the well-damped response of the frequency without improved droops yields an underdamped behavior of the system, while the faster reacting frequencies that result from the improved droop controller damp the system by "'pushing"' the phase and helping it achieve a new stationary value.

The lines in Fig. 6.8 give the false impression that the dynamics of node 1 is worse damped than the rest, since a larger transient frequency deviation can be

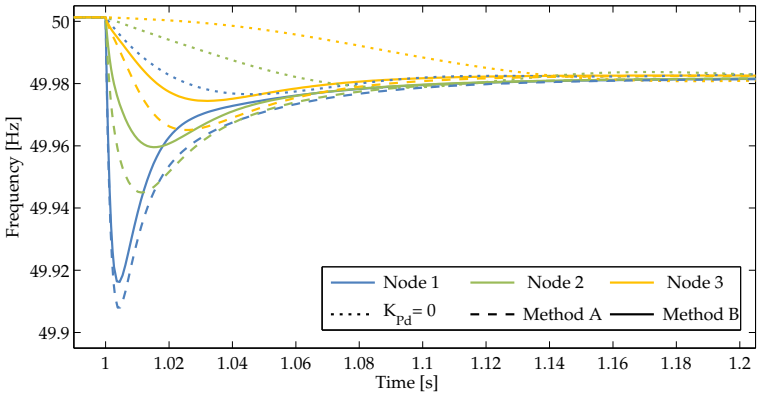

Figure 6.8: Instantaneous frequencies of the inverters after a 3.8 kW load increase at node 1

observed for that node. However, the disturbance is larger at node 1 since the load step is introduced at this node. Consequently, the transient frequency deviation at node 3 is the smallest, since this node is the most distant to the load. The overshoot seen in Fig. 6.8 is hence caused by the equivalent frequency impulse that arises from connecting abruptly the load. The same simulation can be repeated by introducing the load step at different nodes of the system, yielding equivalent results. In those cases, the amplitude of the transient of the instantaneous frequency of each inverter differs from node to node, but the resulting eigenvalues stay unchanged.

The steady state frequency achieved after the load step remains as well unaffected, since the dynamic droops do not modify the stationary gain. A deviation of 19 mHz relates to the load step of 3.8 kW and the static droop gain chosen based on [37] (66.84 kW/Hz for each inverter).

6.5 SIMULATION RESULTS FOR GRID-CONNECTED MODE

An alternative scenario can be considered by connecting the three inverters to the MV power grid through a transformer. The connection to the transformer is done through the impedance $\tilde{Z}_{02}$, which was chosen to be half the average value found in Chapter 2, which better represents a real-world system, since the non-zero impedances $\tilde{Z}_{12}$ and $\tilde{Z}_{23}$ are as well part of the grid. This system models a real-world low-voltage grid with distributed generation. A diagram of this con-

figuration can be seen in Fig 6.9. Note that the grid model has now four nodes, since the transformer has to be as well considered.

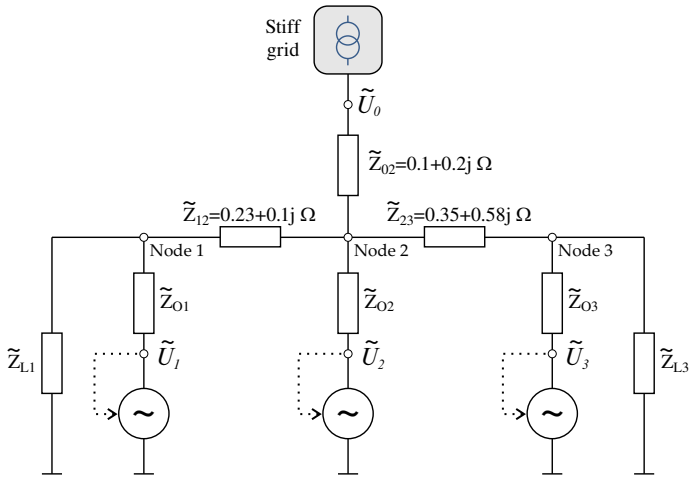

Figure 6.9: Three inverters in grid-connected mode

6.5.1 *Design with method A*

The optimization method is repeated in this case with a small modification. Although this grid has four nodes, there is no way of deriving a dynamic droop gain for the node at which the transformer is connected, since at that node there is merely a simple transformer and its dynamics cannot be modified. With this in mind, the optimization algorithm introduced before is slightly modified removing the dynamic droop gain from the transformer, i.e. forcing the gain to zero. The resulting vector of dynamic droop gains is:

$$\boldsymbol{k_{Pd}} = 10^{-5}\,(0 \quad 1.006 \quad 0.753 \quad 1.408)\,, \tag{6.25}$$

and the frequencies of the equivalent zeros of the improved droop controllers

$$\boldsymbol{\omega_d} = (\infty \quad 9.39 \quad 12.48 \quad 6.68)\,. \tag{6.26}$$

6.5.2 *Design with method B*

The modified grid with an additional impedance connecting to the transformer yields a mean frequency of

$$\omega_m = 28.93 \text{ rad/s} \tag{6.27}$$

Note that, only by adding a node to the system, the mean frequency dropped from 34.42 rad/s, although all the parameters of the inverters were kept unchanged. This is the case, since now power flow between the inverters and the MV grid is possible through the impedance $\tilde{Z}_{02}$, which changes the dynamics of the system.

The RGA analysis yields the matrix

$$RGA_{1,1} = \begin{pmatrix} 0.7163 & 0.0016 & -0.0919 & 0.0798 \\ -0.0182 & 0.3576 & -0.0441 & 0.0357 \\ -0.1414 & -0.0222 & 0.6919 & 0.1575 \\ 0.0230 & 0.0158 & 0.0493 & 0.2920 \end{pmatrix}, \tag{6.28}$$

which results in the dynamic droop gains

$$\boldsymbol{k_{Pd}} = 10^{-5} \begin{pmatrix} 0 & 0.908 & 0.470 & 1.113 \end{pmatrix}, \tag{6.29}$$

and the frequencies of the equivalent zeros

$$\boldsymbol{\omega_d} = \begin{pmatrix} \infty & 10.35 & 20.01 & 8.45 \end{pmatrix}. \tag{6.30}$$

6.5.3 *Comparison of both methods*

This grid-connected system is composed of three inverters and a fourth node with fixed voltage which represents the connection to a stiff grid, resulting in an $\boldsymbol{A_{sys}}$ matrix of rank nine. The nine eigenvalues computed for the system without improved droop controller and those resulting from the implementation of the dynamic droop gains obtained with both methods are shown in Table 6.2.

The same load step as before has been simulated for this system, i.e. a step of 3.8 kW at node 1. In this case, the inverters are configured to provide 4, 3.5, and 3 kW of active power and 0, -200 and 200 var of reactive power at steady state before the load step. The remaining 2.5 kW and 100 var needed to supply the initial loads and maintain the voltage amplitude at its nominal value are provided by the stiff grid, while new steady state values are achieved after the load step. The behavior of the active and reactive power at all four nodes can be seen in

Table 6.2: Eigenvalues of the grid-connected system with and without dynamic droop gains

$\boldsymbol{k_{Pd} = 0}$	Method A	Method B
$-12.87 + 46.07j$	-50.95	$-49.97 + 7.71j$
$-12.87 - 46.07j$	-64.91	$-49.97 - 7.71j$
$-13.60 + 24.45j$	-94.75	$-78.80 + 21.45j$
$-13.60 - 24.45j$	-94.75	$-78.80 - 21.45j$
$-15.00 + 10.12j$	-142.24	$-125.95 + 67.59j$
$-15.00 - 10.12j$	-261.33	$-125.95 - 67.59j$
-44.01	-4.55	-5.32
-59.67	-7.33	-8.10
-106.72	-10.78	-16.85

Fig. 6.10. Four colors are used to distinguish the power flowing into each node, while three different stroke styles are used for each configuration of the improved droop controllers.

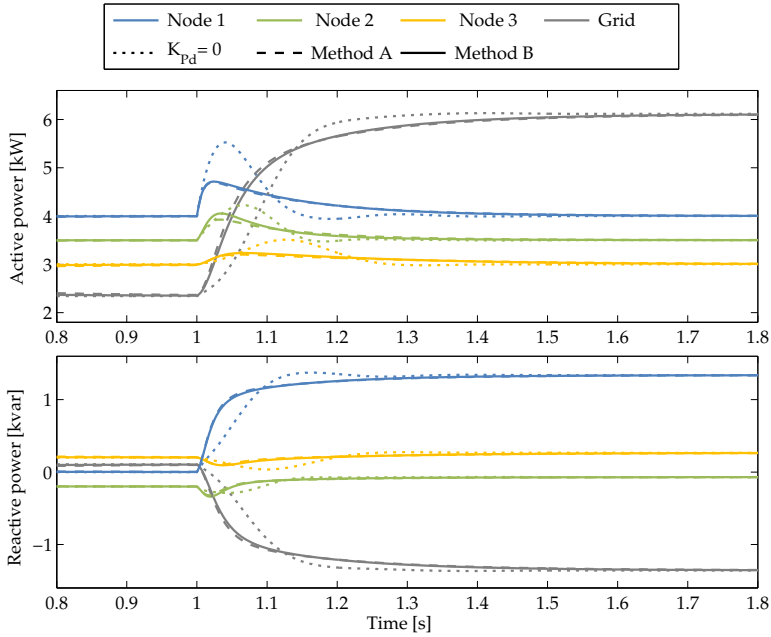

Figure 6.10: Active and reactive power delivered by the inverters after a 3.8 kW load increase at node 1

Note that, after the transient, the increased load causes the stiff grid to provide more active power, while an adjustment in reactive power can be seen as well, due to changes in the power flow through each impedance. However, it is not the end values at steady state that are of interest in this work, but rather the dynamic response of the inverters. Compared to the system without improved droop controller, both methods damp the transient response significantly. The settling time stays almost unchanged, but the observed oscillations are suppressed. A difference between the dynamics resulting from both methods is almost unnoticeable.

Unlike the system in autonomous operation, in grid-connected mode each inverter reacts to the load step but the nominal frequency is restored after the transient, since the voltage from the MV grid stays constant and practically unaffected by the relatively small load step. By observing the trajectory of the instantaneous frequency at each node, which is shown in Fig. 6.11, the compensating effect of the improved droop controller becomes again evident: the phase of each inverter reacts faster with the improved droop controller, which helps achieve a stationary value without oscillations. The impact of the dominant poles of the system becomes clear as well, yielding small differences between both methods.

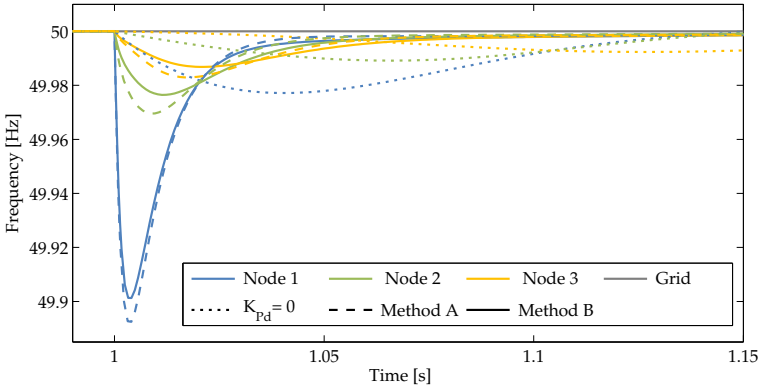

Figure 6.11: Instantaneous frequencies of the inverters after a 3.8 kW load increase at node 1

6.6 PRACTICAL CONSIDERATIONS AND ROBUSTNESS OF THE APPROACH

The implementation of the improved droop controller and its design based on the two methods proposed have proven capable of damping a power system with distributed generation. The methods proposed achieve good results both for islanded and grid-connected systems. However, questions arise regarding the practicability and robustness of this approach.

The improved droop controller itself has been shown to be rather robust regarding parameter variation, since the resulting small-signal dynamics of a given system stay fairly unaffected by the choice of linearization point. Nevertheless, there are two aspects that are critical to the correct functioning of such a distributed power system. First of all, its topology has to be well known, since the coupling between inverters plays a decisive role in the dynamics of the interconnected system and the related dynamic droop gains necessary to damp it. The availability of such information has been taken for granted in this thesis and all the examples shown are based on a given power system, with a known distribution of power lines.

Since knowing the values of the impedances in a grid is crucial to understanding the dynamics of the system, several methods to identify the equivalent impedance seen by an inverter can be found in the literature. Passive methods are based on monitoring grid distortions and using this to estimate the grid impedance between the inverter and a virtual point where the voltage is considered constant. A major drawback of this method is that the variations present on the grid might not be sufficiently large to be detected, failing to yield an estimation of the impedance. To overcome this, active identification methods create deliberately a disturbance on the grid so that the impedance can be then calculated based on the response to the distortion. The most common disturbances are summarized in [76], and require either the injection of a signal of higher frequency, the generation of a transient, or the variation of the fundamental frequency of the inverter. Although this approach has been successfully tested for a single grid-connected inverter in [77], there are concerns regarding the scalability of such an identification, since signals injected by different inverters could interfere with each other, yielding erroneous results.

In any case, knowing the topology of the power lines that make up a grid should not be a challenge in any modern power system, where the distribution of the power lines and their properties can be well identified and documented. An example of such documentation for a benchmark German low-voltage grid can be found in Appendix I.

A second and more critical characteristic of the proposed stabilization by means of the improved droop controller is that the parameters of *all* the inverters present on a given grid have to be set properly in order to assure stable operation. Whether this is done by a central master controller or in a decentralized way does not play any role. Decentralized computing techniques and peer-to-peer networks have gained increasing momentum in the last decade, and several researchers are working on agent-based systems that can solve different kinds of optimization problems related to the distributed generation of electricity in a decentralized way [14, 78, 79]. There might be security and data privacy protection issues, but those are not topics of this work. Nonetheless, what remains critical is the necessity to tune the dynamic droop gains of *all* the inverters of the system by assessing the stability of the system as a whole, rather than studying and stabilizing each inverter as an isolated system.

Keeping in mind that the small-signal stability of a grid with distributed generation depends on the resulting dynamics that arise from the interactions between inverters, and that this dynamic behavior is damped by assigning a dynamic droop gain to each and every inverter, a simple question arises naturally: what happens if one of the inverters of the system cannot implement the dynamic droop gain it was assigned, either because of lack of communication or because its software does not allow it? Put in other terms: can the stability of the system still be guaranteed, if the improved dynamic gains which were derived to stabilize the system are not implemented by *all* the inverters?

In order to evaluate such a situation, the simulation for the grid-connected system studied in the previous section is repeated with some variations, which will be represented in two cases, namely case I and case II. In case I, the dynamic droop gain of the inverter at node 2 is removed. The behavior of the system to a load step under these conditions is shown in Fig. 6.12 with dashed lines. In case II, both static and dynamic droop gains of the inverter at node 2 are removed, which is shown with solid lines. The behavior of the system without dynamic droop gains is shown as a reference with dotted lines. Four different colors are used to distinguish each node.

Compared to the behavior of the system without improved droop, the overall dynamics are still improved even though one inverter does not implement the dynamic droop gain. Nevertheless, the active and reactive power flowing into node 2 in case I results clearly worse damped than it was without dynamic droops ($\boldsymbol{k_{Pd}} = \mathbf{0}$). This is somehow curious, since one would expect that the damping action of the dynamic droop gains acting on all other inverters would still help compensate the oscillations on the system. However, the other inverters can only damp locally the oscillations at nodes 1 and 3, while node 2 is left to behave

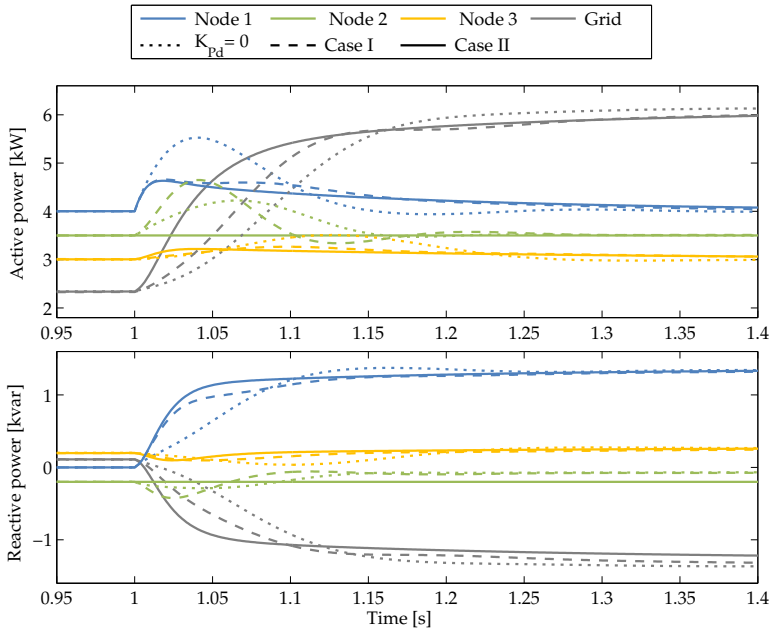

Figure 6.12: Different response of the system when one of the inverters does not implement a dynamic droop gain

with the natural dynamics that emerge from the configuration of the system. As a result, a larger and worse damped transient appears at this node.

Repeating the simulation for several different systems and parameters shows that implementing only partially the dynamic droop gains derived for a given system cannot guarantee its stability. In some cases, such as shown in Fig. 6.12, the resulting dynamics at the node that does not implement the dynamic droop is worse damped but the system remains stable, whereas in other cases the absence of a dynamic droop gain at a single node jeopardizes the stability of the whole system. A sweeping statement cannot be done in the sense as to whether a system will be stable or not when one or more inverters are not able to implement the computed dynamic droop gains. The only option left is to perform an eigenvalue analysis with the corresponding dynamic droop gains set to zero and asses the stability of the system in that way.

A totally different situation arises in case II. Since the inverter at node 2 has both its static and dynamic droop gains set to zero, it acts injecting constant power regardless of any change in frequency and therefore does not react to the load

step. There is no transient behavior at node 2, while the dynamics of the rest of the system are successfully damped by those inverters that do implement a dynamic droop gain. Completely removing the feedback from the inverter at node 2 hence reduces the order of the system and yields a better dynamic response than implementing only the static droop gain.

From these observations it can be noted that an inverter should only be configured with a static droop gain if and only if it can also implement a dynamic droop gain accordingly. Certainly, this inverter won't be able to provide ancillary services to the grid, but at least it won't jeopardize its stability either.

6.7 A LARGE-SCALE REAL-WORLD SCENARIO

Several simulations with one and three inverters have been shown throughout this thesis with the purpose of clarifying and illustrating the functioning of the inverters and the improved droop controller. The methods derived were tested through simulations for systems with one and three inverters. However, the scalability of these methods should also be studied, considering its potential contribution to a future power system with a large amount of decentralized power generation.

With this in mind, a group of power inverters in a real-world low-voltage grid is configured to provide load following energy and voltage control through the implementation of static droops. See Appendix I for details on the benchmark grid under study. Ten out of the 60 nodes of the grid at which there are residential buildings connected are chosen to inject energy in a distributed way, as it would be the case in a future virtual power plant. An inverter is connected to each one of these nodes, each providing 1 kW of active power in steady state. The active and reactive power droops are selected randomly with some dispersion, assuming that an EMS has assigned a larger participation in the ancillary service product to some nodes. The mean values of the static droops represent an injection of 1 kW for a frequency deviation of 100 mHz, and 1 kvar per Volt. The exact droop gains implemented at each inverter can be seen in Table 6.3.

The chosen configuration represents a viable future scenario for decentralized generation of energy and ancillary services as discussed in [80]. Assuming inverters with a rating of 10 kVA, the parameters proposed are easily implemented without exceeding their power rating. The total distributed load of the system of 31.1 kW is provided in part by the inverters and the rest comes from the MV grid through the distribution transformer. Although the amount of power being injected and circulating through the grid lies perfectly within the practicable limits of the inverters and the power lines, the question that remains unanswered at

this point is whether such a configuration would show stable small-signal dynamics.

To study the dynamics of such a system that implements only traditional droop controllers, a simulation is carried out. The frequency at the transformer drops 100 mHz at $t = 1$ second and the simulation extends over a few seconds showing the theoretical unstable behavior of the system under test, according to the nonlinear model of Chapter 5. The behavior of the active power injected by each inverter can be seen in Fig. 6.13, which is clearly unstable. The same conclusion is obtained by computing the 31 poles of the system, ten of which have positive real parts.

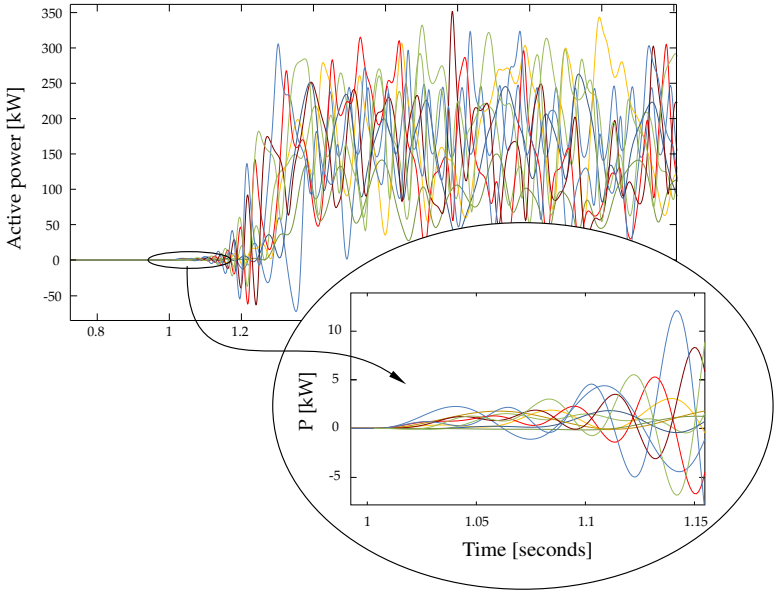

Figure 6.13: Active power injected by the inverters after a disturbance at the transformer at $t = 1$ second

A real system with the parameters proposed would probably not come to oscillate in such a chaotic way, since different safety mechanisms would take the inverters out of operation, disconnecting them before exceeding their power ratings so disproportionately. Either way, the dynamics of the system is unstable, which renders such a configuration impracticable. The zoomed area in Fig. 6.13 shows that the system's behavior assimilates an unstable linear system in the range of interest, i.e. within a few kW, which is consistent with Lyapunov's first method

for stability. A linear controller, such as the improved droop controller proposed, can hence stabilize this unstable system.

Considering both design methods introduced, two sets of dynamic droop gains can be derived. For method A, the optimization is run as done before, with the difference that the size of the system is now much larger. This yields Jacobi matrices of bigger size, the inversion of which is computationally more expensive, which causes the optimization to take a longer time. However, a set of dynamic droop gains is found after 80 iterations, which were processed in about 4.3 seconds running on a PC with 4 GB of RAM and a quad-core microprocessor @ 2.4 GHz. The iterative optimization process can be visualized in Fig. 6.14, which shows the minimization of the angles of all the poles of the system. The five pairs of complex poles that were unstable are highlighted initially in red, denoting an angle larger than $\pi/2$. Withing a few iterations, these poles are damped, resulting in stable dynamics. Note that, in this case, a critical damping of all the poles of the system is not achieved.

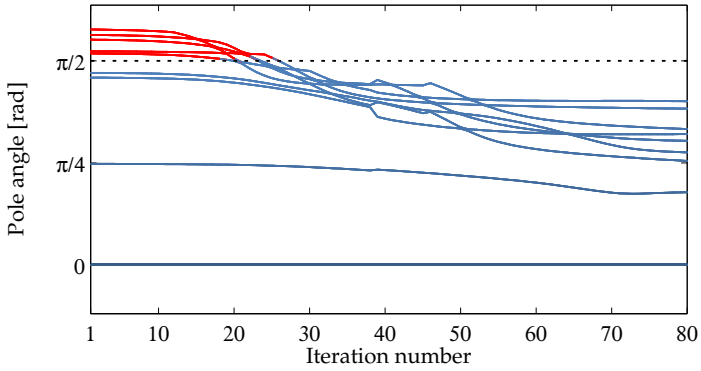

Figure 6.14: Evolution of the angles of the poles during the optimization

For method B, a mean frequency of 12.203 rad/s is found computing the 31 poles of the system without improved controller. The RGA matrix is computed from the admittance matrix of the system and a set of dynamic droop gains is obtained according to Eq. (6.18). The resulting dynamic droop gains obtained with both methods for each inverter, together with the static droop gains and the equivalent zeros, can be found in Table 6.3.

The unstable poles of the system are shifted to the left half-plane by implementing the dynamic droop gains resulting from either two methods. To illustrate this, the poles of the system without improved droop controller are plotted in grey in

Fig. 6.15, while the poles that result from implementing the dynamic droop gains obtained with method A and B are shown in blue and green respectively.

Table 6.3: Parameters used for the simulation of a real-world low-voltage grid

Node	k_P	k_Q	$k_{Pd}(A)$	$\omega_d(A)$	$k_{Pd}(B)$	$\omega_d(B)$
15	0.1023	1.0225	0.0244	8.75	0.0734	8.75
21	0.0982	0.9821	0.0287	13.78	0.0448	13.78
27	0.1008	1.0082	0.0245	14.88	0.0426	14.88
33	0.1099	1.0988	0.0332	21.67	0.0319	21.67
39	0.1057	1.0574	0.0253	16.38	0.0406	16.38
45	0.0937	0.9373	0.0023	12.98	0.0453	12.98
51	0.1107	1.1073	0.0268	7.65	0.0909	7.65
57	0.0932	0.9322	0.4525	20.00	0.0293	20.00
63	0.1092	1.0922	0.4195	21.05	0.0326	21.05
69	0.0967	0.9673	0.0293	25.65	0.0237	25.65

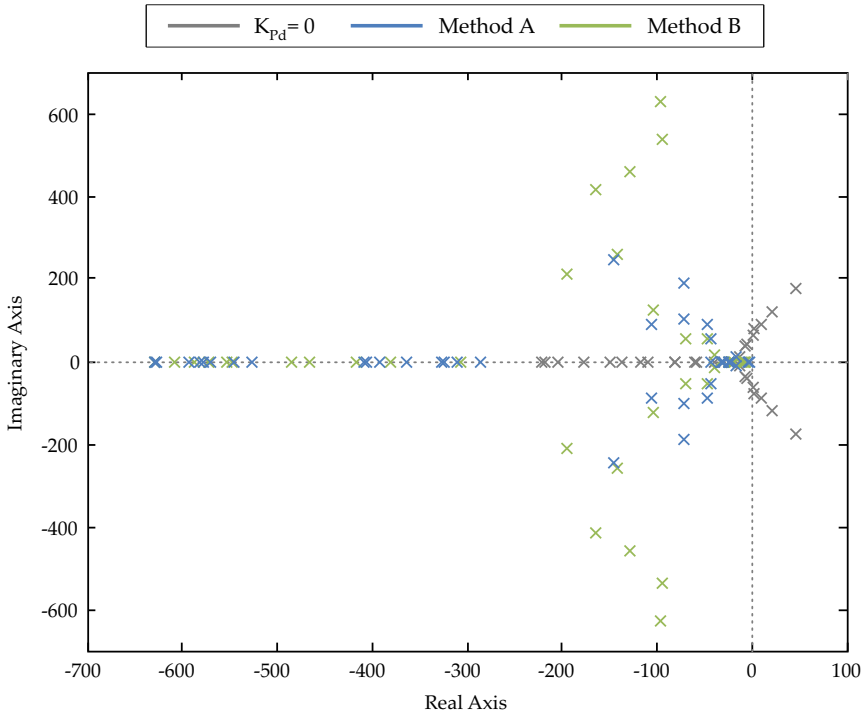

Figure 6.15: Poles of the system with and without dynamic droop gains

Note that the damping obtained with method A is greater, but at the same time some poles shift further to the right on the real axis, which makes their dynamics dominant. This can be better seen by simulating again a frequency step at the transformer and observing the transient response of the inverters when implementing the improved droop controller. The behavior resulting from both methods can be seen in Fig. 6.16.

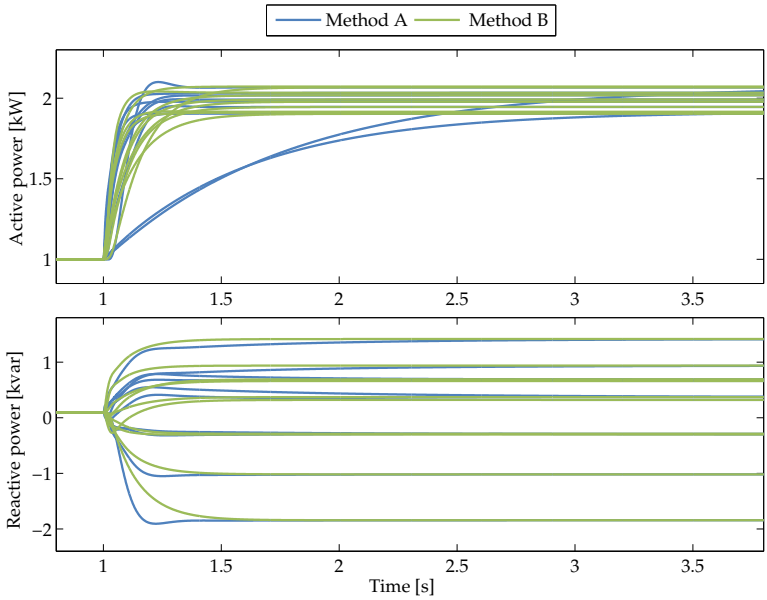

Figure 6.16: Active and reactive power injected by the inverters after a frequency drop at the transformer

The resulting dynamics is in both cases clearly stable, although the impact of the dominant poles of method A can be seen at two of the inverters, whereas the responses of the inverters obtained with method B are more balanced. The end values achieved after a few seconds by each inverter differ, since their static droop gains are all different. Collectively, the ten inverters inject 10 kW of active power as a reaction to the frequency drop of 100 mHz. This can be seen as well at the transformer, which is shown in Fig. 6.17.

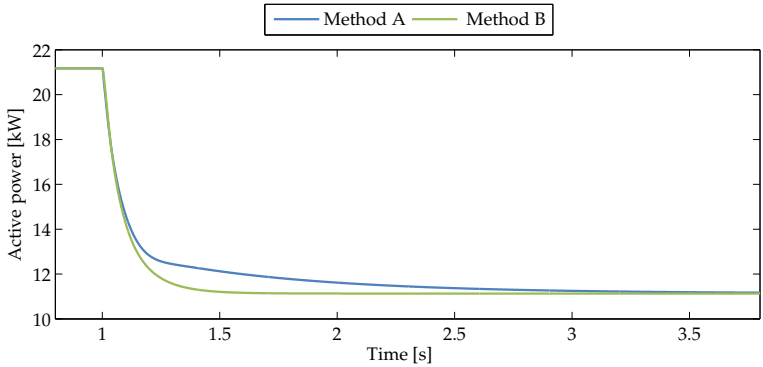

Figure 6.17: Active and reactive power through the transformer

Although the inverters respond to the frequency step with different dynamics, together they form a stable virtual power plant that can inject load following energy into the MV grid through the transformer with an equivalent power droop and a resulting dynamic response. This equivalent combined response of the distributed system will be topic of Chapter 7.

7

REDUCED-ORDER MODEL OF A LOW-VOLTAGE GRID WITH DISTRIBUTED GENERATION

When studying the dynamics of distributed generation in a LV grid, be it in a MG or a VPP, the MV grid to which the system is connected is usually considered stiff. Its dynamics and its power droops are entirely disregarded, and an ideal voltage source is used to model it as an infinite bus instead. This helps study the behavior of the LV grid but disregards the dynamics and the droops of the distributed generators present in the MV grid and hence the interactions between both. In a similar manner, traditional power system stability analysis is carried out at HV and MV levels, disregarding the behavior of the LV grids or considering them as mere loads [4].

However, in a future scenario with larger amounts of distributed generation at the LV level, the dynamics and the presence of power droops might play an important role on the stability of the power system. For instance, inter-area oscillations could appear between two LV grids that interact over a MV grid, or the dynamics of one grid could affect the behavior of the other.

Running a complete simulation of a power system including details of the HV, MV, and LV grids would of course allow to study in detail the stability of the system, but the implementation of such a model is unrealistic, since the immense amount of nodes present in a power system such as the synchronous grid of continental Europe (ENTSO-E) would render any simulation impracticable.

A suitable approach to solving the problem of simulating such a large system is to build hierarchical models that can be integrated into higher-level simulations as needed. Although this is usual practice in the power stability analysis, very little has been done up to date to include aggregated LV models into higher-voltage grids. Reduced-order models of AC and DC MG can be found in the literature within the scope of stability analysis [81–83] but these studies focus on the islanded operation of a MG rather than on the interactions between LV and MV grids.

In the following, a nonlinear reduced-order model for a LV grid with distributed generation will be proposed, based on an equivalent single inverter which can be later integrated hierarchically into the model of a MV grid.

7.1 PROPOSED MODEL

The easiest way to derive a reduced-order model of the system would be to apply order-reduction techniques to the linearized model presented in Chapter 5. In this way, a state space representation of reduced order could easily be achieved. However, instead of making use of mathematical tools to derive systematically a reduced-order model of the system, a given model structure is followed. This aims to derive a set of parameters with physical meaning rather than to obtain some values that are correct in a mathematical sense but do not provide any further understanding on the functioning of the system.

The proposed structure of the reduced-order model consists in a single droop-controlled inverter connected to the grid through an impedance of value $\tilde{Z} = R + jX$, as seen in Fig. 7.1.

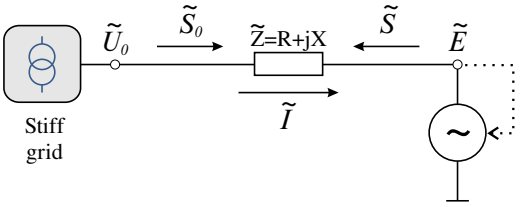

Figure 7.1: Proposed reduced-order model

The stiff grid is represented at the point of coupling with the MV grid by the voltage phasor $\tilde{U}_0 = U_0$, while the voltage $\tilde{E} = Ee^{j\theta}$ of the equivalent inverter is governed by the equations:

$$f = f_{nom} - k_{Pf}(\hat{P} - P_s) - k_{Qf}(\hat{Q} - Q_{set}) \tag{7.1}$$

$$E = E_{nom} - k_{QE}(\hat{Q} - Q_s) - k_{PE}(\hat{P} - P_{set}) \tag{7.2}$$

$$\theta = 2\pi T_{Pd} f + \int 2\pi f dt \tag{7.3}$$

Equations (7.1) and (7.2) implement active and reactive power droops on the equivalent inverter. Under nominal conditions, the inverter has a frequency $f = f_{nom}$ and a voltage amplitude $E = E_{nom}$, while it injects an apparent power $\tilde{S}_{set} = P_{set} + jQ_{set}$. Note that two cross-coupled droop gains k_{Qf} and k_{PE} are included in these equations. Although traditional droop-controlled inverters do not implement this kind of cross-coupled droops, it is important to introduce them in the equivalent reduced-order model to account for the coupling of active and reactive power through the power grid, which will become clearer when studying the equivalent model of a real-world grid in Section 7.3.

The dynamics of the equivalent inverter are modeled including a dynamic droop in Eq. (7.3). Although this term is not mandatory on an equivalent inverter and does not increase the order of the model, it allows for a better fitting of the dynamics of the reduced-order model to that of the complete system, since it allows to better tune the zeros of the equivalent system.

The active and reactive powers $\hat{P}$ and $\hat{Q}$ are modeled by first-order filters, which can be written in the s-domain as

$$\hat{P}(s) = \frac{1}{1 + sT_P} P(s), \tag{7.4}$$

$$\hat{Q}(s) = \frac{1}{1 + sT_Q} Q(s), \tag{7.5}$$

where P and Q are the instantaneous active and reactive power injected by the equivalent inverter. These two equations can be related to the filters on the power estimations of the inverters on the grid or as well be interpreted as an equivalent inertia of a rotating generator as discussed in Chapter 3. In any case, both interpretations relate to the equivalent dynamics of distributed power generation in the grid.

Equations (7.1) through (7.5) are essentially similar to those of a single inverter connected to a stiff grid, except from the cross-coupled droop gains. The model becomes nonlinear when considering the power flow through the impedance $\tilde{Z}$, which couples the voltage $\tilde{E}$ from the equivalent inverter to the voltage U_0 at the stiff grid, introducing a nonlinearity into the model. The premise behind this modeling approach is that a given LV grid with distributed generation, as seen from the point of coupling to the MV grid, will behave similarly to an equivalent single inverter connected at the same point through an equivalent impedance. However, the parameters of the equivalent inverter and the equivalent coupling impedance will differ from those of each inverter, and have to be identified accordingly in order to correctly reproduce the behavior of the system.

7.2 PARAMETER FITTING

A total of eleven parameters define the reduced-order model of the system. These parameters can be divided into three groups, according to their physical meaning:

- Four parameters are related to the power flow in steady state when the system is operating at nominal values, i.e. two real values for the equivalent impedance $\tilde{Z}$ (R and X) and two real values for the voltage phasor $\tilde{E}$ (E and θ).
- Another four parameters are related to the power flow in steady state when the frequency and/or voltage differ from nominal values. These are the four droop gains of the equivalent inverter (k_{Pf}, k_{QE}, k_{Qf} and k_{PE}).
- Three parameters relate to the linearized dynamic response of the system, namely the time constants T_P, T_Q, and T_{Pd}.

Since these sets of parameters can be attributed to distinct processes on the system, they can be identified and/or tuned separately. The voltage U_0 of the stiff grid is considered exogenous to the model.

7.2.1 *Coupling impedance and nominal operating point*

In steady state, both the stiff grid and the equivalent inverter have a voltage value that, together with the impedance $\tilde{Z}$, defines the current $\tilde{I}$ and therefore the power flow $\tilde{S}_0$ into the system. Although the voltage $\tilde{U}_0$ and the current $\tilde{I}$ can be taken as given and even measured in a real system, the voltage $\tilde{E}$, as well as the impedance $\tilde{Z}$ and the apparent power $\tilde{S}$ injected by the equivalent inverter are prototypical values that do not exist at any point of the real grid. These have to be estimated indirectly based on observations made at the point of coupling with the stiff grid, which can be obtained either through simulations or by solving analytically for a known system with distributed generation. The way in which the power $\tilde{S}_0$ flows to the different nodes of the real grid is at this point unimportant. What interests is only the current $\tilde{I}$ flowing into the grid as a response to the distributed generators and loads.

For a given nominal voltage $\tilde{U}_{0nom}$, the current $\tilde{I}_{nom}$ is related to the equivalent impedance $\tilde{Z} = R + jX$ and to the nominal voltage of the equivalent inverter $\tilde{E}_{nom} = E_{nom}e^{j\theta_{nom}}$ through

$$\tilde{U}_{0nom} = \tilde{I}_{nom}\tilde{Z} + \tilde{E}_{nom}. \tag{7.6}$$

Changing the nominal value $\tilde{U}_{0nom}$ to $\tilde{U}_{0\Delta U} = \tilde{U}_{0nom} + \Delta U$ would make the droop-controlled inverters react to this new voltage, reaching a new equivalent operating point $\tilde{E}_{\Delta U}$. However, since the inverters present a lagged response, they remain momentarily unaffected by a sudden change on the voltage $\tilde{U}_0$ until the droop controllers take over. A stepwise change on amplitude creates therefore an initial step on the current $\tilde{I}$ that depends only on the equivalent impedance $\tilde{Z} = R + jX$ and the nominal inverter voltage $\tilde{E}_{nom}$, which can be expressed as

$$\tilde{U}_{0\Delta U} = \tilde{I}_{nom\Delta U}\tilde{Z} + \tilde{E}_{nom}. \tag{7.7}$$

Separating Eqs. (7.6) and (7.7) in real and imaginary parts yields a system of four linear equations with four unknowns ($R, X, E_{nom}, \theta_{nom} \in \Re$), which can be easily solved for known values of $\tilde{U}_0$ and $\tilde{I}$. As a result, the equivalent impedance $\tilde{Z}$ and the nominal operating point $\tilde{E}_{nom}$ are found.

The equivalent impedance obtained refers to the coupling of the equivalent inverter to the stiff grid. Note that this value is not necessarily equal to the equivalent impedance that can be obtained through computations with the admittance matrix of the grid, since the latter considers only the nature of the power lines but disregards the power flow produced by the distributed generators. Moreover, all the loads that were present on the complete LV grid have now been included into the equivalent power source. The set-point of the apparent power of the equivalent inverter can be computed as

$$\tilde{S}_{set} = P_{set} + jQ_{set} = -\tilde{E}_{nom}\tilde{I}^*_{nom}, \tag{7.8}$$

which reproduces the power imbalance in the grid, i.e. the difference between loads and distributed generation. The single equivalent inverter recreates, at nominal values, both distributed generation and loads.

7.2.2 *Droop gains*

After the transient response of the inverters, the current $\tilde{I}$ settles at a value $\tilde{I}_{\Delta U}$ and the equivalent inverter has a voltage of value

$$\tilde{E}_{\Delta U} = \tilde{U}_{0\Delta U} - \tilde{I}_{\Delta U}\tilde{Z}, \tag{7.9}$$

which yields the power

$$\tilde{S}_{\Delta U} = P_{\Delta U} + jQ_{\Delta U} = -\tilde{E}_{\Delta U}\tilde{I}^*_{\Delta U}. \tag{7.10}$$

In a similar fashion, a step Δf on the frequency of the voltage source U_0 triggers the droop controllers of the distributed generators, which, given enough settling time, yields a new current $\tilde{I}$ of value $\tilde{I}_{\Delta f}$. The equivalent inverter will settle at the same frequency and with a voltage of value

$$\tilde{E}_{\Delta f} = \tilde{U}_0 - \tilde{I}_{\Delta f}\tilde{Z}, \tag{7.11}$$

which yields the power

$$\tilde{S}_{\Delta f} = P_{\Delta f} + jQ_{\Delta f} = -\tilde{E}_{\Delta f}\tilde{I}^*_{\Delta f}. \tag{7.12}$$

Evaluating the droop equations (7.1) and (7.2) for the voltage and frequency steps yields a system of four linear equations:

$$0 = -K_{Pf}(P_{set} - P_{\Delta U}) - K_{Qf}(Q_{set} - Q_{\Delta U}) \tag{7.13}$$
$$E_{nom} - E_{\Delta E} = -K_{PU}(P_{set} - P_{\Delta U}) - K_{QU}(Q_{set} - Q_{\Delta U}) \tag{7.14}$$
$$\Delta f = -K_{Pf}(P_{set} - P_{\Delta f}) - K_{Qf}(Q_{set} - Q_{\Delta f}) \tag{7.15}$$
$$E_{nom} - E_{\Delta f} = -K_{PE}(P_{set} - P_{\Delta f}) - K_{QE}(Q_{set} - Q_{\Delta f}) \tag{7.16}$$

Solving this system returns the droop gains K_{Pf}, K_{Qf}, K_{PU}, and K_{QU} of the equivalent inverter.

7.2.3 *Linearized dynamics*

Considering the frequency f and the voltage U_0 at the transformer as inputs and the active and reactive power flow P_0 and Q_0 as outputs yields a 2-input 2-output MIMO system. The derivation of the transfer functions of each input-output pair can be obtained from the linearized state-space model of the system shown in Eq. (5.22).

Using the nominal conditions as linearization point, the transfer matrix of the system can be expressed as

$$\boldsymbol{G_{sys0}}(s) = \begin{pmatrix} \frac{\Delta P_0}{\Delta f}(s) & \frac{\Delta P_0}{\Delta U_0}(s) \\ \frac{\Delta Q_0}{\Delta f}(s) & \frac{\Delta Q_0}{\Delta U_0}(s) \end{pmatrix}. \tag{7.17}$$

For a system with n distributed generators, each of these four transfer functions has an order $3n$.

In a similar manner, the transfer matrix of the reduced order system can be expressed as

$$\boldsymbol{G_{eq}}(s) = \begin{pmatrix} \frac{\Delta P_0}{\Delta f}(s) & \frac{\Delta P_0}{\Delta U_0}(s) \\ \frac{\Delta Q_0}{\Delta f}(s) & \frac{\Delta Q_0}{\Delta U_0}(s) \end{pmatrix}, \tag{7.18}$$

which are third order transfer functions that depend on the eleven parameters of the equivalent model.

When solving for the coupling impedance and the nominal operating point, the response of the current immediately after the voltage step was considered. On the other hand, the steady state values of the current were used when solving for the droop gains. From a dynamic system point of view, this means that the initial and final values of the reduced system match with those of the complete system. Put in mathematical terms, this implies:

$$\boldsymbol{G_{sys0}}(0) = \boldsymbol{G_{eq}}(0), \quad \boldsymbol{G_{sys0}}(\infty) = \boldsymbol{G_{eq}}(\infty), \quad \forall\, T_P, T_Q, T_{Pd}. \tag{7.19}$$

Although the initial and final values already match, the transfer functions in $\boldsymbol{G_{sys0}}(s)$ and $\boldsymbol{G_{eq}}(s)$ should depict a similar dynamic behavior for the whole frequency range. A perfect fitting of both is of course impossible, given the reduced order of the equivalent model. However, the time constants T_P, T_Q, and T_{Pd} can be optimized to best fit the transfer functions. This can be formulated as an optimization problem posed to minimize the quadratic objective function

$$\sum_{k=1}^{m} |\boldsymbol{G_{sys0}}(j\omega_k) - \boldsymbol{G_{eq}}(j\omega_k)|^2, \tag{7.20}$$

which constitutes a nonlinear least-squares optimization problem. A valid set of m data points is obtained by sampling Eqs. (7.17) and (7.18) at m frequencies ω_k ($m >> 3$). The three equivalent time constants can be found out by solving the nonlinear least-squares problem. A suitable algorithm for solving such a problem can be found for instance in [84].

7.3 REDUCED-ORDER MODEL OF A REAL-WORLD GRID

A large-scale real-world scenario with sixty households and ten distributed generators was examined in Chapter 6. The resulting active and reactive power flow through the transformer after a frequency step was shown in Fig. 6.17 for the dynamic droop gains derived with methods A and B. The following reduced-order model will be obtained for the system with the droop gains resulting from

Method B, with the goal of reproducing the same dynamics at the transformer. The same process can be easily repeated for the dynamics resulting from Method A.

Out of the 31.1 kW of load present in the grid, 10 kW are supplied by the distributed generators. Additionally, each distributed generator injects 0.1 kvar of reactive power at nominal conditions. The MV grid has to supply the remaining 21.1 kW of active power, as well as enough reactive power necessary to maintain a nominal voltage of 400 V_{rms} phase to phase at the transformer. According to the droop-controlled inverters used for distributed generation, a deviation from nominal values at the transformer triggers a deviation in active and reactive power flow, which is proportional to the droop gains on the inverters. Studying these deviations allows for the identification of the parameters of the equivalent system.

By increasing stepwise the voltage $\tilde{U}_0$ at the transformer in $\Delta U = 1\ V$, the parameters P_{0set}, Q_{0set}, $P_{0\Delta U}$, and $Q_{0\Delta U}$ are obtained. Likewise, a frequency step of 10 mHz at the transformer allows for the identification of $P_{0\Delta f}$, and $Q_{0\Delta f}$. These parameters are inputs to Eqs. (7.6) through (7.7) and (7.13) through (7.16), whose solutions yield the equivalent impedance $\tilde{Z}$, the nominal voltage $\tilde{E}_{nom}$, and the equivalent droop gains. These values are summarized in Table 7.1

Table 7.1: Static parameters of the equivalent system

Parameter	Value	Units
Measurements		
S_{0set}	$21.17 - j0.845$	kVA
$S_{0set\Delta U}$	$28.61 + j2.002$	kVA
$S_{0\Delta U}$	$21.36 + j4.544$	kVA
$S_{0\Delta f}$	$22.17 - j1.915$	kVA
Equivalent parameters		
$\tilde{Z}$	$0.273 + j0.106$	Ω
$\tilde{E}_{nom}$	$227.52 - j1.0766$	V
K_{Pf}	$9.923\ 10^{-3}$	mHz/Ws
K_{PU}	$7.792\ 10^{-2}$	mV/Ws
K_{Qf}	$-3.025\ 10^{-4}$	mHz/var
K_{QU}	$1.344\ 10^{-1}$	mV/var

Note that, although the inverters were configured without coupled droops, the resulting system has values of K_{PU} and K_{Qf} different from zero. This means that, given a frequency deviation at the transformer, the LV grid responds with a change in active *and* reactive power. Although this might seem counter-intuitive,

this coupling is a natural phenomenon in LV grids, since each inverter will react to the frequency deviation by injecting only active power at its terminals, but the resistive nature of the grid and the voltage drop related to the current flow through it implies additional reactive power, which is seen at the transformer as a reaction to the frequency step. The same phenomenon couples a voltage deviation at the transformer with a phase difference at the inverters.

Having found the static parameters, the final step to derive the reduced-order model is to fit its dynamics to that of the complete system. The transfer functions of the complete system considering all ten distributed inverters has order 30, whereas the goal of the reduced-order model is to reproduce a similar behavior of only third order. Since the static parameters already guarantee that the initial and final values of the transfer functions match, the order of the equivalent system simply relates to the accuracy with which the transfer functions can be approximated.

The transfer matrix $\boldsymbol{G_{sys0}}(s)$ of the complete system is sampled at 100 logarithmically spaced frequencies between 0.1 and 100 Hz, yielding a nonlinear least-squares problem with three unknowns and 400 data points.The time constants resulting from solving the optimization problem are shown in Table 7.2.

Table 7.2: Dynamic parameters of the equivalent system

Parameter	Value	Units
$\omega_P = 1/T_P$	47.91	rad/s
$\omega_Q = 1/T_Q$	44.94	rad/s
$\omega_{Pd} = 1/T_{Pd}$	10.99	rad/s

The Bode plots of both the original and the reduced-order model are shown in Fig. 7.2. Note that the values for $\omega \to 0$ and $\omega \to \infty$ match perfectly, whereas the response in the whole frequency range is merely an approximation. Although a better fit could be achieved by increasing the order of the equivalent model, it is important to keep in mind that the time constants of the equivalent system are not directly the poles of $\boldsymbol{G_{sys0}}(s)$, but rather related to them through the static parameters of Table 7.2 on which the transfer functions depend. Hence, these three time constants cannot be directly read out of the Bode plot and must rather be found through nonlinear fitting.

The dynamic response of the active and reactive power flow into the grid to a voltage step of 1 V can be seen in Fig. 7.3, and that to a frequency step of 10 mHz in Fig. 7.4. The key-values needed to compute the inverter parameters are denoted in these figures as well.

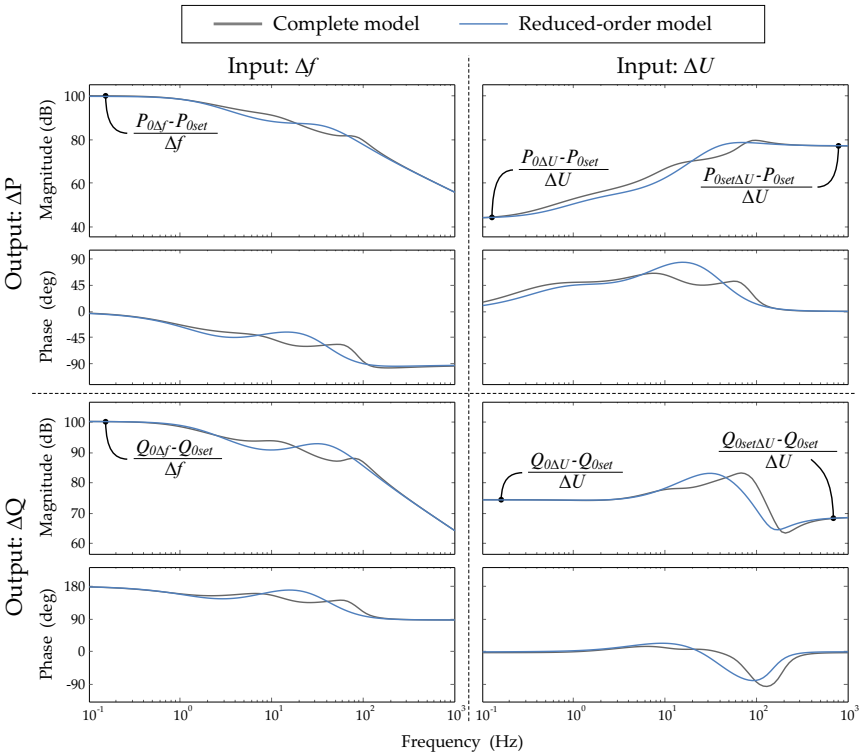

Figure 7.2: Bode plots of the original and the reduced-order model

Although the dynamic responses of the complete and the reduced-order models are not identical, a suitable fit can be achieved. The stationary values of both models are nonetheless perfectly reproduced.

7.4 ADVANTAGES OF THE NONLINEAR MODEL

The reduced-order model proposed was derived with the purpose of finding the equivalent dynamics of a LV grid with distributed generation. To do this, a model structure was followed and its parameter fit comparing the responses of the reduced-order model with those of the complete system. However, a question arises as to whether the parameters obtained, which were derived at a given linearization point and with a stiff MV grid, will perform as well at other operating points and coupled to a non-stiff grid.

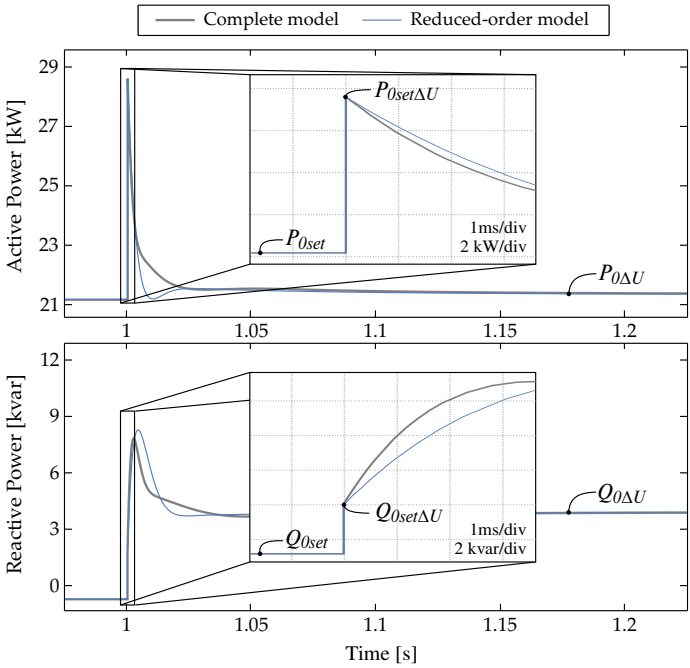

Figure 7.3: Response of the active and reactive power flow to a voltage step

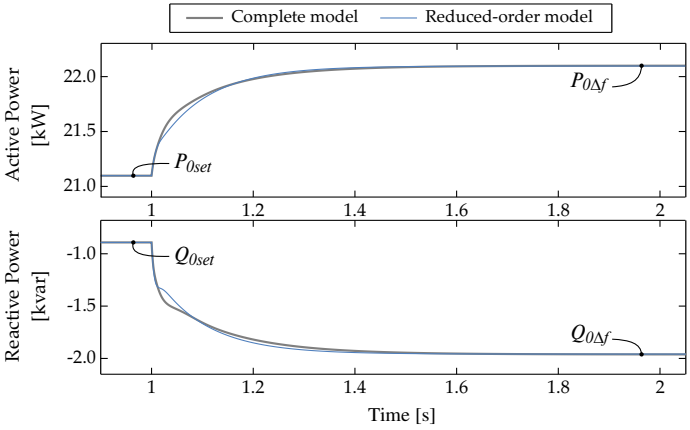

Figure 7.4: Response of the active and reactive power flow to a frequency step

Regarding the operating point, the chosen model structure has a further advantage over traditional model-order reduction tools, since the voltage $\tilde{E}_{nom}$ at which the

system is linearized is one of the parameters of the equivalent model. With this in mind, the equivalent voltage $\tilde{E}_{nom}$ could be adapted to reproduce changes on the system without having to modify the remaining parameters.

For instance, if the total load was cut to a half and the inverters continued to provide the same amount of active and reactive power, the MV grid would only have to provide $5.23-0.86j$ kVA to maintain the same voltage at the transformer. With this new nominal value, and recalling Eq. (7.6), a new voltage $\tilde{E}_{nom} = 229.2 - 10.04j$ V for the equivalent inverter can be computed.

The complete process described in Section 7.3 could be repeated for the modified system with half as many loads, but repeated experiments for different systems show that the equivalent impedance, droop gains, and time constants barely change. Adapting the linearization voltage $\tilde{E}_{nom}$ is therefore enough to introduce the modifications into the equivalent model.

Another important aspect is the dynamic interaction with the MV grid. The voltage and frequency steps simulated on the stiff grid are not realistic, but rather chosen as suitable inputs when identifying the system. Instead of such arbitrary steps, a real-world grid faces constantly load steps of various amplitude. However, if the MV grid was further considered as an ideal voltage source, all loads parallel to it would not trigger any interaction with the distributed inverters.

To better study these interactions, the dynamics of the MV grid could also be simulated, replacing the ideal voltage source with an equivalent rotating generator and a series impedance. To further intensify the coupling of the medium and the LV grid, the active and reactive power droops of the rotating generator are chosen of the same order as those of the equivalent inverter, with $k_P = 0.01$ mHz/kW and $k_Q = 0.1$ mV/kvar. This is of course not realistic in a scenario in which a small residential LV grid is connected to an urban MV grid, which itself is supplied by a larger system of interconnected higher-voltage grids, because much more load-following energy is provided by the higher voltage levels than from the LV grid. However, if most load-following energy is provided by the MV grid, it acts as an almost ideal voltage source, omitting any interaction with the dynamics of the LV grid. Choosing similar droop gains allows to better study the equivalent dynamics of the LV grid with distributed generation and to analyze the limits of the proposed approach.

The time constants of the rotating generator are set to 1 Hz, which is about the average frequency usually present in MV grids. Finally, the series impedance is chosen as the benchmark value of $\tilde{Z}_{series} = 0.2 + 0.1j\ \Omega$, discussed in Chapter 2. A load of 5 kW and a switch are included in the LV grid, which can be seen in Fig. 7.5.

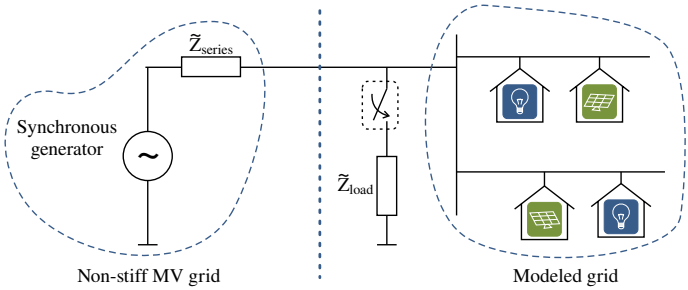

Figure 7.5: Test system with non-stiff MV grid

This system is simulated once with the complete model of the LV grid and again with the equivalent reduced-order model. The switch is closed at $t = 1$ second. The response of the active and reactive power flowing into the LV grid is shown in Fig. 7.6.

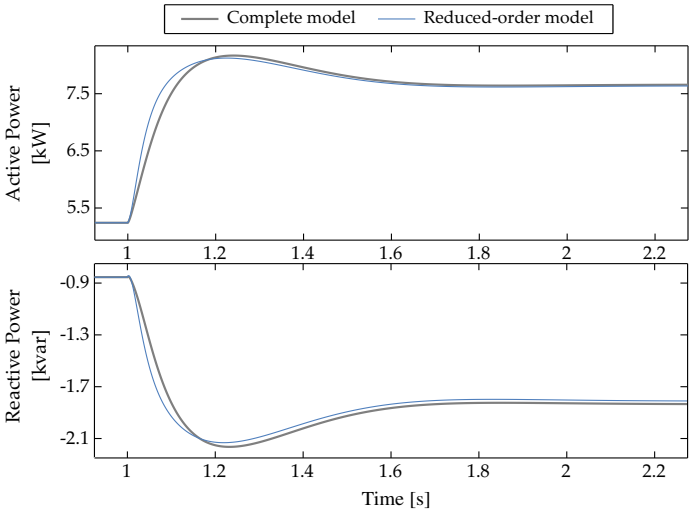

Figure 7.6: Response of the active and reactive power flow into the grid after a load step

The resulting frequency deviation caused by the load step can be seen in Fig. 7.7. The frequency of the equivalent inverter builds an average of those of the distributed inverters. The faster dynamics of the LV grid compared to the rotating generator can also be appreciated on this plot.

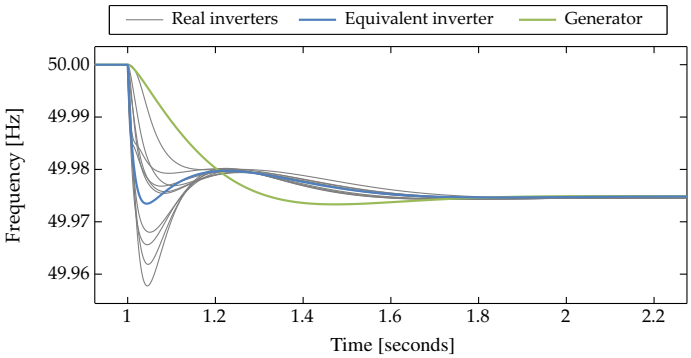

Figure 7.7: Response of the instantaneous frequency after a load step

Note that, although the parameters of the equivalent system were originally derived considering a stiff MV grid and twice as many loads, the reduced-order model reproduces the dynamics of the modified system correctly. Although some minor differences proper of such an approximation arise, the reduced-order model can be used to accurately replicate the dynamics of a LV grid with distributed generation without having to model each power source in detail. This sort of macro-model allows for the feasible integration of the dynamics of the LV grid into MV models, which will be necessary in a future power system with large amounts of distributed generation at the LV level.

8

EXPERIMENTAL RESULTS

In order to test the feasibility of the theoretical analysis and the simulations presented, a small-scale experimental setup was used. These tests are based on droop-controlled voltage source inverters which are set up in different configurations to test the response of a single inverter and of several inverters in a distributed system.

8.1 VOLTAGE SOURCE INVERTER

Each VSI consists of a Danfoss FC302 2.2 kVA three-phase three-legs power module, together with an output three-phase LCL filter and voltage and current sensors. An independent DC power supply is used to provide energy to the DC bus with the voltage U_{DC}. The schematic diagram of this voltage source inverter can be seen in Fig. 8.1

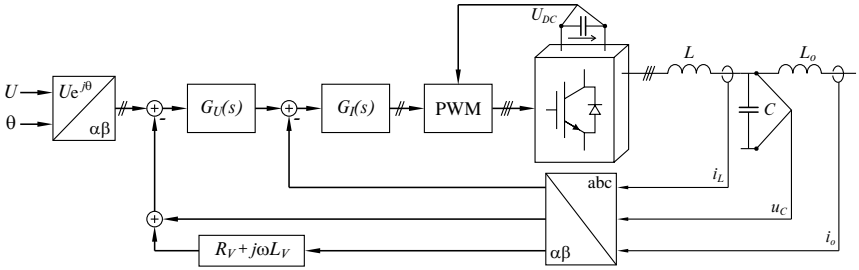

Figure 8.1: Schematic diagram of a voltage source inverter

The inverter is controlled implementing two cascaded loops. The internal loop consists of a proportional-resonant controller $G_I(s)$ that regulates the inductor current i_L. The controller has the form

$$G_I(s) = k_{pI} + \frac{k_{rI}s}{s^2 + \omega_0^2}, \tag{8.1}$$

where k_{pI} and k_{rI} are the proportional and resonant controller gains and ω_0 is the nominal frequency of the grid[1]. The PWM unit generates the switching signals that command each leg of the power module. The DC voltage is measured and used in the generation of the PWM signals to compensate for possible ripple on the DC bus.

The outer loop consists of a controller $G_U(s)$ that regulates the voltage u_C on the capacitors. Analogously to the current controller, the voltage controller is implemented as a proportional-resonant controller of the form

$$G_U(s) = k_{pU} + \frac{k_{rU}s}{s^2 + \omega_0^2}. \tag{8.2}$$

A virtual impedance loop is included in the voltage control loop, which helps tune the output impedance of the inverter. Note that the control loops of the inverter take place in the stationary two-phase reference frame $\alpha\beta$, while transformations must be done between the natural reference frame (abc) and the equivalent one-phase rotating system ($Ue^{j\theta}$).

The choice of parameters for the internal voltage and current controllers was made based on [21] followed by additional empirical fine-tuning. Details on the inverter parameters used for the experimental setup are shown on Table 8.1.

Provided that these internal control loops are tuned with enough bandwidth, the inverter behaves as an equivalent voltage source with magnitude U, phase θ, and output impedance $\tilde{Z}_o = R_v + j\omega(L_v + L_o)$. However, the concept of bandwidth on such a system is not trivially defined, since the inverter operates at 50 Hz in steady state and the input U is modulated nonlinearly by the phase θ. The proportional-resonant controller assures no error in steady state, i.e. for an input of constant amplitude U and a phase θ that rotates at a constant rate of 50 Hz, but the behavior of the system for time-varying inputs has to be further studied in order to guarantee that the voltage source inverter effectively operates approximately as an ideal voltage source with negligible lag.

1 Some authors use the reference frequency from the droop controller instead, which yields a better response over a wider frequency range.

Table 8.1: Parameters of the voltage source inverter

Parameter	Symbol	Value	Units
Power Stage			
Nominal grid effective voltage	U_g	400	V
Nominal grid frequency	f	50	Hz
Output inductance	L_o	1.8	mH
Filter inductance	L	1.8	mH
Filter capacitance (Δ)	C	27 (3×9)	μF
DC Voltage	U_{DC}	650	V
Switching Frequency	f_{SW}	20	kHz
Voltage/Current PR Control			
Voltage loop PR	$k_{pU},\ k_{rU}$	0.35, 150	-
Current loop PR	$k_{pI},\ k_{rI}$	1, 1000	-

To better illustrate the functioning of the internal control loops, the Bode plot of the closed-loop transfer function from u_{ref} to u_C is shown in Fig. 8.2. From this plot it is easy to see that the inverter responds with a unity gain and without phase lag for an input with a constant frequency of 50 Hz, but it is not immediately clear how the inverter will respond to a change in amplitude or phase of the input.

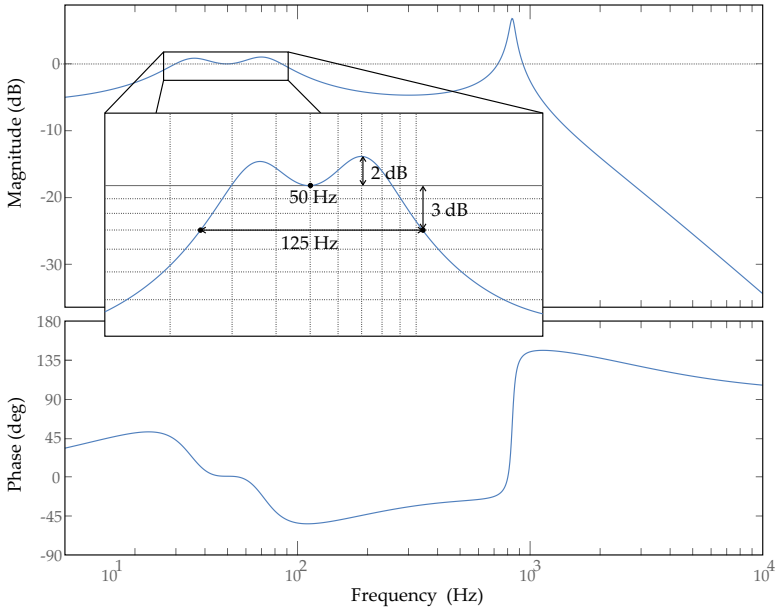

Figure 8.2: Bode plot of the voltage source inverter

Even though an approximate 3 dB bandwidth of 125 Hz centered at 50 Hz can be read out of the Bode plot, the equivalent bandwidth of the system in the rotating reference frame is about one half of it. This can be observed by studying the response of the inverter to a step input on the voltage amplitude U, which is shown in Fig. 8.3. Although highly nonlinear due to the transformation between stationary and rotating reference frames, this step response can be approximated by means of a least square estimation to that of a first-order system, which is also shown in Fig. 8.3. The equivalent cutoff frequency was found to be of 64.3 Hz.

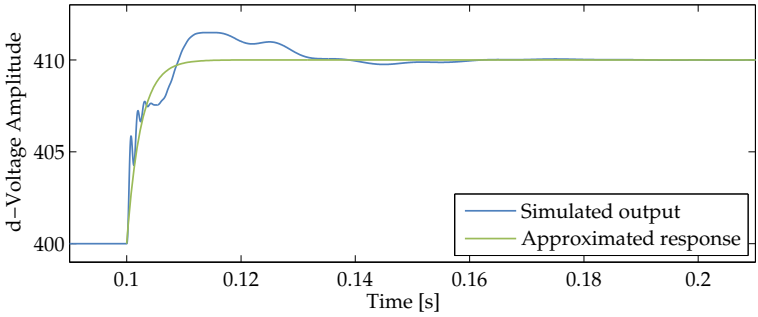

Figure 8.3: Simulated step response and estimated equivalent first-order response

From this analysis it follows that the dynamic response of the inverter with the chosen parameters can be in fact disregarded, since the lag introduced by the internal control loops is negligible compared to the slower dynamics of the droop controller.

The analysis and tuning of the closed-loop dynamics of the internal control loops of a voltage source inverter can be investigated in depth and is itself a topic of great complexity and constant research, although it shall not be further approached in this work. A comprehensive overview on proportional-resonant control theory followed by a number of practical cases can be found in [85]. An extension of this scheme to control harmonics is shown in [86], while further damping on the resonance of the LCL output filter is introduced in [87]. An analysis and comparison of DQ frame and resonant controllers is presented in [88], while alternative, more complicated nonlinear control schemes can be found for instance in [89].

8.2 SINGLE INVERTER

The design methods of the improved droop controller for a single inverter proposed in Chapter 4 can be validated by building a simple experimental setup as shown in Fig. 8.4, which consists of two VSIs and a dSPACE1006 which implements the control algorithms. The first inverter is configured as a programmable voltage source with adjustable amplitude and frequency, which functions as a grid simulator [90]. The second inverter implements the improved droop controller. In this way, the first inverter acts as a stiff grid, which allows for the study of the response of the other inverter without having to cope with external sources of error present on a real grid such as power fluctuations and deviations from nominal values.

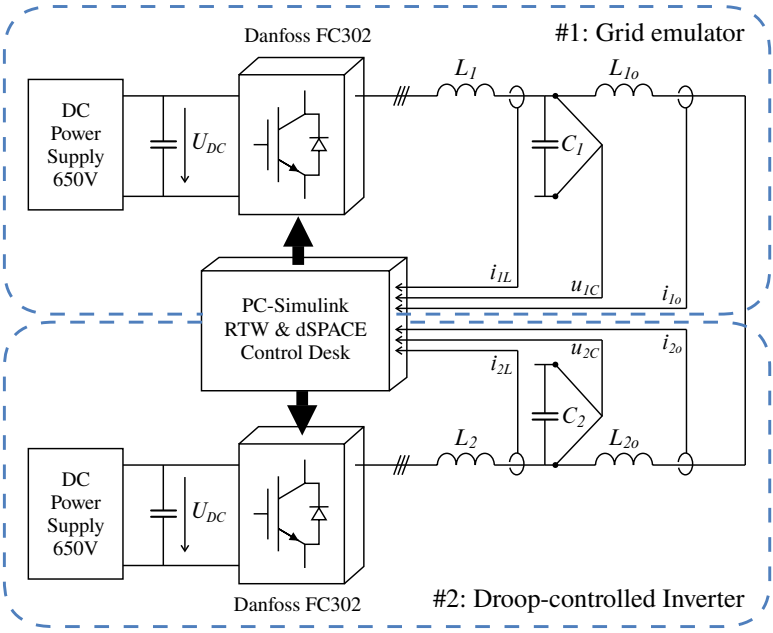

Figure 8.4: Schematic diagram of the experimental setup

The experimental setup was configured with the parameters described in Table 8.2, while different values of dynamic droop gains k_{Pd} were tested. An equivalent inverter-to-grid inductance is obtained by tuning the virtual output impedance of both inverters. Details on this method can be found for instance in [36, 91]. As a result, the electrical equivalent of Fig. 8.5 is obtained.

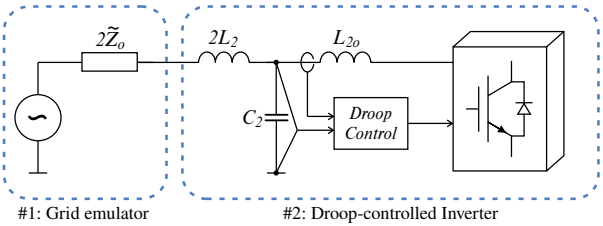

Figure 8.5: Electrical equivalent of the experimental setup

Table 8.2: Parameters used for the test

Parameter	Symbol	Value	Units
Virtual output impedance			
Virtual output resistance	R_o	0.5	Ω
Virtual output inductance	L_o	2	mH
Droop Control (only at inverter 2)			
Power filters	$\omega_{fP} = \omega_{fQ}$	2π	rad/s
Active power droop	k_P	0.25	rad/kWs
Reactive power droop	k_Q	0.01	V/var

Table 8.3 shows the dynamic droop gains in mrad/kW and the resulting poles of the system obtained with the three methods proposed, as well as the poles for the case without dynamic gain. The equivalent zero ω_d that results from the improved droop controller is shown as well. Note that the design based on root locus yields all real poles, which is achieved by increasing the gain until both complex poles are shifted to the break-in point present in the root locus. The other two methods preserve the pair of complex poles but with improved damping.

Table 8.3: Resulting poles for different dynamic droop gains

Open-loop $k_{Pd} = 0$ $\omega_d = \infty$	Root locus $k_{Pd} = 70.5$ $\omega_d = 3.55$	Bode plot $k_{Pd} = 25.9$ $\omega_d = 9.65$	Impedance $k_{Pd} = 18.1$ $\omega_d = 13.82$
-628.5	-602.7	-619.3	-622.1
$-2.72 + 9.26j$	-21.81	$-8.21 + 6.27j$	$-6.32 + 7.69j$
$-2.72 - 9.26j$	-21.81	$-8.21 - 6.27j$	$-6.32 - 7.69j$
-15.66	-3.203	-13.89	-14.86

To better visualize the dynamics of the droop-controlled inverter in each case, a frequency drop of 50 mHz is introduced with the other inverter. The active and

reactive power for the different dynamic droop gains shown in Table 8.3 can be seen in Fig. 8.6. Although such a step in frequency is unlikely to be present in practice, these experimental results help illustrate the transient response of the inverter and validate the feasibility of the resulting dynamic droop gains, as well as the accuracy of the model.

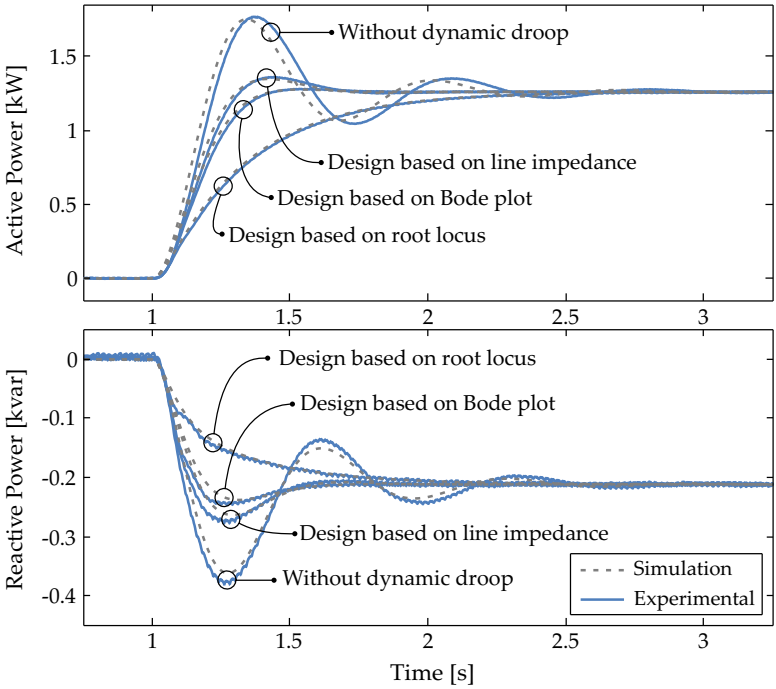

Figure 8.6: Active and reactive power response of the inverter to a frequency step of the grid emulator with different values of k_{Pd}

As already seen in the theoretical analysis, the design based on line impedance damps the initial oscillatory behavior of the inverter without improved droop, yet the step response stays underdamped. The response obtained with the design based on Bode plot seems fairly damped, although a small overshoot can be noticed. On the other hand, the droop gain based on root locus, which critically damps both complex poles, yields a transient response which might seem unnecessary slow and overdamped. This is caused by the dominant effect of the slowest pole of the system, since increasing the gain needed to shift both complex poles to the real axis also shifts the slowest pole to the right, making it slower.

The consistency of the simulation results with the measurements seen in Fig. 8.6 furthers validates the modeling approach.

8.3 THREE INVERTERS

Experimental results for the design methods for a system with multiple inverters introduced in Chapter 6 were obtained by considering a three-inverter scenario. An experimental setup was built according to this configuration as shown in Fig. 8.7, which consists of three voltage source inverters and a dSPACE1006 which implements the control algorithms. Each inverter is controlled with cascaded voltage and current loops as discussed before, implementing the parameters of Table 8.1.

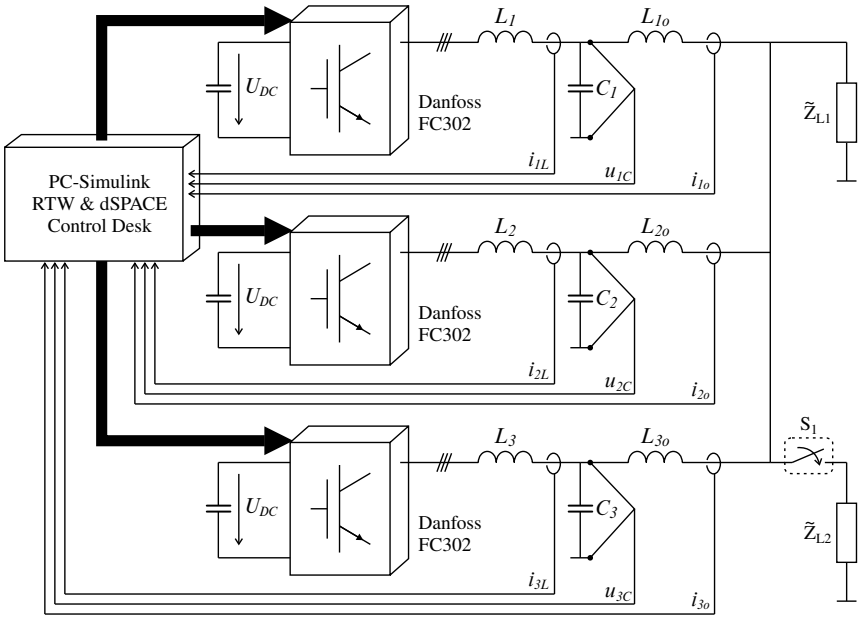

Figure 8.7: Schematic diagram of the experimental setup

The virtual output impedance $\tilde{Z}_O$ of the inverters is used to mimic an equivalent grid impedance. Each output impedance was chosen deliberately different from the others to better represent a real system with distributed generation. As a result, the electrical equivalent of Fig. 8.8 is obtained, which reproduces a MG in autonomous operation.

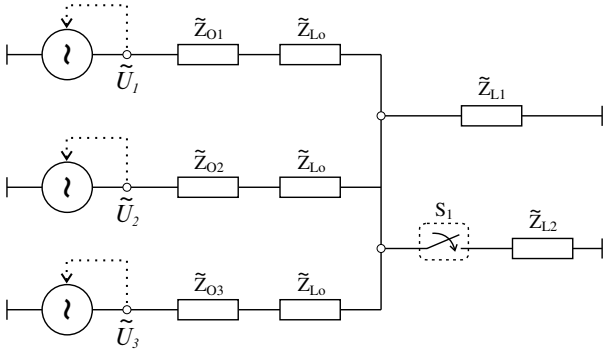

Figure 8.8: Electrical equivalent of the experimental setup

The experimental setup was configured with the parameters described in Table 8.4, while two set of dynamic droop gains derived by means of the design methods introduced in Chapter 6 were tested.

Table 8.4: Parameters used for the test

Parameter	Symbol	Value	Units
Virtual output impedance			
Virtual output resistance	R_{O_1}	0.25	Ω
	R_{O_2}	0.5	Ω
	R_{O_3}	1.0	Ω
Virtual output inductance	L_{O_1}	1	mH
	L_{O_2}	2	mH
	L_{O_3}	4	mH
Droop Control			
Power filters	$\omega_{fP} = \omega_{fQ}$	2π	rad/s
Active power droop	k_P	0.1	rad/kWs
Reactive power droop	k_Q	0.01	V/var
Load			
Resistive Load	$\tilde{Z}_{L_1} = \tilde{Z}_{L_2}$	230	Ω

8.4 DESIGN WITH METHOD A

The search for an optimal set of dynamic droop gains is performed by running the optimization algorithm of Method A. A trivial nonzero initial condition $\boldsymbol{k_{Pd}} = \mathbf{1} \cdot 10^{-8}$ is used to avoid singularities in the numerical solution. As a result, the

optimization increases iteratively the value of each dynamic droop gain and an optimal controller is found after 29 iterations. The resulting vector of dynamic droop gains is:

$$\boldsymbol{k_{Pd}} = (67.1 \quad 104.2 \quad 81.7)\,, \tag{8.3}$$

and the frequencies of the equivalent zeros of the improved droop controllers are

$$\boldsymbol{\omega_d} = (1.49 \quad 0.96 \quad 1.22)\,. \tag{8.4}$$

8.5 DESIGN WITH METHOD B

The dynamic droop gains computed with method B are related to the dynamics of the system without dynamic droop and to information of the coupling obtained with the RGA matrix. The matrix $\boldsymbol{A_{sys}}$ possess only two pairs of complex eigenvalues, which yields a mean frequency of

$$\omega_m = \sqrt{7.837\ .\ 5.658} = 6.659 \text{ rad/s}. \tag{8.5}$$

The RGA analysis yields the matrix

$$RGA_{1,1} = \begin{pmatrix} 0.3005 & 0.1144 & 0.0437 \\ 0.1075 & 0.3072 & 0.0403 \\ 0.1084 & 0.0806 & 0.3898 \end{pmatrix}, \tag{8.6}$$

which results in the dynamic droop gains

$$\boldsymbol{k_{Pd}} = (50.2 \quad 48.6 \quad 38.6)\,, \tag{8.7}$$

and the frequencies of the equivalent zeros of the improved droop controllers

$$\boldsymbol{\omega_d} = (4.98 \quad 5.14 \quad 6.48)\,. \tag{8.8}$$

8.6 COMPARISON OF BOTH METHODS

The closed-loop dynamics of the system with the improved droop gains can be evaluated by computing the eigenvalues of the matrix $\boldsymbol{A^*_{sys}}$. Table 8.5 shows the resulting values for the system using the gains obtained with both methods. The eigenvalues of the system without dynamic droop gains are shown as well for reference.

Table 8.5: Eigenvalues of the system in autonomous operation with and without dynamic droop gains

$\boldsymbol{k_{Pd}} = \mathbf{0}$	Method A	Method B
$-2.84 + 4.89j$	-21.93	$-14.76 + 5.49j$
$-2.84 - 4.89j$	-21.93	$-14.76 - 5.49j$
$-2.85 + 7.30j$	-46.79	$-25.81 + 8.03j$
$-2.85 - 7.30j$	-24.77	$-25.81 - 8.03j$
-6.28	-6.28	-6.28
-6.28	-6.28	-6.28
-13.77	-0.92	-1.76
-20.20	-1.19	-1.83

As expected, the poles obtained with method A are all real and stable. The second pair of complex poles shifts to the real axis, while the first pair results critically damped. Two of the poles obtained from the power filter with a cutoff frequency of 1 Hz (6.28 rad/s) barely move, while the remaining poles slide along the real axis. The poles obtained with method B are not as well damped, which was expected. However, the damping of both pairs of complex poles is as well improved with this method, while all other poles stay on the real axis.

To visualize these dynamic responses, the experimental setup is excited by closing the switch S_1 at $t = 1$ s. Before closing the switch, the inverters are configured with offsets of 130, 230 and 300 W and -30, 0, and 30 var respectively to provide the load $\tilde{Z}_{L_1}$ and ensure nominal voltage and frequency. Fig. 8.9 shows the active and reactive power response obtained experimentally. Simulation results are also shown with superimposed faded lines.

From these measurements it can be noted that the response of the inverters becomes more sensible to high frequency perturbations as the damping increases, as it was expecting from increasing the derivative term on the controller. This can be better illustrated by observing the output currents of the inverters, which are shown in Fig. 8.10. The increase in current after the load step can be noticed at $t = 1$ s, while the zoomed in area shows in detail the distortion for each case.

To better quantify this effect, the total harmonic distortion was computed for each phase in each case. The resulting values are shown in Table 8.6 together with the Euclidean norm of the THD of all three phases.

On this account, care should be taken when tuning the dynamic droop gains, since overdamping the system makes the inverters less robust against non-modeled high frequency dynamics. To better handle this, harmonic controllers can be used

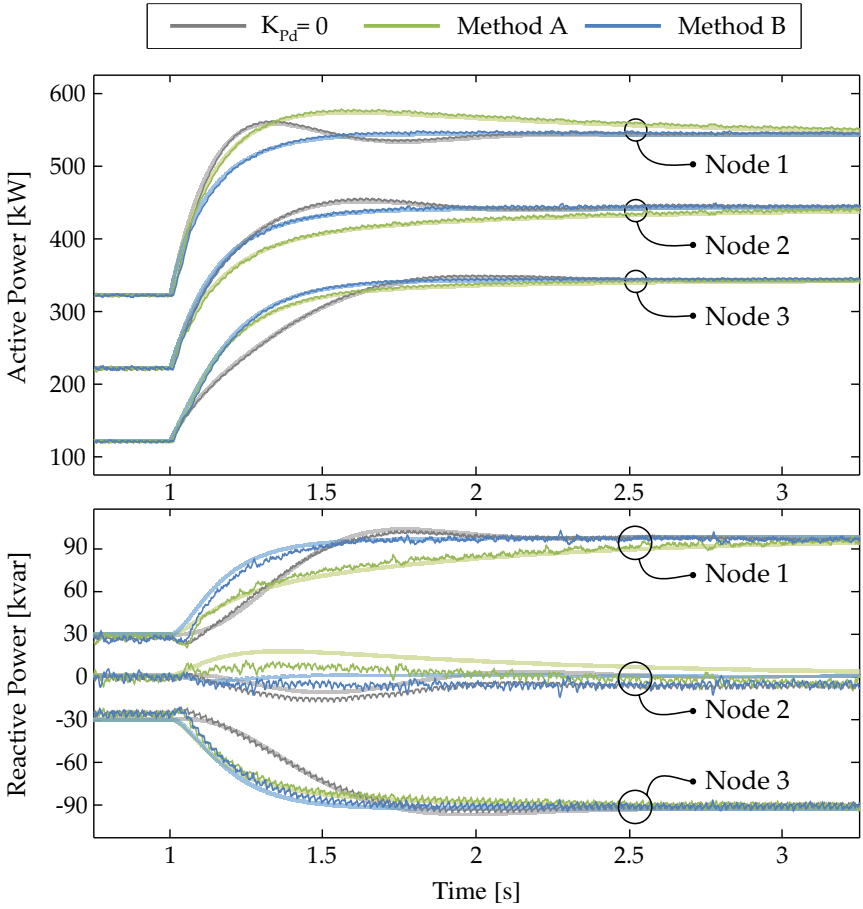

Figure 8.9: Active and reactive power response of the inverter to a load step with different values of $\boldsymbol{k_{Pd}}$

Table 8.6: Total harmonic distortion (THD) of the output current. Values in %

	THD_a	THD_b	THD_c	$\|\|THD\|\|$
$\boldsymbol{k_{Pd}} = \mathbf{0}$	14.73	15.87	16.37	15.67
Method A	18.38	19.63	19.67	19.24
Method B	17.42	18.66	18.89	18.33

when implementing the voltage and current loops, which allows for better sharing of unbalanced and nonlinear loads [92, 93]. However, the contribution of this

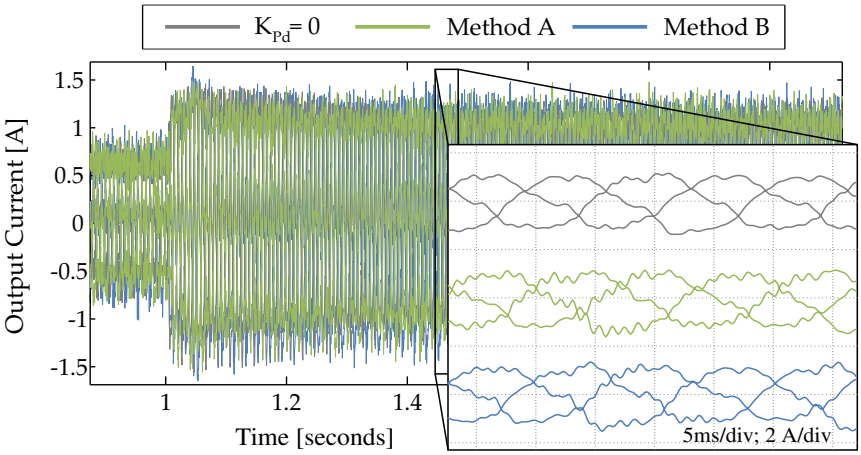

Figure 8.10: Output current (abc) with different values of $\boldsymbol{k_{Pd}}$

work has focused merely on the slower dynamics due to the power filters and the droop controller, which shall be studied independently.

9

CONCLUSIONS

This thesis studied the dynamic behavior of a LV grid with DG and presented systematical methods to stabilize and better damp the system. The analysis followed a modular approach, going from the simplified models of a power grid and a single power generator to the complex interaction of several generating units distributed in a real-world grid.

The main contributions of this work are many-fold. On the first hand, a compact model for the stability analysis of distributed generation was derived. The resulting nonlinear model can be represented in a simple block diagram employing complex vectors, while disturbances can be simulated either as load steps or as voltage or frequency changes at a given node of the grid. The stability of a LV grid was studied and simulated with the nonlinear model proposed, which reproduces the behavior of the grid in a way that is simple enough in order to reduce computational costs, yet allows for the analysis of the fundamental dynamic interactions between distributed power inverters.

The dynamics of energy flow through the power lines was studied with the concept of dynamic phasors, extending the admittance parameter with a complex pole. It was also shown that the related eigenvalues depend only on the resistive to inductive ratio of the line, while the eigenfrequency is always higher than 50 Hz. This justifies that the power interactions between inverters can be further studied without considering phasor dynamics, as long as the resulting eigenfrequencies lie in the single-digit Hz range.

The implementation of a decentralized controller in the form of improved droop gains allowed for a better damping of the system and even the stabilization in case of instability. Different tuning methods for a single and several inverters were presented, which enhance the dynamics of the system.

A reduced-order model reproduced the dynamic response of the aggregated LV grid as seen from the MV grid in a simplified manner, which enables the hierarchical integration into higher-level simulations.

The proposed models and controllers were implemented in MATLAB/Simulink under different validation scenarios. The results of these simulations were compared with more complex models and experimental results found in the literature.

Finally, measurements were conducted on a small-scale laboratory setup, which further validated experimentally the approaches presented in this work.

9.1 FURTHER RESEARCH AND OUTLOOK

The droop-controlled voltage source inverter is nowadays the inverter structure mostly employed in MGs and some research VPPs. However, some not-so-popular alternatives to this scheme also exist. For instance, a current source controller could also be modified to implement power droops. This scenario should be seriously analyzed in the future, since such controllers must implement a PLL for the synchronization to the grid and inverse power droops as an outer loop to provide load-following energy, which plays a decisive role in the dynamics of the system. Although a single such inverter can be configured to be stable, the stability of both control loops in a system with several distributed inverters should be further studied, and eventually a damping approach similar to the improved droop controller presented in this work should be performed.

When considering the real-world large-scale implementation of the inverters studied in this work, two critical aspects must be further analyzed. On the first hand, asymmetrical systems must be taken into account, particularly since it is not infrequent to find unbalanced loads and single-phase power inverter in LV grids. A second important issue is the existence of constant-power and nonlinear loads, which are rather common in the LV level and have a destabilizing effect on the system.

Further possibilities with the RGA should also be investigated. For instance, the matrices $\boldsymbol{K_P}$, $\boldsymbol{K_Q}$, and $\boldsymbol{K_{Pd}}$ were considered diagonal throughout this work, under the premise that each inverter should only operate autonomously, hence avoiding any kind of real-time comunication. However, the non-zero elements of these matrices could be used to couple the control loops of two or more inverters, in case that this was critical to the stability of the system. The RGA matrix could further aid in the search of critical control signals, identifying a minimal set of inverters that should be communicated with each other in order to guarantee stability.

Last but not least, the incorporation of stability analysis and systematic controller design must be intensively promoted in the area of energy management systems. Only by considering both technical and economical aspects together can we accomplish a green, reliable, and stable power system of the future.

I

BENCHMARK GRID

A real-world low-voltage grid has been available for studies during the project *Smart Nord* [30] and has been used as a benchmark grid in this thesis. The system consists of 71 power lines that connect 71 nodes forming a LV power grid of a German urban area.

The length and type of each line is well known, which is shown in Table I.1. Each node has a number from 1 to 71 assigned to it, while each line connecting any two nodes is documented. The transformer which interfaces with the MV grid is related to node number 1. Nodes number 2 to 11 are bus-bars, while the remaining 60 are connections to buildings. The system is three-phase and is considered balanced, hence equivalent single-phase resistances and reactances are considered.

Table I.1: Details of a real-world low-voltage grid

From	To	Type of cable	R $[m\Omega]$	X $[m\Omega]$	Iso $[A]$	Len [m]
2	54	NAYY 4*025/0.4	4.80	0.35	102	4.0
54	55	NAYY 4*025/0.4	93.60	6.86	102	78.0
34	35	NAYY 4*025/0.4	52.80	3.87	102	44.0
4	14	NAYY 4*035/0.4	30.38	2.98	122	35.0
4	15	NAYY 4*035/0.4	39.06	3.82	122	45.0
16	13	NAYY 4*035/0.4	30.38	2.98	122	35.0
16	17	NAYY 4*035/0.4	4.34	0.42	122	5.0
45	46	NAYY 4*035/0.4	22.57	2.21	122	26.0
45	47	NAYY 4*035/0.4	22.57	2.21	122	26.0
10	70	NAYY 4*035/0.4	17.01	1.67	122	19.6
10	71	NAYY 4*035/0.4	98.95	9.69	122	114.0
3	33	NAYY 4*070/0.4	28.35	5.25	179	64.0
5	52	NAYY 4*070/0.4	20.07	3.71	179	45.3
52	2	NAYY 4*070/0.4	15.06	2.79	179	34.0

continues on next page...

...continued from previous page

From	To	Type of cable	$R\ [m\Omega]$	$X\ [m\Omega]$	Iso $[A]$	Len [m]
28	29	NAYY 4*070/0.4	10.19	1.89	179	23.0
29	30	NAYY 4*070/0.4	14.62	2.71	179	33.0
30	31	NAYY 4*070/0.4	17.99	3.33	179	40.6
31	32	NAYY 4*070/0.4	12.58	2.33	179	28.4
33	34	NAYY 4*070/0.4	19.05	3.53	179	43.0
44	45	NAYY 4*070/0.4	65.56	12.14	179	148.0
8	48	NAYY 4*070/0.4	70.88	13.12	179	160.0
11	27	NAYY 4*070/0.4	34.73	6.43	179	78.4
27	28	NAYY 4*070/0.4	13.29	2.46	179	30.0
62	63	NAYY 4*120/0.4	2.58	0.82	245	10.2
63	64	NAYY 4*120/0.4	7.34	2.32	245	29.0
64	65	NAYY 4*120/0.4	6.93	2.19	245	27.4
65	66	NAYY 4*120/0.4	11.97	3.78	245	47.3
66	67	NAYY 4*120/0.4	5.06	1.60	245	20.0
67	68	NAYY 4*120/0.4	3.67	1.16	245	14.5
68	69	NAYY 4*120/0.4	9.36	2.96	245	37.0
36	37	NAYY 4*120/0.4	4.73	1.50	245	18.7
37	38	NAYY 4*120/0.4	13.66	4.32	245	54.0
38	39	NAYY 4*120/0.4	15.46	4.89	245	61.1
39	40	NAYY 4*120/0.4	16.19	5.12	245	64.0
40	41	NAYY 4*120/0.4	8.35	2.64	245	33.0
41	42	NAYY 4*120/0.4	1.52	0.48	245	6.0
42	43	NAYY 4*120/0.4	2.78	0.88	245	11.0
43	8	NAYY 4*120/0.4	2.53	0.80	245	10.0
8	44	NAYY 4*120/0.4	2.83	0.90	245	11.2
9	19	NAYY 4*120/0.4	4.05	1.28	245	16.0
11	36	NAYY 4*120/0.4	7.34	2.32	245	29.0
2	53	NAYY 4*150/0.4	9.89	3.84	275	48.0
5	49	NAYY 4*150/0.4	7.05	2.74	275	34.2
18	9	NAYY 4*150/0.4	21.63	8.40	275	105.0
49	50	NAYY 4*150/0.4	5.97	2.32	275	29.0
50	51	NAYY 4*150/0.4	9.56	3.71	275	46.4
69	10	NAYY 4*150/0.4	130.40	50.64	275	633.0
7	1	NAYY 4*150/0.4	15.66	6.08	275	76.0
1	5	NAYY 4*150/0.4	34.61	13.44	275	168.0
20	21	NAYY 4*185/0.4	2.05	1.00	313	12.5
21	22	NAYY 4*185/0.4	5.77	2.82	313	35.2
16	6	NAYY 4*185/0.4	4.43	2.16	313	27.0

continues on next page...

...continued from previous page

From	To	Type of cable	$R\ [m\Omega]$	$X\ [m\Omega]$	Iso $[A]$	Len [m]
22	11	NAYY 4*185/0.4	10.99	5.36	313	67.0
9	20	NAYY 4*185/0.4	20.66	10.08	313	126.0
6	7	NAYY 4*185/0.4	1.69	0.82	313	10.3
7	4	NAYY 4*185/0.4	6.89	3.36	313	42.0
23	6	NAYY 4*185/0.4	18.04	8.80	313	110.0
23	24	NAYY 4*185/0.4	7.95	3.88	313	48.5
24	25	NAYY 4*185/0.4	6.40	3.12	313	39.0
25	26	NAYY 4*185/0.4	3.00	1.46	313	18.3
26	11	NAYY 4*185/0.4	3.61	1.76	313	22.0
3	56	NAYY 4*240/0.4	3.25	2.05	364	26.0
12	3	NAYY 4*240/0.4	5.25	3.32	364	42.0
56	57	NAYY 4*240/0.4	7.25	4.58	364	58.0
57	58	NAYY 4*240/0.4	4.38	2.77	364	35.0
58	59	NAYY 4*240/0.4	1.79	1.13	364	14.3
59	60	NAYY 4*240/0.4	2.13	1.34	364	17.0
60	61	NAYY 4*240/0.4	5.66	3.58	364	45.3
61	9	NAYY 4*240/0.4	17.13	10.82	364	137.0
1	12	Two in parallel	22.70	10.43	275	131.0
1	62	Two in parallel	33.48	12.40	245	155.0

Out of this data, it is possible to build a graph representation of the system as seen in Fig. I.1, which shows the topology of this grid. Note that the resulting disposition of nodes in the graph is not necessarily related to the real geographical location of the nodes. To better visualize the system, the transformer node is denoted in gray and the bus-bars in green. All other nodes are related to buildings.

Information about the consumption of energy in this benchmark grid has been as well available. The loads at nodes 12 to 71 were registered during the whole year 2009 at an interval of 15 minutes, yielding over 35000 data-points for each of these 60 nodes. The annual load mean of each node is depicted in Table I.2. Intra-day variations of the load were as well considered in this thesis, but have to be left out of this appendix for matter of space.

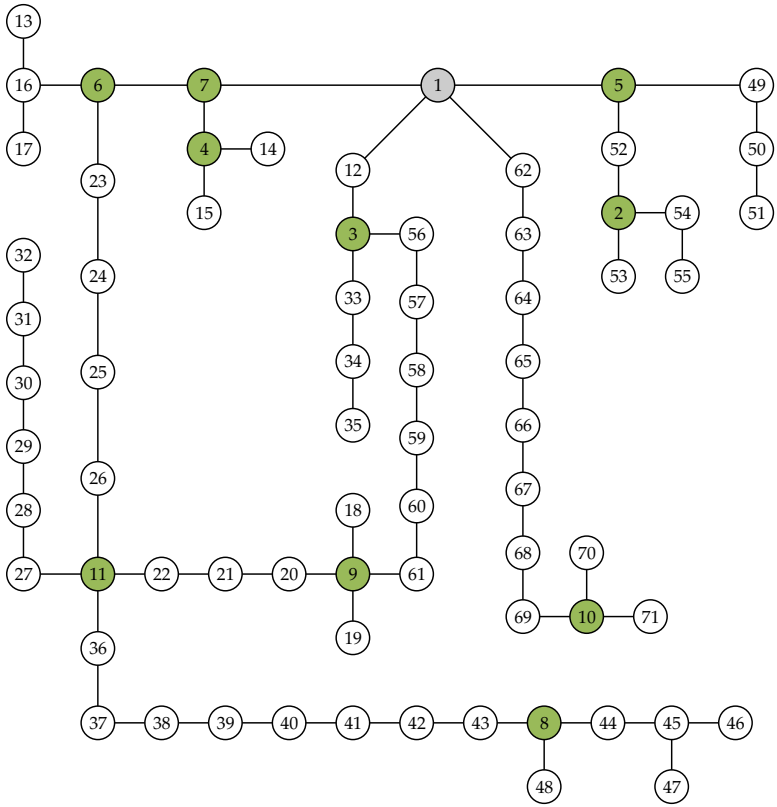

Figure I.1: Graph representation of the benchmark low-voltage grid

Table I.2: Annual mean load at each node

Node	Load [W]	Node	Load [W]	Node	Load [W]
12	283.81	32	275.67	52	1055.04
13	247.24	33	391.73	53	900.54
14	353.27	34	252.88	54	1338.99
15	281.62	35	315.10	55	1334.15
16	304.18	36	332.43	56	243.47
17	952.96	37	348.70	57	362.03
18	765.11	38	355.72	58	319.97
19	811.06	39	305.46	59	1584.70
20	833.76	40	274.73	60	380.12
21	990.87	41	385.84	61	278.03
22	295.45	42	264.96	62	868.42
23	376.32	43	365.72	63	516.53
24	398.44	44	313.58	64	572.90
25	248.78	45	292.84	65	473.60
26	263.62	46	279.90	66	491.72
27	271.54	47	303.94	67	454.60
28	380.28	48	316.03	68	516.53
29	244.66	49	792.69	69	772.43
30	279.58	50	960.39	70	819.12
31	255.10	51	1040.52	71	787.17

II

ASYMPTOTE OF THE NYQUIST PLOT OF A SYSTEM WITH A POLE AT THE ORIGIN

Let the transfer function of a linear system be given by:

$$G(s) = \frac{k}{s} \frac{\prod_{i=1}^{q}(s - s_{z_i})}{\prod_{i=1}^{n}(s - s_{p_i})} \tag{II.1}$$

Such a system has a single pole at the origin, n non-zero poles, and q non-zero zeros, with $q < n$. The Nyquist plot of this transfer function for an arbitrary set of parameters can be seen in Fig. II.1.

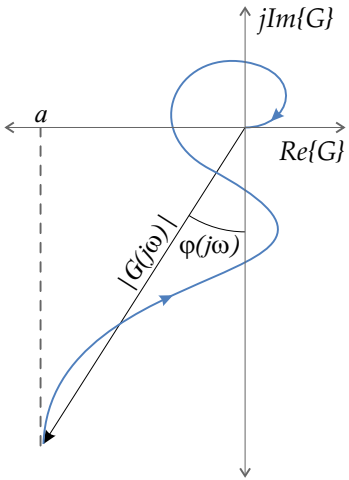

Figure II.1: Nyquist plot with asymptote

Although the behavior of the system for higher frequencies and how the curve approaches the origin is at this point of little interest, the existence of a verti-

cal asymptote for lower frequencies deserves further study. The distance to the imaginary axis is described by the limit

$$a = \lim_{\omega \to 0} Re\{G(j\omega)\}, \tag{II.2}$$

which can as well be expressed as

$$a = \lim_{\omega \to 0} |G(j\omega)| \sin \varphi(j\omega), \tag{II.3}$$

with

$$\varphi(j\omega) = \sum_{i=1}^{q} \tan^{-1}\left(\frac{\omega - Im\{s_{z_i}\}}{-Re\{s_{z_i}\}}\right) - \sum_{i=1}^{n} \tan^{-1}\left(\frac{\omega - Im\{s_{p_i}\}}{-Re\{s_{p_i}\}}\right) + \pi(q^- - n^-) \tag{II.4}$$

The term $\pi(q^- - n^-)$ accounts for additional rotations of $180°$, where q^- and n^- are the amounts of zeros and poles in the right half-plane respectively. This term is necessary since the range of the arctangent function is limited to values between $\pi/2$ and $-\pi/2$. The same could be achieved considering the two-argument arctangent function, which otherwise complicates the mathematical analysis that follows, since its limit for $\omega \to 0$ is not univocally defined.

Considering complex conjugate pole pairs and making use of trigonometric properties, the following identity holds [94]:

$$\sum_{i=1}^{n} \tan^{-1}\left(\frac{\omega - Im\{s_{p_i}\}}{-Re\{s_{p_i}\}}\right) = \sum_{i=1}^{q} \tan^{-1}\left(\frac{-\omega}{s_{p_i}}\right) \tag{II.5}$$

The same is valid for the argument of the complex zeros of the system.

With this in mind, and replacing Eqs. (II.1) and (II.4) into Eq. (II.3), it results

$$a = \lim_{\omega \to 0} \frac{k}{\omega} \frac{\prod_{i=1}^{q} |s_{z_i}|}{\prod_{i=1}^{n} |s_{p_i}|} \sin\left(\sum_{i=1}^{n} \tan^{-1}\left(\frac{\omega}{s_{p_i}}\right) - \sum_{i=1}^{q} \tan^{-1}\left(\frac{\omega}{s_{z_i}}\right) + \pi(q^- - n^-)\right) \tag{II.6}$$

Keeping in mind that for every integer k it holds

$$\sin(x + \pi k) = (-1)^k \sin(x), \tag{II.7}$$

and taking the limit on Eq. (II.6), it results in

$$a = k(-1)^{q^- - n^-} \frac{\prod_{i=1}^{q} |s_{z_i}|}{\prod_{i=1}^{n} |s_{p_i}|} \left(\sum_{i=1}^{n} \frac{1}{s_{p_i}} - \sum_{i=1}^{q} \frac{1}{s_{z_i}} \right) \tag{II.8}$$

Finally, considering that $|x| = x$ for real positive values of x, $|x| = -x$ for real negative values of x, and $|x|^2 = xx^*$ for complex values of x, the asymptote a results in

$$a = k \frac{\prod_{i=1}^{q} -s_{z_i}}{\prod_{i=1}^{n} -s_{p_i}} \left(\sum_{i=1}^{n} \frac{1}{s_{p_i}} - \sum_{i=1}^{q} \frac{1}{s_{z_i}} \right) \tag{II.9}$$

Note that a lead controller, in which a pole-zero pair is present and the pole is faster than the zero, results in a shift of the asymptote to the right. The opposite is true for a lag controller, which shifts the asymptote to the left.

BIBLIOGRAPHY

[1] H. Schellnhuber, *Global Sustainability: A Nobel Cause*. Cambridge University Press, 2010. [Online]. Available: https://books.google.de/books?id=fLij0sWtZiQC

[2] "DOE global energy storage database," http://www.energystorageexchange.org/projects.

[3] H. Holttinen, *The Impact of Large Scale Wind Power Production on the Nordic Electricity System*. VTT Publications, 2005.

[4] P. Kundur, *Power System Stability And Control*, ser. EPRI power system engineering series. McGraw-Hill Education (India) Pvt Limited, 1994. [Online]. Available: http://books.google.de/books?id=v3RxH_GkwmsC

[5] R. H. Lasseter and P. Piagi, "Microgrid: A conceptual solution," in *in Proc. Power Electronics Specialists Conference*, 2004.

[6] H. Saboori, M. Mohammadi, and R. Taghe, "Virtual power plant (vpp), definition, concept, components and types," in *Power and Energy Engineering Conference (APPEEC), 2011 Asia-Pacific*, March 2011, pp. 1–4.

[7] F. Katiraei, M. Iravani, and P. Lehn, "Small-signal dynamic model of a micro-grid including conventional and electronically interfaced distributed resources," *Generation, Transmission Distribution, IET*, vol. 1, no. 3, pp. 369–378, May 2007.

[8] X. Yu, A. Khambadkone, H. Wang, and S. Terence, "Control of parallel-connected power converters for low-voltage microgrid;part i: A hybrid control architecture," *Power Electronics, IEEE Transactions on*, vol. 25, no. 12, pp. 2962–2970, Dec 2010.

[9] P. Hasanpor Divshali, S. Hosseinian, and M. Abedi, "A novel multi-stage fuel cost minimization in a vsc-based microgrid considering stability, frequency, and voltage constraints," *Power Systems, IEEE Transactions on*, vol. 28, no. 2, pp. 931–939, 2013.

[10] E. Barklund, N. Pogaku, M. Prodanovic, C. Hernandez-Aramburo, and T. Green, "Energy management in autonomous microgrid using stability-constrained droop control of inverters," *Power Electronics, IEEE Transactions on*, vol. 23, no. 5, pp. 2346–2352, 2008.

[11] G. Diaz, C. Gonzalez-Moran, J. Gomez-Aleixandre, and A. Diez, "Scheduling of droop coefficients for frequency and voltage regulation in isolated microgrids," *Power Systems, IEEE Transactions on*, vol. 25, no. 1, pp. 489–496, Feb 2010.

[12] M. Hassan and M. Abido, "Optimal design of microgrids in autonomous and grid-connected modes using particle swarm optimization," *Power Electronics, IEEE Transactions on*, vol. 26, no. 3, pp. 755–769, March 2011.

[13] I.-Y. Chung, W. Liu, D. Cartes, J. Collins, E.G., and S.-I. Moon, "Control methods of inverter-interfaced distributed generators in a microgrid system," *Industry Applications, IEEE Transactions on*, vol. 46, no. 3, pp. 1078–1088, May 2010.

[14] Nieße, A., Lehnhoff, S., Tröschel, M., Uslar, M., Wissing, C., Appelrath, H.-J. and Sonnenschein, M., "Market-based self-organized provision of active power and ancillary services: An agent-based approach for smart distribution grids," *2012 IEEE Workshop on Complexity in Engineering*, 2012.

[15] A. Nieße and M. Sonnenschein, "Using grid related cluster schedule resemblance for energy rescheduling - goals and concepts for rescheduling of clusters in decentralized energy systems." in *SMARTGREENS*, B. Donnellan, J. F. Martins, M. Helfert, and K.-H. Krempels, Eds. SciTePress, 2013, pp. 22–31. [Online]. Available: http://dblp.uni-trier.de/db/conf/smartgreens/smartgreens2013.html

[16] J. Guerrero, L. Garcia de Vicuna, J. Matas, M. Castilla, and J. Miret, "A wireless controller to enhance dynamic performance of parallel inverters in distributed generation systems," *Power Electronics, IEEE Transactions on*, vol. 19, no. 5, pp. 1205–1213, Sept 2004.

[17] G. Yajuan, W. Weiyang, G. Xiaoqiang, and H. Wu, "An improved droop controller for grid-connected voltage source inverter in microgrid," in *Power Electronics for Distributed Generation Systems (PEDG), 2010 2nd IEEE International Symposium on*, June 2010, pp. 823–828.

[18] R. Majumder, A. Ghosh, G. Ledwich, and F. Zare, "Angle droop versus frequency droop in a voltage source converter based autonomous microgrid,"

in *Power Energy Society General Meeting, 2009. PES '09. IEEE*, 2009, pp. 1–8.

[19] H. Avelar, W. Parreira, J. Vieira, L. de Freitas, and E. Alves Coelho, "A state equation model of a single-phase grid-connected inverter using a droop control scheme with extra phase shift control action," *Industrial Electronics, IEEE Transactions on*, vol. 59, no. 3, pp. 1527–1537, March 2012.

[20] Y.-R. Mohamed and E. El-Saadany, "Adaptive decentralized droop controller to preserve power sharing stability of paralleled inverters in distributed generation microgrids," *Power Electronics, IEEE Transactions on*, vol. 23, no. 6, pp. 2806–2816, Nov 2008.

[21] J. Vasquez, J. Guerrero, M. Savaghebi, J. Eloy-Garcia, and R. Teodorescu, "Modeling, analysis, and design of stationary-reference-frame droop-controlled parallel three-phase voltage source inverters," *Industrial Electronics, IEEE Transactions on*, vol. 60, no. 4, pp. 1271–1280, April 2013.

[22] H. Liang, B. J. Choi, W. Zhuang, and X. Shen, "Stability enhancement of decentralized inverter control through wireless communications in microgrids," *Smart Grid, IEEE Transactions on*, vol. 4, no. 1, pp. 321–331, March 2013.

[23] M. Shahidehpour, H. Yamin, and Z. Li, *Market Operations in Electric Power Systems: Forecasting, Scheduling, and Risk Management*. Wiley, 2003. [Online]. Available: http://books.google.de/books?id=RxXdmxLUJ_QC

[24] K. Suresh, *Electric Circuits And Networks (For Gtu)*. Pearson Education, 2010. [Online]. Available: http://books.google.de/books?id=-8xuxa1r1J4C

[25] G. Kron, *Tensor analysis of networks*. Macdonald, 1965. [Online]. Available: http://books.google.de/books?id=Xu0iAAAAMAAJ

[26] F. Dörfler and F. Bullo, "Kron reduction of graphs with applications to electrical networks," *Circuits and Systems I: Regular Papers, IEEE Transactions on*, vol. 60, no. 1, pp. 150–163, 2013.

[27] S. Bedrosian, "Converse of the star-mesh transformation," *Circuit Theory, IRE Transactions on*, vol. 8, no. 4, pp. 491–493, Dec 1961.

[28] D. Shen, "Generalized star and mesh transformations," *Phil. Mag.*, vol. 38, no. 7, pp. 267–275, April 1947.

[29] G. Calabrese, "Notes on the equivalence of electrical networks," *Gen. Elec. Rev.*, vol. 42, pp. 323–325, July 1939.

[30] "Smart nord – intelligente netze norddeutschland," http://http://www.smartnord.de/.

[31] M. Newman, *Networks: An Introduction*. OUP Oxford, 2010. [Online]. Available: http://books.google.de/books?id=LrFaU4XCsUoC

[32] P. Hines, S. Blumsack, E. Cotilla Sanchez, and C. Barrows, "The topological and electrical structure of power grids," in *System Sciences (HICSS), 2010 43rd Hawaii International Conference on*, Jan 2010, pp. 1–10.

[33] Z. Wang, A. Scaglione, and R. Thomas, "Generating statistically correct random topologies for testing smart grid communication and control networks," *Smart Grid, IEEE Transactions on*, vol. 1, no. 1, pp. 28–39, June 2010.

[34] H. Meier, C. Fünfgeld, and B. Schieferdecker, *Repräsentative VDEW-Lastprofile, VDEW-Materialien M-28/99*. Verband der Elektrizitätswirschaft, 1999.

[35] R. Majumder, *Microgrid : Stability Analysis and Control: Modeling, Stability Analysis and Control of Microgrid for Improved Power Sharing and Power Flow Management*. VDM Publishing, 2010. [Online]. Available: http://books.google.de/books?id=20zWRgAACAAJ

[36] J. Guerrero, L. Garcia de Vicuna, J. Matas, M. Castilla, and J. Miret, "Output impedance design of parallel-connected ups inverters with wireless load-sharing control," *Industrial Electronics, IEEE Transactions on*, vol. 52, no. 4, pp. 1126–1135, 2005.

[37] N. Pogaku, M. Prodanovic, and T. Green, "Modeling, analysis and testing of autonomous operation of an inverter-based microgrid," *Power Electronics, IEEE Transactions on*, vol. 22, no. 2, pp. 613–625, 2007.

[38] C. Zhang, T. Dragicevic, J. Vasquez, and J. Guerrero, "Resonance damping techniques for grid-connected voltage source converters with LCL filters: a review," in *Energy Conference (ENERGYCON), 2014 IEEE International*, May 2014, pp. 169–176.

[39] M. Savaghebi, J. Guerrero, A. Jalilian, and J. Vasquez, "Mitigation of voltage and current harmonics in grid-connected microgrids," in *Industrial Electronics (ISIE), 2012 IEEE International Symposium on*, May 2012, pp. 1610–1615.

[40] E. Coelho, P. Cortizo, and P. Garcia, "Small-signal stability for parallel-connected inverters in stand-alone AC supply systems," *Industry Applications, IEEE Transactions on*, vol. 38, no. 2, pp. 533–542, 2002.

[41] E. Alves Coelho, P. Cortizo, and P. Garcia, "Small signal stability for single phase inverter connected to stiff AC system," in *Industry Applications Conference, 1999. Thirty-Fourth IAS Annual Meeting. Conference Record of the 1999 IEEE*, vol. 4, 1999, pp. 2180–2187 vol.4.

[42] W. Yao, M. Gao, Z. Ren, M. Chen, and Z. Qian, "Study on the impact of the complex impedance on the droop control method for the parallel inverters," in *Applied Power Electronics Conference and Exposition (APEC), 2010 Twenty-Fifth Annual IEEE*, 2010, pp. 1204–1208.

[43] M. Reza, D. Sudarmadi, F. Viawan, W. Kling, and L. van der Sluis, "Dynamic Stability of Power Systems with Power Electronic Interfaced DG," in *Power Systems Conference and Exposition, 2006. PSCE '06. 2006 IEEE PES*, 2006, pp. 1423–1428.

[44] C. Sao and P. Lehn, "Control and power management of converter fed microgrids," in *Power and Energy Society General Meeting, 2010 IEEE*, 2010, pp. 1–1.

[45] V. Venkatasubramanian, H. Schattler, and J. Zaborszky, "Fast time-varying phasor analysis in the balanced three-phase large electric power system," *Automatic Control, IEEE Transactions on*, vol. 40, no. 11, pp. 1975–1982, Nov 1995.

[46] A. Stankovic and T. Aydin, "Analysis of asymmetrical faults in power systems using dynamic phasors," in *Power Engineering Society Summer Meeting, 2000. IEEE*, vol. 3, 2000, pp. 1957 vol. 3–.

[47] K. De Brabandere, B. Bolsens, J. Van den Keybus, J. Driesen, M. Prodanovic, and R. Belmans, "Small-signal stability of grids with distributed low-inertia generators taking into account line phasor dynamics," in *Electricity Distribution, 2005. CIRED 2005. 18th International Conference and Exhibition on*, June 2005, pp. 1–5.

[48] L. Wang, X. Q. Guo, H. R. Gu, W. Wu, and J. Guerrero, "Precise modeling based on dynamic phasors for droop-controlled parallel-connected inverters," in *Industrial Electronics (ISIE), 2012 IEEE International Symposium on*, May 2012, pp. 475–480.

[49] R. Bracewell, *The Fourier Transform and Its Applications*, ser. McGraw-Hill international editions. McGraw-Hill Education, 2000. [Online]. Available: http://books.google.de/books?id=ecH2KgAACAAJ

[50] Z. Miao, A. Domijan, and L. Fan, "Investigation of microgrids with both inverter interfaced and direct AC-connected distributed energy resources," *Power Delivery, IEEE Transactions on*, vol. 26, no. 3, pp. 1634–1642, July 2011.

[51] C. Karawita and U. Annakkage, "A hybrid network model for small signal stability analysis of power systems," *Power Systems, IEEE Transactions on*, vol. 25, no. 1, pp. 443–451, Feb 2010.

[52] H.-P. Beck and R. Hesse, "Virtual synchronous machine," in *Electrical Power Quality and Utilisation, 2007. EPQU 2007. 9th International Conference on*, Oct 2007, pp. 1–6.

[53] T. Van, K. Visscher, J. Diaz, V. Karapanos, A. Woyte, M. Albu, J. Bozelie, T. Loix, and D. Federenciuc, "Virtual synchronous generator: An element of future grids," in *Innovative Smart Grid Technologies Conference Europe (ISGT Europe), 2010 IEEE PES*, Oct 2010, pp. 1–7.

[54] Q.-C. Zhong and G. Weiss, "Synchronverters: Inverters that mimic synchronous generators," *Industrial Electronics, IEEE Transactions on*, vol. 58, no. 4, pp. 1259–1267, April 2011.

[55] T. Kawabata and S. Higashino, "Parallel operation of voltage source inverters," *Industry Applications, IEEE Transactions on*, vol. 24, no. 2, pp. 281–287, Mar 1988.

[56] M. Chandorkar, D. Divan, and R. Adapa, "Control of parallel connected inverters in standalone AC supply systems," *Industry Applications, IEEE Transactions on*, vol. 29, no. 1, pp. 136–143, Jan 1993.

[57] A. Tuladhar, K. Jin, T. Unger, and K. Mauch, "Parallel operation of single phase inverter modules with no control interconnections," in *Applied Power Electronics Conference and Exposition, 1997. APEC '97 Conference Proceedings 1997., Twelfth Annual*, vol. 1, Feb 1997, pp. 94–100 vol.1.

[58] A. Bergen, *Power systems analysis*, ser. Prentice-Hall series in electrical and computer engineering. Prentice-Hall, 1986. [Online]. Available: http://books.google.de/books?id=9uhSAAAAMAAJ

[59] A. Engler and N. Soultanis, "Droop control in LV-grids," in *Future Power Systems, 2005 International Conference on*, Nov 2005, pp. 6 pp.–6.

[60] N. Benesch, "Netzregelung von wechselrichtersystemen für die energieerzeugung in microgrids," in *SPS/IPC/Drives Kongress 2013, Nürnberg, Deutschland*, 2013, pp. 449–458.

[61] A. Pikovsky, M. Rosenblum, and J. Kurths, *Synchronization: A Universal Concept in Nonlinear Sciences*, ser. Cambridge Nonlinear Science Series. Cambridge University Press, 2003. [Online]. Available: http://books.google.de/books?id=FuIv845q3QUC

[62] Y. Kuramoto, "Self-entrainment of a population of coupled nonlinear oscillators," in *International Symposium on Mathematical Problems in Theoretical Physics, Lecture Notes in Physics, Vol. 39,*, H. Araki, Ed. New York, NY, USA: Springer, 1975, pp. 420–422.

[63] J. A. Acebrón, L. L. Bonilla, C. J. Pérez Vicente, F. Ritort, and R. Spigler, "The kuramoto model: A simple paradigm for synchronization phenomena," *Rev. Mod. Phys.*, vol. 77, pp. 137–185, Apr 2005. [Online]. Available: http://link.aps.org/doi/10.1103/RevModPhys.77.137

[64] J. W. Simpson-porco, F. Dörfler, and F. Bullo, "Droop-controlled inverters in microgrids are kuramoto oscillators," in *3rd IFAC Workshop on Distributed Estimation and Control in Networked Systems*, 2012.

[65] F. Dörfler and F. Bullo, "Synchronization and transient stability in power networks and non-uniform kuramoto oscillators," in *American Control Conference (ACC), 2010*, June 2010, pp. 930–937.

[66] Y. Wang, Z. Lu, Y. Min, and Z. Wang, "Small signal analysis of microgrid with multiple micro sources based on reduced order model in islanding operation," in *Power and Energy Society General Meeting, 2011 IEEE*, July 2011, pp. 1–9.

[67] I. Balaguer, Q. Lei, S. Yang, U. Supatti, and F. Z. Peng, "Control for grid-connected and intentional islanding operations of distributed power generation," *Industrial Electronics, IEEE Transactions on*, vol. 58, no. 1, pp. 147–157, Jan 2011.

[68] J. Liceaga-Castro, E. Liceaga-Castro, and I. Alcala, "Phase and gain margins for MIMO linear control systems," in *System Theory, Control and Computing (ICSTCC), 2012 16th International Conference on*, Oct 2012, pp. 1–6.

[69] E. Bristol, "On a new measure of interaction for multivariable process control," *Automatic Control, IEEE Transactions on*, vol. 11, no. 1, pp. 133–134, Jan 1966.

[70] F. Shinskey, *Process-control systems: application, design, adjustment*. McGraw-Hill, 1979. [Online]. Available: http://books.google.de/books?id=w6ZTAAAAMAAJ

[71] W. Hu, W.-J. Cai, and G. Xiao, "Relative gain array for MIMO processes containing integrators and/or differentiators," in *Control Automation Robotics Vision (ICARCV), 2010 11th International Conference on*, Dec 2010, pp. 231–235.

[72] T. McAvoy, *Interaction analysis: principles and applications*, ser. Monograph series. Instrument Society of América, 1983. [Online]. Available: http://books.google.de/books?id=xtdTAAAAMAAJ

[73] S. Skogestad and I. Postlethwaite, *Multivariable Feedback Control: Analysis and Design*, ser. Multivariable Feedback Control: Analysis and Design. Wiley, 2005. [Online]. Available: http://books.google.de/books?id=3dxSAAAAMAAJ

[74] J. Milanović and A. Duque, "Identification of electromechanical modes and placement of psss using relative gain array," *Power Systems, IEEE Transactions on*, vol. 19, no. 1, pp. 410–417, Feb 2004.

[75] Y. Li, C. Rehtanz, S. Ruberg, L. Luo, and Y. Cao, "Assessment and choice of input signals for multiple HVDC and FACTS wide-area damping controllers," *Power Systems, IEEE Transactions on*, vol. 27, no. 4, pp. 1969–1977, Nov 2012.

[76] F. Bertling and S. Soter, "A novel converter integrable impedance measuring method for islanding detection in grids with widespread use of decentral generation," in *Power Electronics, Electrical Drives, Automation and Motion, 2006. SPEEDAM 2006. International Symposium on*, May 2006, pp. 503–507.

[77] X. Sun, J. Chen, J. Guerrero, X. Li, and L. Wang, "Fundamental impedance identification method for grid-connected voltage source inverters," *Power Electronics, IET*, vol. 7, no. 5, pp. 1099–1105, May 2014.

[78] R. Kamphuis, K. Kok, C. Warmer, and M. Hommelberg, "Architectures for novel energy infrastructures: Multi-agent based coordination patterns," in *Infrastructure Systems and Services: Building Networks for a Brighter Future (INFRA), 2008 First International Conference on*, 2008, pp. 1–6.

[79] T. Nagata, R. Hatano, and H. Saiki, "A multi-agent based distributed reactive power control method," in *Power Energy Society General Meeting, 2009. PES '09. IEEE*, 2009, pp. 1–7.

[80] S. Lehnhoff, T. Klingenberg, M. Blank, M. Calabria, and W. Schumacher, "Distributed coalitions for reliable and stable provision of frequency response reserve – an agent-based approach for smart distribution grids," in *Intelligent Energy Systems (IWIES), 2013 IEEE International Workshop on*, Nov 2013, pp. 11–18.

[81] V. Mariani, F. Vasca, J. Vasquez, and J. Guerrero, "Model order reductions for stability analysis of islanded microgrids with droop control," *Industrial Electronics, IEEE Transactions on*, vol. PP, no. 99, pp. 1–1, 2014.

[82] L. Luo and S. Dhople, "Spatiotemporal model reduction of inverter-based islanded microgrids," *Energy Conversion, IEEE Transactions on*, vol. 29, no. 4, pp. 823–832, Dec 2014.

[83] S. Anand and B. Fernandes, "Reduced-order model and stability analysis of low-voltage DC microgrid," *Industrial Electronics, IEEE Transactions on*, vol. 60, no. 11, pp. 5040–5049, Nov 2013.

[84] C. Kelley, *Iterative Methods for Optimization*, ser. Frontiers in Applied Mathematics. Society for Industrial and Applied Mathematics, 1999. [Online]. Available: https://books.google.de/books?id=Bq6VcmzOe1IC

[85] R. Teodorescu, F. Blaabjerg, M. Liserre, and P. Loh, "Proportional-resonant controllers and filters for grid-connected voltage-source converters," *Electric Power Applications, IEE Proceedings*, vol. 153, no. 5, pp. 750–762, September 2006.

[86] R. Teodorescu, F. Blaabjerg, U. Borup, and M. Liserre, "A new control structure for grid-connected LCL PV inverters with zero steady-state error and selective harmonic compensation," in *Applied Power Electronics Conference and Exposition, 2004. APEC '04. Nineteenth Annual IEEE*, vol. 1, 2004, pp. 580–586 Vol.1.

[87] Y. W. Li, "Control and resonance damping of voltage-source and current-source converters with lc filters," *Industrial Electronics, IEEE Transactions on*, vol. 56, no. 5, pp. 1511–1521, May 2009.

[88] R. Carnieletto, D. Ramos, M. Simoes, and F. Farret, "Simulation and analysis of dq frame and proportional-resonant controls for voltage source inverter to distributed generation," in *Power Electronics Conference, 2009. COBEP09 Brazil*, Sept 2009, pp. 104–109.

[89] S. Eren, M. Pahlevaninezhad, A. Bakhshai, and P. Jain, "Composite nonlinear feedback control and stability analysis of a grid-connected voltage

source inverter with LCL filter," *Industrial Electronics, IEEE Transactions on*, vol. 60, no. 11, pp. 5059–5074, Nov 2013.

[90] J. Eloy-Garcia, J. Vasquez, and J. Guerrero, "Grid simulator for power quality assessment of micro-grids," *Power Electronics, IET*, vol. 6, no. 4, pp. 700–709, April 2013.

[91] J. He and Y. W. Li, "Generalized closed-loop control schemes with embedded virtual impedances for voltage source converters with LC or LCL filters," *Power Electronics, IEEE Transactions on*, vol. 27, no. 4, pp. 1850–1861, April 2012.

[92] M. Marwali, J.-W. Jung, and A. Keyhani, "Control of distributed generation systems - part ii: Load sharing control," *Power Electronics, IEEE Transactions on*, vol. 19, no. 6, pp. 1551–1561, Nov 2004.

[93] D. De and V. Ramanarayanan, "Decentralized parallel operation of inverters sharing unbalanced and nonlinear loads," *Power Electronics, IEEE Transactions on*, vol. 25, no. 12, pp. 3015–3025, Dec 2010.

[94] A. Polyanin and A. Manzhirov, *Handbook of Mathematics for Engineers and Scientists*. Taylor & Francis, 2006. [Online]. Available: http://books.google.de/books?id=knnDOwlNE4AC